WW dibosons at the LHCb experiment

Ben William McSkelly
The University of Liverpool

Thesis submitted in accordance with the requirements of The University of Liverpool
for the degree of Doctor of Philosophy
January 2015

Abstract

The Large Hadron Collider (LHC) is a proton–proton collider that has achieved a world high centre of mass energy. The protons are collided at four distinct detectors. One such is the ATLAS, a large general purpose detector aimed at a multitude of physics analyses. At the start of this PhD, work was undertaken searching for supersymmetry at the ATLAS experiment. After calculating the rates of various processes for wider use, work was undertaken searching for pair production of stops, the supersymmetric partners of top particles. A two lepton stop particle analysis is presented with focus on data driven estimates of electroweak backgrounds.

The main analysis in this thesis was conducted using the LHCb experiment. LHCb is a precision detector focusing on events in the forward region. Although primarily designed for B physics, high precision LHCb tracking and vertex resolution allows for electroweak measurements probing proton parton distribution functions at low values of Björken–x. A method for measurement of the fiducial cross section of WW events with $|\eta| > 2$ is presented. The electron–muon channel is chosen due to lower background rates. Events with no jet content and a pair of high momentum leptons originating from the same vertex are selected. The measurement suffers from a small statisitical sample, but nevertheless measures a cross section,

$\sigma_{fid}(\sqrt{s} = 8\,\text{TeV}) = 4.7 \pm 1.5(\text{stat.}) \pm 0.5(\text{syst.}) \pm 0.1(\text{lumi.})\,\text{fb}$

consistent with the standard model prediction. Finally, the future of diboson measurements at LHCb is assessed. Further LHCb runs due to begin imminently, will provide sufficient data to alleviate statistical limits and produce competitive measurements.

Declaration

This dissertation is the result of my own work, except where explicit reference is made to the work of others, and has not been submitted for another qualification to this, or any, other university. This dissertation does not exceed the word limit for the respective Degree Committee.

Ben William McSkelly

Acknowledgements

Having changed experiment after two years of my PhD, I have many people to thank for making it to the end without losing my hair. Themis Bowcock was instrumental in this and I am greatly indebted to him. Too often in particle physics the focus on publishing papers comes before everything, including the best interests of students. Themis told me to focus on my thesis above all else and went out of his way to help. I'd also like to thank David Joss, he listens to PhD students and has genuine drive to sort out their problems with the system.

I'd like to thank David Hutchcroft and Steven Farry for volunteering to be supervisors in all but name and for their patience with my slow debugging skills. I'd like to thank my initial supervisors Barry and Monica. In particular, I worked extensively with Monica and her dedication to her students is really unrivaled, her passion for her job is inspiring and intimidating.

There are too many people at CERN to thank, but I must mention Kurt and Karol of the Liverpool group. There were many fellow PhD students whose advice, fresh eyes and code swaps were very helpful; Danny, Henry, Miffy, Sara, Terry[1] and Will to name a few. Oh and thanks to Harvey and McKenna for proving if CERN is going to send you slightly potty, its nice to have company.

I also thank Sazzi for her patience with a poor, stressed and busy PhD student.

Oh and immeasurable thanks to my parents.

[1] also known as Yan-Jie and numerous nicknames

Contents

Chapter 1

Introduction

Particle physics is the study of the most fundamental constituents of matter and their interactions. Underpinning particle physics since the 1970s is the Standard Model (SM). This theoretical framework is a collection of quantum field theories; quantum descriptions of particles with special relativity applied. The motivation and properties of each force is built from a gauge symmetry group with Lorentz invariance applied. This does not, however, include the gravitational force, which is best described by general relativity. Chapter 2 of this thesis explains the SM in detail, noting it's successes and deficiencies. Notably the SM offers no candidate phenomena for the observations of dark matter, non–zero neutrino masses or matter–antimatter asymmetry in the universe.

The Large Hadron Collider (LHC) finished the first long scale data taking period in early 2013. Accelerating protons at hitherto unachievable energies enables the production of high mass particles via the famous energy mass relation $E = mc^2$[1]. With such a machine it is possible to test and measure the parameters of the SM in order to tune and tweak the modelling. These tests have produced a number of successes during LHC running, most notably measurements of a particle consistent with a Higgs Boson, the particle theorised in order to provide a mass mechanism for SM particles. Secondly, one may wish to look for physics Beyond the Standard Model (BSM), either by direct detection or by indirect measurements not consistent with the SM.

This thesis uses two of the detectors on the LHC machine, the ATLAS and LHCb detectors. At each of these detectors, the clockwise and anti–clockwise proton beams are collided. In the ATLAS detector, this collision occurs in the centre of a barrel shaped detector, aiming to detect all the particles subsequently created regardless of direction of flight. Alternatively, the LHCb detector aims to detect particles only in a small angular acceptance in the forward direction. The smaller acceptance allows for alternative detector design and greater precision in the tracking of charged particles.

Chapter 3 first details the LHC machinery and performance. Secondly, the LHCb detector components and performance are discussed in more detail.
Chapter 4 begins with a description of the ATLAS detector. The rest of the chapter details a supersymmetry search on the ATLAS detector performed in the first half of the PhD timeframe. This was a direct search for BSM phenomena and particles, namely for pair production of the light supersymmetric partner of the top quark. This analysis searches for a very low statistic signal that is very kinematically similar to SM production of top quarks. This requires exacting measurements of backgrounds, specifically in this document fake leptons arising from jets estimated using the data driven matrix method. The final results enabled increased exclusion of phenomenological supersymmetry models with low mass.
The main analysis presented in this thesis is a search for pairs of W bosons in the LHCb detector. The weak nuclear force is mediated by the W and Z bosons. These heavy bosons can be produced in pairs in proton–proton collisions, mainly in the transverse direction. Diboson events that are produced in the LHCb acceptance can be used to probe the SM, such as the internal parton layout of the proton. Chapter 5 details the motivation for a WW search. The signal characteristics are compared with the main backgrounds, as are the simulations used to describe them. The event selections used to discriminate signal from backgrounds are motivated, with the efficiency for each calculated. Finally the resulting cross section for the WW process is presented.
Chapter 6 estimates the possibilities of more diboson measurements at LHCb in the future LHC runs. It is shown that with increased data luminosity and increased production rates at higher collision energy, diboson searches increase greatly in potential. The WW channel improves in this scenario, with the increased event numbers providing scope for more precise backgrounds estimates. Furthermore the ZZ channel becomes attractive, due to it's unique signal with very small rates of background processes.

Chapter 2

Theoretical Overview

Particle physics is the study of fundamental particles of matter and their interactions. The states of these fundamental particles are best described by quantum mechanics, while their space-time development are described by special relativity. To describe the confluence of these two theories one must use a relativistic quantum field theory. The Standard Model (SM) is a collection of such theories that provides self-consistent, tested predictions for interactions of the strong, weak and electromagnetic force[1]. The following chapter will discuss the implications, successes and limits of the Standard Model (SM).

2.1 Fundamental Particles

The fundamental particles detected by experimental methods and predicted by the SM consist of half–integer spin fermions, with integer spin bosons responsible for mediating interactions.

2.1.1 Fermions

Fundamental fermions can be separated into two branches, six quarks which interact via the strong force and six leptons that do not. Additionally, every fermion has an antiparticle, a negative energy solution of the relativistic energy-momentum relation. These antiparticles carry the opposite electric charge but otherwise the same quantum

[1]The Standard Model does not provide predictive method for the inclusion of gravity. Higher level models such as String Theory aim to reconcile gravity as described by general relativity with the basis of particle physics. From a collider experiment point of view, gravity is negligibly weak.

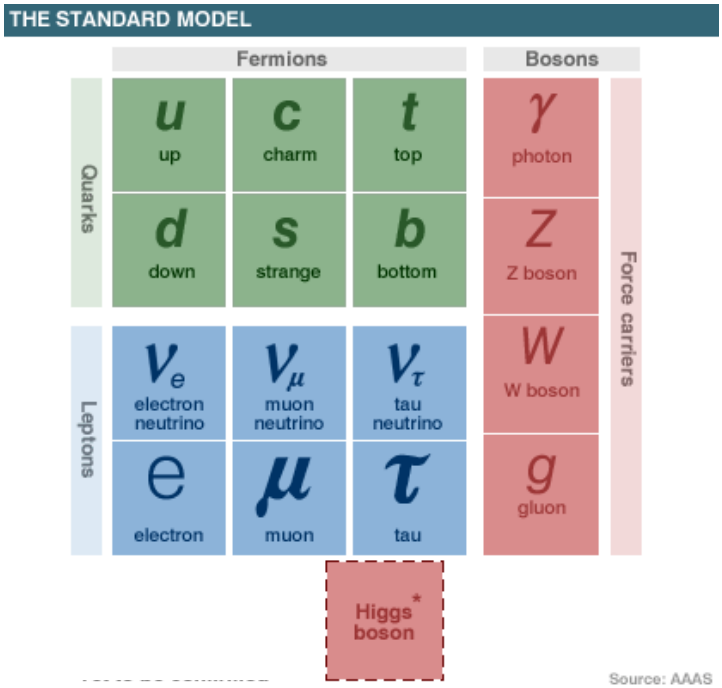

Figure 2.1: The particles contained within the Standard Model, as portrayed by the AAAS.

numbers (hence the same interaction properties) and are denoted by a bar, ie antidown quark $\bar{d}$.

Quarks do not naturally occur in isolation but are bound by the strong force into hadrons. The proton uud and neutron udd are examples of baryons, collections of three bound quarks. Mesons are composite particles of two bound quarks. For example, pions are mesons consisting of a up or down quark bound with an antiup or antidown. Three pairs of quarks exist with charges of $\frac{2}{3}$ or $-\frac{1}{3}$; namely the up and down, charm and strange and top and bottom. Three negatively charged leptons are paired with their corresponding neutrino; electron–electron neutrino, muon–muon neutrino and tau–tau neutrino pairs. Neutrino flavour mixing as discussed in Section 2.3.2 suggests mass, however this mass is so small only upper limits on neutrino mass exist. These neutral fermions interact via the weak or gravitational interactions, but effects are limited by their small weak coupling and mass respectively.

These twelve particles can be categorised into three generations. The first generation consists of the electron, electron neutrino, up and down quarks. The further two generations consist of particles with the same quantum numbers, but with increased mass. These properties can be shown in Figure 2.1, where the first three columns are populated by these three generations. No experimental evidence for fourth generation

particles has been found. Furthermore strict indirect limits have been placed on a fourth generation. These limits are discussed in more details in sections 2.2.3 and 2.3.2.

2.1.2 Gauge Bosons and Interactions

In the SM forces act by the exchange of mediating spin–1 particles known as gauge bosons. The couplings of the bosons, as described in Table 2.1, define the action of the interactions with fermions. The electromagnetic interaction between any electrically charged particle is mediated by the massless photon, leading to no restrictions on the range of the force. The weak interaction is mediated by W and Z bosons, acting upon particles with weak isospin. Weak interactions are unique in changing the flavour of quarks and drive nuclear decay processes such as those in stars. As mediating bosons are virtual[2], the mass of the W and Z bosons restrict the range of the interaction to roughly 10^{-2} fm. The strong force is mediated by gluons, as is named after the large coupling constant is carries. It acts upon colour charges, which only quarks and gluons exhibit. For two partons[3] bound at close range, the energy taken to separate them exceeds that to create an additional pair of quarks. Hence, isolated quarks do not occur, as the newly created quarks bind with the original quarks as they separate. This phenomenon is called colour confinement, because single colour charges are not visible. Conversely as quarks are brought together, the interaction strength decreases, such that within a bound state the partons effectively have asymptotic freedom.

Boson	Mass (GeV)	Q/e	Associated Charge
Gluon	0	0	Colour Charge
Photon	0	0	Electric Charge
W	80.385	± 1	Weak Isospin
Z	91.1876	0	Weak Isospin

Table 2.1: Selected properties of the gauge bosons in the Standard Model, where Q/e is the electric charge of a particle normalised to that of an electron. Data taken from the Particle Data Group [2].

[2]A virtual particle in a physics process cannot be directly observed. The uncertainty principle states that such particles can borrow energy from the vacuum with a limited lifetime. Hence these particles can be off–shell, particles that do not follow the Einstein energy–momentum relation.

[3]Partons are gluons/quarks modelled as point particle in the high energy approximation such that the frame of reference effectively has infinite momentum.

2.2 The Standard Model

This section will describe the key characteristics of the standard model, namely the gauge formalisation of three interactions. Each interaction and the associated gauge boson(s) can be directly motivated from a single gauge symmetry principle. The first step is to identify a global gauge symmetry under which the Lagrangian is invariant. Noether's theorem[3] infers a conserved quantity for each symmetry and the localised symmetry infers an interacting theory. The following section uses symmetry under the $U(1)$ transformation to produce the characteristics and mechanics of quantum electro dynamics. For the SM formalism, only variations on the unitary groups $U(n)$ are needed. $U(n)$ are the n dimensional unitary matrix groups. The matrices that define these groups have the property $U^{-1} = U^{\dagger}$. In the case where the unitary matrices have unit determinant values, the groups are labelled special unitary $SU(n)$.

2.2.1 Quantum Electro Dynamics

Quantum Electro Dynamics (QED) is an interacting theory built upon symmetry of the $U(1)$ gauge group. A brief outline of how this symmetry can be shown to reproduce the laws of electromagnetism now follows. The global $U(1)$ symmetry is such that the Lagrangian is invariant under rotation through an angle α on the particle field, where the angle α has no dependence on spatial co–ordinates. Transformed fields F are denoted F', in this case $\psi' = e^{i\alpha}\psi$. The Lagrangian for a free particle is

$$\mathcal{L}_{free} = \bar{\psi} i \partial\!\!\!/ \psi - m\bar{\psi}\psi \tag{2.1}$$

using covariant notation. A global symmetry is not entirely physical. Instead, it is more reasonable to have a localised symmetry $\psi' = e^{i\Lambda(x)}\psi$, where the rotation angle $\Lambda(x)$ itself has a space-time dependence. To satisfy relativistic principles, a Lorentz Gauge Invariant (LGI) Lagrangian is required, but this local phase invariance presents issues with derivatives. Specifically terms with $\partial_\mu \Lambda(x)$ have transformations under the symmetry that do not maintain LGI. The solution is to introduce a new vector field A_μ, to cancel $\partial_\mu \Lambda(x)$ terms and consequently define a new gauge covariant derivative D_μ

such that

$$A'_\mu = A_\mu - \frac{i}{g}\partial_\mu \Lambda \tag{2.2}$$

and

$$D_\mu = \partial_\mu - igA_\mu \tag{2.3}$$

with an associated constant g. Additionally, a kinetic energy term is required without reliance on the field ψ. Noting the formulation of the commutator $[D_\mu, D_\nu] = igF_{\mu\nu}$ which is itself LGI, the Lagrangian for this local rotation symmetry is

$$\mathcal{L} = \bar{\psi} i \not{D}_\mu \psi - m\bar{\psi}\psi - \frac{1}{4} F_{\mu\nu} F^{\mu\nu} \tag{2.4}$$

with slash notation $\not{D}_\mu = j^\mu D_\mu$ implemented. An interaction term $g\bar{\psi}\gamma_\mu A^\mu \psi$, between the particle and a gauge boson has been introduced. The structures of electromagnetism can hence be identified; namely the constant g as the electron charge e, the electromagnetic field tensor $F^{\mu\nu}$ and interacting field of the photon A_μ. These structures are consistent with the classical Maxwell formulation but have been entirely motivated from the gauge symmetry. No mass term for the boson itself is present as $\frac{1}{2} m_A A_\mu A^\mu$ is not LGI, hence the boson of QED in this theory is massless. More generally any Lagrangian invariant under a continuous local transformation infers an interacting theory with mediating spin 1 gauge boson(s). However, this formalism infers massless bosons which does not agree with experimental observation for the W and Z.

2.2.2 The Weak Force

The weak force is based on $SU(2)$ gauge symmetry group. In general for a SU(n) theory, the field transforms under the symmetry via a unitary matrix $\psi' = U\psi$ such that $\bar{\psi}\psi' = \bar{\psi} U U^\dagger \psi = \bar{\psi}\psi$. This unitary matrix for any $SU(n)$ group can be expanded

$$U(x) = \exp\left(-ig \sum_{k=1}^{n^2-1} \theta^k(x) t^k \right) \tag{2.5}$$

in terms of coupling constants g, real rotation angles θ^k and generator matrices t^k obeying the commutator relation $[t_a, t_b] = i f_{abc} t_c$. For $SU(2)$ these generators are the

Pauli matrices

$$\sigma_1 = \sigma_x = \begin{pmatrix} 0 & 1 \\ 1 & 0 \end{pmatrix}$$
$$\sigma_2 = \sigma_y = \begin{pmatrix} 0 & -i \\ i & 0 \end{pmatrix}$$
$$\sigma_3 = \sigma_z = \begin{pmatrix} 1 & 0 \\ 0 & -1 \end{pmatrix}$$

and for $SU(3)$ the Gell-Mann matrices

$$\lambda_1 = \begin{pmatrix} 0 & 1 & 0 \\ 1 & 0 & 0 \\ 0 & 0 & 0 \end{pmatrix}, \ \lambda_2 = \begin{pmatrix} 0 & -i & 0 \\ i & 0 & 0 \\ 0 & 0 & 0 \end{pmatrix}, \ \lambda_3 = \begin{pmatrix} 1 & 0 & 0 \\ 0 & -1 & 0 \\ 0 & 0 & 0 \end{pmatrix}, \ \lambda_4 = \begin{pmatrix} 0 & 0 & 1 \\ 0 & 0 & 0 \\ 1 & 0 & 0 \end{pmatrix}$$
$$\lambda_5 = \begin{pmatrix} 0 & 0 & -i \\ 0 & 0 & 0 \\ i & 0 & 0 \end{pmatrix}, \ \lambda_6 = \begin{pmatrix} 0 & 0 & 0 \\ 0 & 0 & 1 \\ 0 & 1 & 0 \end{pmatrix}, \ \lambda_7 = \begin{pmatrix} 0 & 0 & 0 \\ 0 & 0 & -i \\ 0 & i & 0 \end{pmatrix}, \ \lambda_8 = \frac{1}{\sqrt{3}} \begin{pmatrix} 1 & 0 & 0 \\ 0 & 1 & 0 \\ 0 & 0 & -2 \end{pmatrix}.$$

Similar to the process above for QED, a Lagrangian[4] for the localised symmetry can be written with interaction terms

$$\mathcal{L} = \bar{\psi} i \not{D}_\mu \psi - m\bar{\psi}\psi - \frac{1}{2}\mathrm{Tr}\left(\mathrm{F}^{\mu\nu}\mathrm{F}_{\mu\nu}\right) \tag{2.6}$$

where the kinetic energy term has become a trace of field tensors for each generator. This introduces two terms with self interactions of the vector field, cubic $g(\partial A)A^2$ and quartic g^2A^4 as shown in Figure 2.2. The charge of the weak interaction is the weak isospin I_3, otherwise known as the third component of isospin. This can be related the to weak hypercharge Y via the relation

$$Q = T_3 + Y/2 \tag{2.7}$$

with Q being the standard electric charge. Positively charged up–like quarks have $I_3 = +1/2$ and negatively charged down–like quarks have $I_3 = -1/2$. The weak interaction

[4]also symmetric under the CPT transformations

only allows decays of quarks to opposite isospin values, i.e from up to down–like quarks or the opposite.

Figure 2.2: Feynman diagrams illustrating the possible single vertex interactions with photon/W/Z bosons (left) and gluons (right).

(a) Particle field–boson interaction possible in both $U(1)$ and $SU(n)$.

(b) Cubic self interaction possible in $SU(n)$ theories only.

(c) Quartic self interaction possible in $SU(n)$ theories only.

2.2.3 Electroweak Unification and the Higgs Boson

To address the existence of massless bosons, the process of spontaneous symmetry breaking is used to produce a new field and boson. Weak interactions violate parity, acting differently on left handed and right handed fermions. Hence one can split the fermion fields into left handed and right handed components. With the zero mass approximation for neutrinos, only left handed neutrino terms are present. Similarly only left handed fermion fields interact via the weak force. Projecting out the right handed components[5] of SU(2) gives a left handed interaction term $\frac{1}{2}\bar{\psi}_L\gamma_\mu W^{a\mu}\sigma^2\psi_L$, with

[5]Projection of fields can be obtained by $P_{R/L} = \frac{1}{2}(1 \pm \gamma_5)$, where γ_5 is defined as the product of Dirac matrices $\gamma_5 = i\gamma_0\gamma_1\gamma_2\gamma_3$

$W^{a\mu}$ as the weak bosons and σ as the Pauli matrices. This can be combined with the electromagnetic gauge group as $SU(2)_L \otimes U(1)_Y$.
A generic theory must specify both the Lagrangian and the ground state to be fully

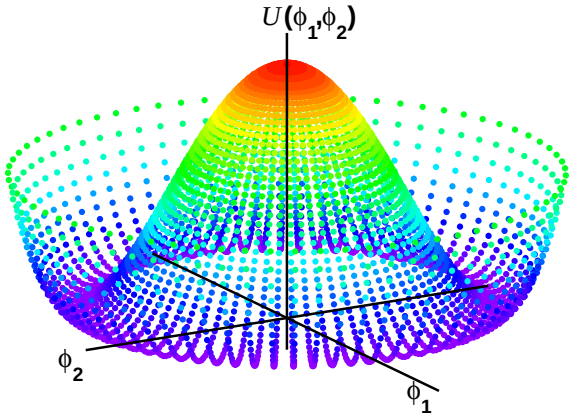

Figure 2.4: Illustration of a Higgs like potential, which maintains a symmetry until the ground state is chosen. Reproduced from [4].

complete. A potential of the form

$$V(\Phi) = -\frac{1}{2}\mu^2\left(\phi_1^2+\phi_2^2\right)+\frac{1}{4}\lambda^2\left(\phi_1^2+\phi_2^2\right)^2 \tag{2.8}$$

as shown in Figure 2.4 is chosen. The potential is symmetric, with a maximum at (0,0). Minima of the potential occur at $\phi_{min}^2 = v^2 = {}^{\mu}/_{\lambda}$ and are not symmetric. Rewriting the Lagrangian in terms of these minima $\tilde{\phi} = \phi - v$, breaks the previous symmetry $\Phi' = -\Phi$ giving a Lagrangian

$$\mathcal{L} = \frac{1}{2}\left(\partial_\mu\tilde{\phi}\right)^2+\frac{1}{2}\mu^2\left(\tilde{\phi}+v\right)^2-\frac{\lambda}{4!}\left(\tilde{\phi}+v\right)^4 = \frac{1}{2}\left(\partial_\mu\tilde{\phi}\right)^2-\mu^2\tilde{\phi}^2-\lambda v\tilde{\phi}^3-\frac{\lambda}{4!}\tilde{\phi}^4 \tag{2.9}$$

with the second term identifiable as mass–like. This is a basic example of spontaneous symmetry breaking, turning n massless fields into n-1 massless and one massive field, with a consequential boson. Applying this to a simple $U(1)$ theory, with a shifted field $\tilde{\phi} = {}^1/\sqrt{2}\,(v+\sigma-i\xi)$ prompts an interaction term between the fields A_μ and ξ. However after gauge transformation of the Lagrangian, all ξ' terms are cancelled by terms in A'_μ. The second field is said to have been 'eaten' by A_μ. Photons have no longitudinal degree of freedom, this eaten field provides the required third degree of freedom to the boson.

In addition a spin zero field σ with mass $\sqrt{2}\mu$ is again present, the Higgs boson. This spin–0 boson with mass 125 GeV is neutral in colour and electrostatic charge. It is a very unstable particle and is rarely produced due to its high mass. Observation was prevented until 2012 by these factors. The interaction between the gauge theory and the Higgs field generates mass.

For electroweak $SU(2)_L \otimes U(1)_Y$ theory, the scalar field is now a $SU(2)$ doublet field but proceeds in a similar way. The covariant derivative becomes $D_\mu = \partial_\mu + \frac{i}{2} g_L \sigma^a W_\mu^a + i g_Y B_\mu$, with the gauge bosons and coupling for $\mathrm{SU}(2)_L$ W_μ^a, g_L and $U(1)_Y$ B_μ, g_y. In this formulation, the quadratic terms of the bosons coming from $(D_\mu \phi_0^\dagger)(D^\mu \phi_0)$ gives three important terms

$$\mathcal{L} = ... + \frac{v^2}{2}\left(\frac{g_Y^2}{4}[(W_\mu^1)^2 + (W_\mu^2)^2] + \frac{1}{2}[g_L W_\mu^3 - g_Y B_\mu]^2 + 0[g_l W_\mu^3 + g_Y B_\mu]^2\right) + \ ...$$

relating to gauge boson masses. The first term gives mass to the $W^\pm$ bosons, the second to the Z boson and the final term is a photon mass term carrying a zero value. Normalising these fields gives values of boson masses

$$m_W = \frac{1}{2} g_L v, \quad m_Z = \frac{1}{2}\sqrt{g_L^2 + g_Y^2}\, v, \quad \frac{m_W}{m_Z} = \frac{g_L}{\sqrt{g_L^2 + g_Y^2}} = \cos\theta_\mathrm{W} \tag{2.10}$$

with θ_W known as the weak mixing angle. With the $SU(2)_L$ interaction acting differently on left and right handed fields of particles, simple mass terms for fermions, in the form $m\bar{f}f$, are not gauge invariant before spontaneous symmetry breaking. The solution is to couple CP opposite fields (see Section 2.3.1) in Lagrangian terms

$$... + -\bar{L}\lambda\phi R - \bar{R}\lambda\phi^\dagger L + \ ...$$

where L & R are the left and right handed fields and λ is the Yukawa coupling. After spontaneous symmetry breaking a fermion mass term appears as well as a coupling between Higgs field and the fermion, proportional to the fermion mass. Hence, this mechanism that provides mass to all fermions and well as gauge bosons. Relations such as Equation 2.10 can be used to present variables such as gauge couplings in terms of more readily measurable variables such as the weak mixing angle. Collectively these are known as the electroweak precision observables. Precise measurement of these variables has been possible, enabling stringent tests of the SM, search areas for new physics and predictions for the Higgs mass. Figure 2.5 shows an example electroweak precision observable fit.

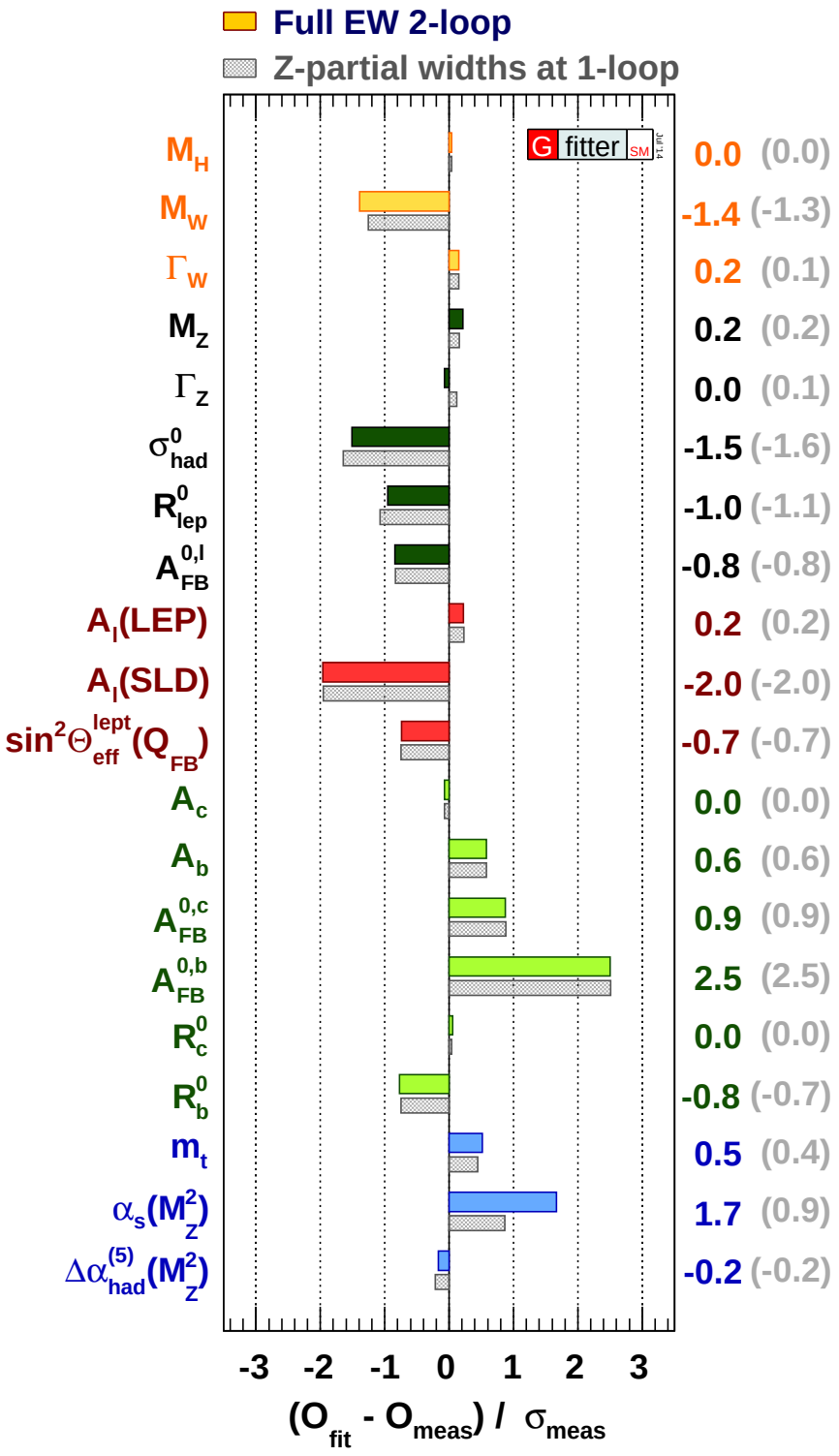

Figure 2.5: Pull of electroweak precision observables to the SM fit performed by the gFitter[5] group using LEP, TeVatron and LHC data.

2.2.4 Quantum Chromo Dynamics

QCD is a non-abelian SU(3) gauge interaction containing a triplet of Dirac fields. Following the form for unitary matrices as shown in Equation 2.5, there are eight generators of the theory. Each generator refers to a gluon field carrying a colour charge which controls strong interactions. Similar to the weak force shown in Section 2.2.2, triplet and quartic self interactions are possible. This leads to the coupling constant of QCD α_s, decreasing as the energy scale Q^2 increases. This leads to two unique phenomenon that define QCD. As quarks are separated, the attractive force between them rises until the energy available is enough to produce a quark-antiquark pair. This is known as quark confinement, such that an individual quark cannot be isolated. Secondly, at high energies α_s has a low value such that the strong force has little to no effect, known as asymptotic freedom.

2.2.5 Limits of the Standard Model

The experimental observation of candidate Higgs bosons in 2012 finally answered one of the outstanding issues within the SM, the non–zero masses of gauge bosons. Whether this particle is a purely SM Higgs boson or part of a more complicated multiple Higgs sector is an important question for the LHC going forward. However, there are still many problems to be solved within and outside of the SM, a few of which will be outlined here. The success of electroweak unification shows that the weak force can be seen to lack strength purely due to the distance scale it acts over. Similarly one may seek to add the strong force to the unification, such that the coupling constants of all three forces run at a higher scale to unify into one value. Proton decay has not been observed, with stringent limits on the decay time. This proton decay time is inversely proportional to the fourth power of the unification scale, such that the proton's stability suggests a scale very much larger than the TeV regime. The question of whether a unifying scale exists and under which proposed theory is still unanswered. The Higgs mass is very low compared the the unified or plank scales, the question of why is commonly known and the hierarchy problem[6]. Figure 2.6 shows fermion loops that add quantum corrections to the Higgs mass, especially from the top quark. The Higgs Mass corrections can be calculated as

$$\Delta m_H^2 = \frac{\lambda_f}{16\pi^2}\left[-2\Lambda_{UV}^2 + 2m_f^2 \ln\left(\frac{\Lambda_{\mathrm{UV}}}{\mathrm{m_f}}\right) + ...\right] \tag{2.11}$$

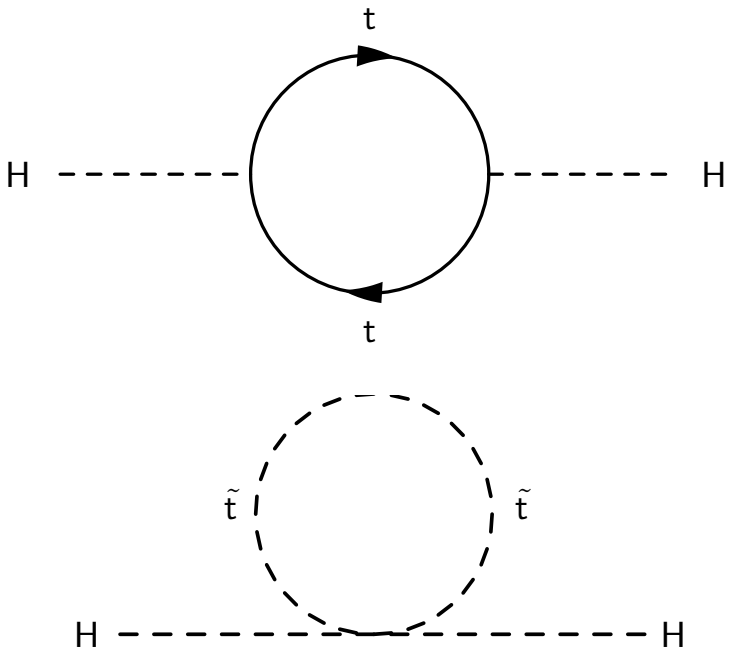

Figure 2.6: Illustration of the a top quark loop (top) contributing to the Higgs mass and the supersymmetric partner stop loop (bottom) that could cancel it.

where m_f are the fermion masses, λ_f are the fermion–Higgs couplings and Λ_{UV} is the cut off scale. To calculate a value that agrees with experimental bounds, limitations must be placed. One solution is that no high mass particles couple to the Higgs field, effectively lowering the cut off scale. A test of this solution with the LHC reach is to look for coupling of top and Higgs via ttH production. Alternatively, one could theorise cancellation terms for each of these contributions, as in supersymmetry shown in Section 4.2.

The existence and nature of dark matter is a major question outside the SM. The effects of dark matter have been well measured in galactic rotation curves, but none of the potential candidates have been observed. Some candidate particles would be best observed in dedicated dark matter experiments, but a small number could theoretically be produced and indirectly observed in collider experiments. One such collection of theories in supersymmetry (SUSY), a proposed partially broken symmetry between fermions and bosons. Under this framework, each Standard Model fermion has a partner boson, providing candidates for dark matter particles. Supersymmetry can also provide a solution to the aforementioned hierarchy problem[6], each fermion loop contribution to the Higgs mass is cancelled by the supersymmetric partner's loop, as shown in Figure 2.6. Collider searches have excluded supersymmetric particles with masses of under 500 MeV–1 TeV for many of the common regimes. For supersymetry to be useful as a candidate for

the dark matter and hierarchy problems, supersymmetry existing under the TeV scale is heavily favoured. The LHC is heavily engaged to focus on the supersymmetry scenarios still available in this regime. For more please see chapter 4.2.
In the following Section 2.3.1 it is seen that the Standard Model contains small amounts of CP violation, allowing for differing behaviour between matter and antimatter. However, cosmological models require much larger CP violating effects to allow for the initial matter–antimatter balance of the Universe to evolve into the matter universe we see today. Additionally precise CP measurments such as $B_s/B^0 \to \mu^+\mu^-$ decays performed at LHCb [7] can probe or limit new physics. This decay is tightly predicted with a small rate in the SM and any measured deviations from this value would provide evidence for BSM physics. Conversely, measurements with low event rates are capable of providing strict limitations on model such as SUSY [8]. As seen in Section 2.3.2, experiments have shown unusually low neutrino masses and the limitation of only three lepton generations, both of which have no current explanations.

2.3 Mixing Of States

2.3.1 Charge Parity Conservation

CP conservation refers to the symmetries under two combined operations on fields. Firstly C symmetry refers to conservation under the inversion of charge. Secondly, P symmetry refers to inversion of particle parity, functionally performed by flipping spatial co-ordinates in the Lagrangian. The combined CP symmetry is observed in QED and QCD, however experimental results such as neutral kaon decays shows violation in the weak interaction. Quarks within the kaons are capable of transitioning to other states, implying a mixing between the eigenstates of quarks q' and those quarks q that carry QCD interactions. These two sets of states are related by the CKM matrix

$$\begin{pmatrix} d' \\ s' \\ b' \end{pmatrix} = \begin{pmatrix} V_{ud} & V_{us} & V_{ub} \\ V_{cd} & V_{cs} & V_{cb} \\ V_{td} & V_{ts} & V_{tb} \end{pmatrix} \begin{pmatrix} d \\ s \\ b \end{pmatrix}, \tag{2.12}$$

where the elements V_{ij} can be expressed[6] in terms of three mixing angles $\theta_{13}, \theta_{12}, \theta_{23}$ and a complex phase δ_{CP}

$$\begin{pmatrix} c_{12}c_{13} & s_{12}c_{13} & s_{13}e^{-i\delta_{CP}} \\ -s_{12}c_{23} - c_{12}s_{23}s_{13}e^{i\delta_{CP}} & c_{12}c_{23} - s_{12}s_{23}s_{13}e^{i\delta_{CP}} & s_{23}c_{13} \\ s_{12}s_{23} - c_{12}c_{23}s_{13}e^{i\delta_{CP}} & -c_{12}s_{23} - s_{12}c_{23}s_{13}e^{i\delta_{CP}} & c_{23}c_{13} \end{pmatrix}, \tag{2.13}$$

with c_{ij} and s_{ij} denoting the cosine and sine of the mixing angle θ_{ij}. The complex phase enables CP violation in the Lagrangian whereas non-zero mixing angles enable quark flavour changes in weak interactions. No current measured effect of δ_{CP} is large enough to account for the matter antimatter asymmetry from astronomical observations and models[9]. Hence precision measurements that probe this value are very interesting and one of the main goals of LHCb is to probe this sector.

2.3.2 Neutrinos and Mass

Within the basic SM, neutrinos are assumed to be massless, completely right handed particles. However, the resolution of the so called solar neutrino problem suggests small but non zero ($\lesssim 1\,\mathrm{eV}$) masses for neutrinos. Fluxes of electron neutrinos from the sun were well predicted but Davies' famous Homestake experiment[10] measured lower fluxes on earth. Additional experiments[11] have corroborated this effect measuring electron–neutrinos oscillating flavour in–flight into muon-neutrinos. Oscillation occurs between the three flavours of neutrinos because the three (explicitly non-zero) mass eigenstates of neutrinos are not the same as the flavour eigenstates. These flavour ($\nu_{e/\mu/\tau}$) and mass eigenstates ($\nu_{1/2/3}$) are related by

$$\begin{pmatrix} \nu_e \\ \nu_\mu \\ \nu_\tau \end{pmatrix} = U_{\mathrm{PMNS}} \begin{pmatrix} \nu_1 \\ \nu_2 \\ \nu_3 \end{pmatrix} \tag{2.14}$$

where U_{PMNS} is the Pontecorvo-Maki-Nakagawa-Sakata mixing matrix[12]. The mixing matrix is dependent on three mixing angles and a CP violating phase[7]. Measurements of the Z boson widths have been used to place strong constraints on the number of

[6] by enforcing unitarity on the matrix while choosing quark phases.
[7] If neutrinos are their own antiparticles, two Majorana phases are included in the PMNS matrix.

non–sterile neutrino species to three[13]. There exists an unproven possibility for sterile neutrino flavours. The popular seesaw mechanism proposes the existence of heavy sterile neutrinos mixing with light neutrinos and motivating the unusual mass scales.

2.4 Phenomenology of High Momentum Interactions

High transverse momentum particles and interactions are commonly referred to as hard, with soft interactions for low momentum. Hard interactions involving proton beams consist of two main components, the hard scatter and the underlying event. The hard scatter refers to high energy collisions between partons, involving high momentum in the z direction and calculated using perturbation theory. The remaining partons are the underlying event and are not perturbative processes due to their low energy. To estimate these soft processes, Parton Distribution Functions (PDFs) are used. A PDF uses data to map the probability of a parton existing within a nucleus with a Björken–x momentum fraction at an energy scale Q^2. The production cross section $\sigma_{AB\to X}$, of particle X from colliding particles A and B

$$\sigma_{AB\to X} = \int \mathrm{dx_a dx_b f_{a/A}}\left(\mathrm{x_a}, \mathrm{Q^2}\right) \mathrm{f_{b/B}}\left(\mathrm{x_b}, \mathrm{Q^2}\right) \hat{\sigma}_{\mathrm{ab\to X}} \tag{2.15}$$

is a combination of the partonic cross section $\hat{\sigma}_{ab\to X}$ and the PDF functions for parton a/b carrying momentum fraction $x_{a/b}$ in each particle. Measurements from experiments are made at specific Q^2 values and evolved to other values using DGLAP Equations[14][15][16].

2.4.1 Simulation

Perturbative methods calculate cross sections and processes by adding small Hamiltonians to the solution from similar, yet solvable Hamiltonians. The effects of the small additions to the Hamiltonian are expressed in a power series. Cutting edge calculations vary between Leading Order (LO) to Next to Next to Leading Order (NNLO). Missing contributions to the partonic cross sections can be mitigated with a systematic uncertainty. Higher order terms contain phase space contributions which can change the event characteristics that a systematic cannot allow for. Parton shower techniques model these higher order contributions by calculating incoming/outcoming radiation of partons and photons from the main event particles. At every branch the probability of radiating a particle depends on the momentum fraction given. Final State Radiation (FSR) is evolved forward from

inital highest energy process to the successively lower Q^2 particles. The Initial State Radiation (ISR) is evolved backwards from the same process to maintain the showering to particles with lower Q^2 values. Once partons are produced in hard interactions they hadronise. The quark confinement property of the strong interaction, the free partons combine with $q\bar{q}$ pairs to form hadrons. These processes cannot be simply calculated using perturbation theory, so phenomenological models must be used.

2.5 Diboson Production

Diboson focused physics at a hadron collider is useful measurements of the SM, for hints at new physics and for improving the background estimation of other physics searches. This section will briefly outline the motivation for diboson searches and the theory behind WW production. The cross sections and other properties of diboson production are very good tests of the SM. The rates of the rare diboson processes can be used to constrain the internal parameters of the model. Furthermore, in historical searches and now measurements of the Higgs boson, diboson production provides important backgrounds. The $H \rightarrow WW$ decay channel has a large background from SM WW production and similarly in the $H \rightarrow ZZ$. In both these cases, the same intermediate diboson state is produced, hence the same decay products. Differentiation of the Higgs events is reliant on accurate estimations of the rate and kinematics of SM processes and as such diboson measurements aide these analyses [17, 18, 19, 20]. Triple gauge coupling arises when a single interaction vertex has three gauge bosons coupling to it. In the electroweak sector, both $WW\gamma$ and WWZ are allowed within the SM, however other combinations are not. Those not allowed within the SM are labelled anomalous Triple Gauge Couplings (aTGC). A large range of new physics theories are capable of enabling aTGC vertexes, for example MSSM models (see Section 4.2). The presence of aTGC would affect diboson production by increasing the cross section at high collision energy. Furthermore, the transverse momentum, p_T, of the bosons produced will be high, specifically one expects to see increased p_T in the leading momentum boson and hence of the leading lepton. In order to quantify if aTGC is indeed contributing to a diboson process, a precise grasp of the cross section is needed as well as good lepton momentum resolution. Finally, the effect of sea quarks and high momentum gluons onto diboson production can be used to help improve the worldwide PDF fits. This is especially true in LHCb, where diboson events include two partons with a large disparity in longitudinal momentum with respect to the proton centre of mass. This results in one large momentum parton and another

with very low momentum. This momentum is directly related to the momentum of the partons

$$x_{1,2} \sim \frac{\sqrt{s}}{Q^2} e^{\pm y} \tag{2.16}$$

where $\sqrt{s}$ refers to the sum of colliding particle energies in the centre of mass frame and Q^2 is the energy scale of the interaction, $O(10^4)$ GeV in diboson interactions. Rapidity y is a variable related to particle speed as $y = \tanh^{-1}(\mathrm{v/c})$. Whilst regions of high x values have been well measured by experiments such as HERA[21], however low x values are less well probed and are inaccessible to the LHC general purpose detectors In a GPD the angular coverage is larger, but does not extend to small angles parallel to the beam pipe. The two colliding partons need to have similar momentum for the collision centre of mass to take the event into the detector. Hence, a GPD has one region of x momentum space (for a given y value) that both partons will occur in. However, due to the unique angular acceptance of LHCb electroweak processes, one low x parton and one high x parton will involved. In this scenario, two distinct separated x planes exist for each parton. The lower X plane can access new parameter space as shown in Figure 2.7.
Three potential discovery channels are available; WW, ZZ and WZ in order of decreasing

Decay	Branching Fraction	Error on BR
$e\nu_e\ e\nu_e$	1.118×10^{-2}	1.955×10^{-4}
$\mu\nu_\mu\ \mu\nu_\mu$	1.147×10^{-2}	3.427×10^{-4}
$\mu\nu_\mu\ e\nu_e$	2.326×10^{-2}	3.974×10^{-4}
$l\nu_l\ h$	4.442×10^{-1}	4.160×10^{-3}
$h\ h$	4.544×10^{-1}	3.640×10^{-3}

Table 2.2: Branching ratios of Major WW decays, where h refers to hadronic decay.

cross section. The branching ratio of these diboson modes to leptonic states are 4.7, 1.5 and 0.5% respectively. In the first case, one would wish to measure the leptonic decays as these signatures are cleaner, with lower backgrounds than states with hadronisation of direct decay products. At leading order all Z decay products would be visible in a detector, hence Z decays are easy to identify by measuring the invariant mass of the two leptons produced. Indeed a final state with four clean, isolated high p_T leptons is unique and often used to calibrate lepton measurements. This is compared to each W decaying into a lepton and associated flavour neutrino, widening the invariant mass distribution.

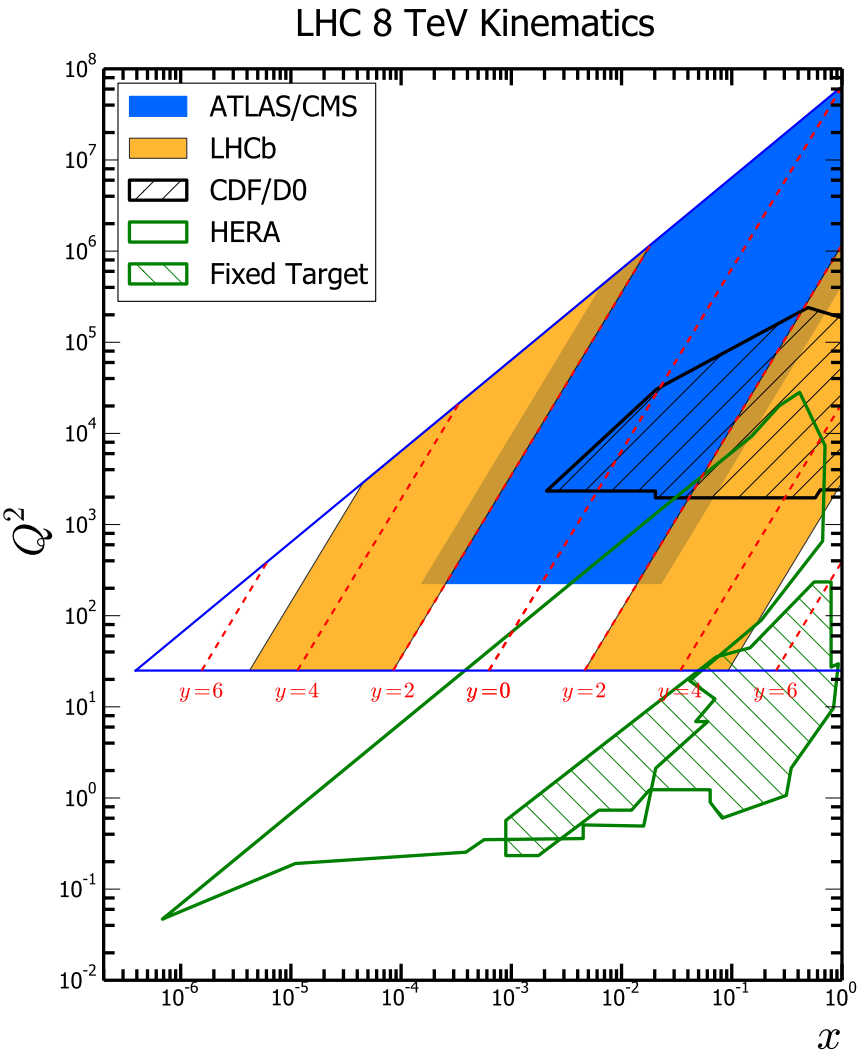

Figure 2.7: Plot showing the accessible region in the x–Q^2 range for LHCb and other experiments. Overlaid red lines show the position of the particles dependent on their rapidity $y = \tanh^{-1}(\mathrm{v/c})$. The low x region is uniquely accessible in LHCb. Adapted from [22] by S. Farry.

Additionally WW and WZ decays produced final states of two and three leptons that are produced in a larger range of background processes.
In the general purpose detectors, there are enough statistics to study all the decay ratios, with results being in agreement with the SM and no aTGC effects have been seen[23, 24, 25]. The ZZ measurements look for two pairs of high p_T leptons, each with transverse mass around the on–shell Z mass. WZ decays are complicated by their low leptonic BR and a large background contribution from events with leptonic tau decays. WW events use E_{T}^{m} and m_T (see Section 4.2) to identify neutrino signatures.
In the LHCb detector with the 2012 data run, the rates of diboson production are low. Table 2.2 shows the number of events expected to be produced in the 2012 run, before detector reconstruction. It is clear from these numbers that in the short term, WW is the most promising analysis. WW production is produced in the u and t channels by quark exchange between a quark and antiquark pair. These contributing quarks can be either valence up and down quarks or any of the sea quarks, as shown in Figure 2.8. Additionally, at NLO gluino–gluino production of WW pairs starts to contribute. Due to the missing p_T in the neutrinos, WW measurements are usually a rate measurement with some degree of irreducible, non–minimal background processes.

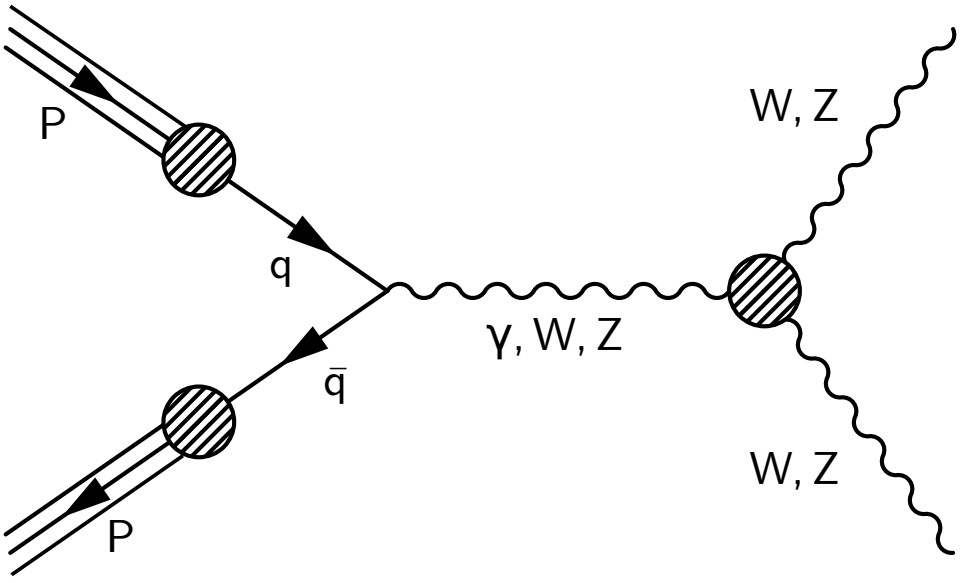

Figure 2.8: The Feymann diagram for Triple Gauge Boson production of dibosons.

Chapter 3

Overview of the LHCb Experiment

This thesis utilitises the proton collisions in the LHCb Detector to study the production of pairs of electroweak bosons. Protons are provided to the experiment by the Large Hadron Collider[26] (LHC) accelerator chain. The following chapter outlines both the LHC and the LHCb detector.

3.1 The Large Hadron Collider

The LHC is the world's highest energy particle accelerator, based at the European Organization for Nuclear Research (CERN) in Geneva. The 27 km circular tunnel, 100 m metres underground was previously used by the Large Electron-Positron (LEP) collider, which ran from 1989 to 2000. Removing the electron–positron accelerator to a new apparatus with pairs of protons principally allowed for collisions roughly seventy times more energetic.

3.1.1 Design Goals

One of the principle goals for the next collider at CERN was higher energy collisions. In the centre of mass frame of the colliding particles, the sum of both energies is equal to the square root of the Mandelstam invariant mass variable $\sqrt{s}$. The LEP apparatus peaked at $\sqrt{s} = 208\,\text{GeV}$. During the design period of the LHC the Tevatron experiment at Fermilab was pushing the TeV region, before end of operations in 2010. Linear configurations have a limited length over which to accelerate, whereas the circular alternative can loop round multiple times, increasing the effective acceleration length. In an accelerator, circular

motion is obtained using dipole magnets to bend the beam. The use of a LEP size tunnel in the TeV regime particles requires fields in the 10T region. Large magnetic fields in this range necessitate the use of cryogenically cooled apparatus/superconducting electromagnets. This magnetic field requirement presented one of the main technical hurdles for the LHC design and construction, as well as the main energy limitation.
Using non-composite particles such as leptons in the LEP experiments provided measurements with well defined initial energy states. The energy of collisions was tuned to the known mass of the Z^0 particle for precision measurements. When conducting a search for new physics, this approach requires large amounts of data taking at varying energy levels, especially for rare decays. Accelerating leptons at higher energies also proves difficult due to large energy losses due to synchrotron radiation. Charged particles bending under an orthogonal magnetic field emit synchrotron radiation. For each full orbit of a ring radius r, a particle with charge q at energy E will loose energy as [27]

$$\Delta E = \frac{q^2 \beta^3 \gamma^4}{3\epsilon_0 r} \tag{3.1}$$

where γ is the relativistic Lorentz factor, β is the particle's speed as a fraction of the light speed c and ϵ_0 is the permittivity of free space. In the relativistic limit, the γ and β factors are approximately E/m and 1 respectively. In this limit the energy loss can be expressed as

$$\Delta E \approx \frac{q^2 E^4}{3\epsilon_0 m^4 r} \tag{3.2}$$

where energy losses are inversely proportional to the fourth power of mass. Hence, at a given energy and radius, synchrotron radiation is much more limiting for lower mass particles. Protons are 1836 times heavier than electrons, therefore the energy loss in the same radius and energy orbit is $\sim 10^{13}$ smaller for the former. This highly limiting relation motivates any TeV scale collider using protons over leptons.
Individual partons within the hadrons will be the objects that collide, hence the event centre of mass energy will be $\sqrt{\hat{s}} = x_1 x_2 \sqrt{s}$, where x_1 and x_2 are the fractional momentum of the colliding partons. This provides a larger range of event energies for a fixed beam, increasing scope for physics searches. Unlike a lepton collider the lack of knowledge of the event energy decreases the potential for precision measurements.

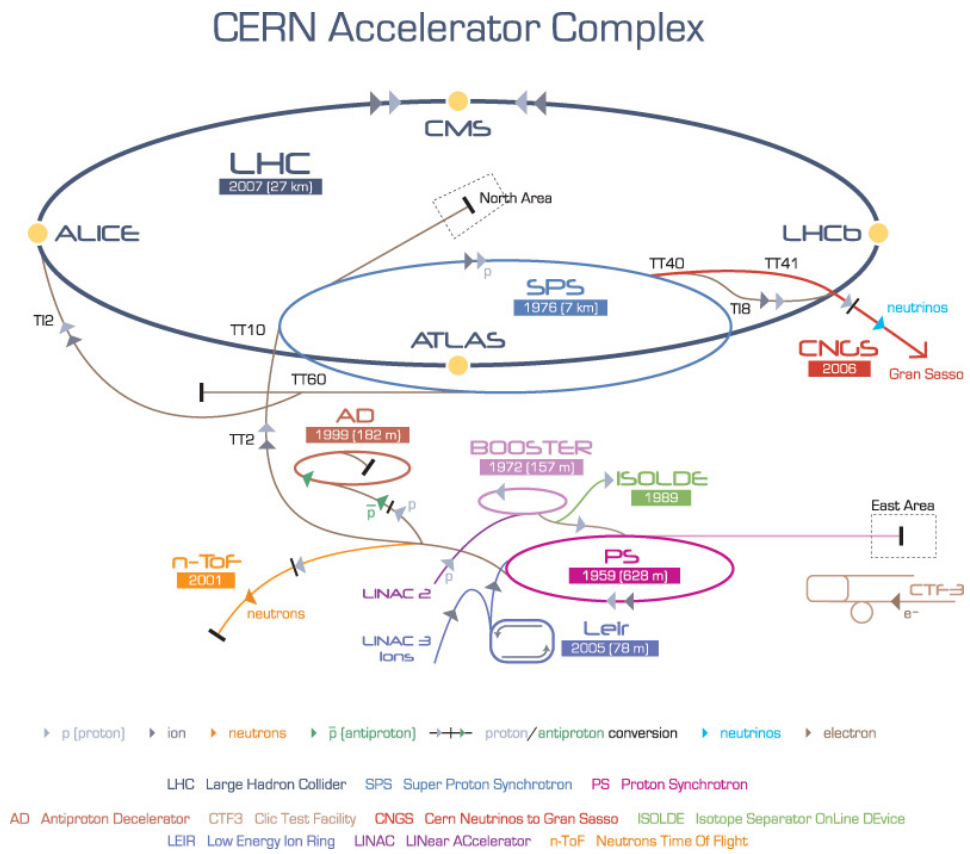

Figure 3.1: The proton acceleration system at CERN. Reproduced from [28].

3.1.2 The Accelerator Chain

The LHC design utilises a number of existing accelerators at the CERN facility to provide protons to the final ring as shown in Figure 3.1. Upgrades to the equipment were made to handle the increased number of protons and lower bunch spacing. Initially the LHC ran with bunch spacing (time between each bunch in the accelerator ring) of 50 ns, with testing underway to run at 25 ns allowing for double the collison rate in each detector. Protons are extracted from gaseous hydrogen and accelerated to 50 MeV in a linear accelerator (LINAC2). The protons then pass through three successively higher energy synchrotron rings; the Proton Synchrotron Booster, Proton Synchrotron and Super Proton Synchrotron. Radio-frequency (RF) cavities accelerate protons bunches, with quadrupole and dipole magnets focussing and bending the beam respectively. This results in a final beam of 450 GeV protons injected into the main LHC acceleration ring.

3.1.3 LHC Particle Acceleration

The LHC ring is a 27 km circular accelerator producing two identical, opposite direction beams of 2748 protons bunches at 3.5 TeV[1]. With particle beams at these energies, large magnetic fields are required to sufficiently bend the beam. Indeed, the current field strength of 8.6 T is the main limiting factor of LHC collision energy. This is provided by 1232 dipoles and over 8000 correction and focussing magnets, using a Niobium-Titanium superconducting alloy. This is achieved by cooling the whole apparatus to less than 2°K with the use of 120 tonnes of liquid helium. Bunches, separated by 50ns are collided at one of four collision points ATLAS[29], CMS[30], ALICE[31] and LHCb [32].

3.1.4 Luminosity

Integrated luminosity is a measure of the amount of data a collider experiment has gathered. The event rate R can be obtained via the instantaneous luminosity $\mathcal{L}$ with

$$R = \mathcal{L} \times \sigma \tag{3.3}$$

where σ is the cross section for a given process. For a particular process in a collider, one is usually interested in the time integrated number of events expressed in terms of beam parameters

$$N_{EVT} = \sigma \int_0^T \mathcal{L} \mathrm{d}t = \sigma \int_0^T f \frac{N_b^2}{4\pi\sigma_X\sigma_Y} \mathrm{d}t \tag{3.4}$$

where f is the beam crossing frequency, N_b is the number of protons per beam bunch and σ_X/σ_Y are the transverse beam profiles in the respective co-ordinates. A General Purpose Detector (GPD) often searches for new physics with very low cross sections, resulting in very infrequent events. Hence, it is very important for GPDs such as CMS and ATLAS to have high instantaneous luminosity. To achieve this goal, the LHC delivers bunches of numerous protons to each experiment. The average number of collisions per bunch crossing μ, for CMS and ATLAS in 2012 was around 30; individual events are subject to pile–up of collisions. This presents difficulties in isolating individual collisions to reconstruct. In a precision experiment focussed on B hadrons, where measurements of primary and secondary vertices are important, pile–up would present a major problem. Precision vertex information is used to measure the displaced vertices of decaying hadrons.

[1] In 2012 the machine was ran with increased 4 TeV beams and will eventually increase to 7 TeV.

Multiple interaction vertices decrease the vertex resolution in the first detector component, hampering B physics searches. Ideally, LHCb would produce a single interaction vertex at a time. To this end, the two incoming beams are defocussed for an offset collision and an average $\mu \simeq 1$. Events with multiple interaction vertices are not recorded as detailed in Section 3.2.6. Furthermore, the beam off-set is adjusted throughout a full LHC run. As the run progresses, the beam becomes depleted and the active collision area is increased to maintain a consistent instantaneous luminosity. This process, known as luminosity levelling, is illustrated in Figure 3.2.

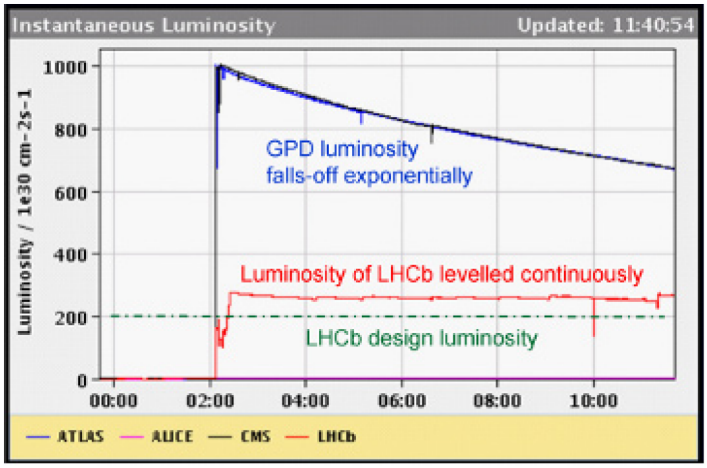

Figure 3.2: Example of the instantaneous luminosity at the four LHC experiments for a complete run. LHCb shows a constant value due to luminosity levelling. Reproduced from [33].

3.2 The LHCb Detector

LHCb is an experiment aimed at probing the physics of CP Violation, via the phase δ_{CP}. Additionally the experiment should be able to focus on rare decays of B and D mesons. To achieve these main goals, the detector must be efficient at identifying $b\bar{b}$ pairs. The dominant production of $b\bar{b}$ pairs is via gluon-gluon fusion and quark pair production. Collisions in the LHC are between partons with fractions of their proton's momentum. Hence, the momentum between colliding partons is frequently asymmetric in the direction parallel to the beams. This results in a substantial proportion of both b quarks moving in a highly forward direction. LHCb covers such a forward region,

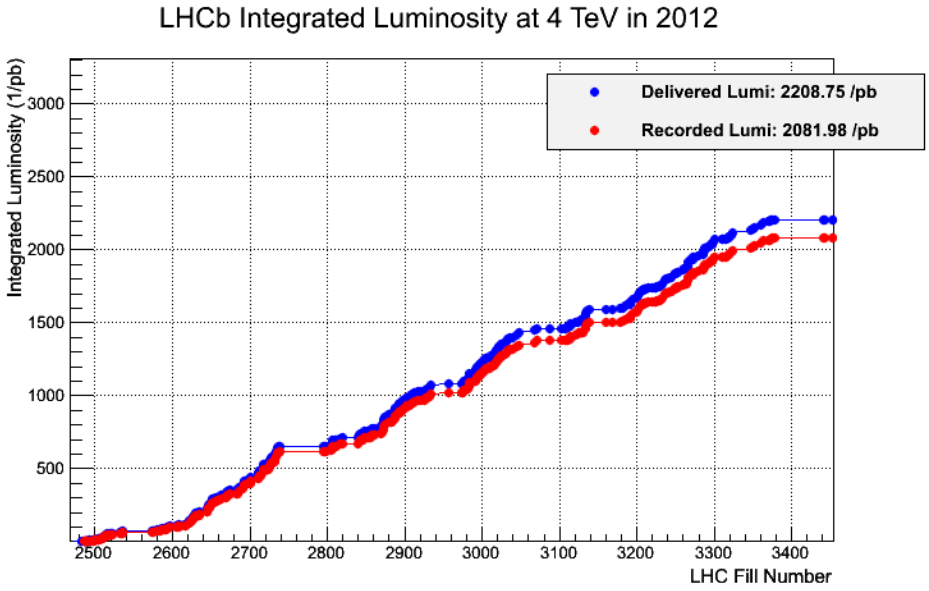

Figure 3.3: Plot showing the instantaneous luminosity delivered to to LHCb in 2012 and the amount recorded, as produced by LHCb Operations.

covering pseudorapidity[2] η, of between 1.9 and 4.9 η. In order to reconstruct these B particles, the detector needs to able to measure low momentum particles and accurately measure decay lengths.

3.2.1 Detector Layout

The LHCb collaboration uses the co-ordinate convention of the incoming beams parallel to the z axis, with the detector mounted in the forward z direction and the positive y co-ordinate representing the vertical. However, it is common to describe particle position in a variation of spherical co-ordinates; the radial distance R, the azimuthal angle ϕ, and the pseudorapidity η. The detector is constituted of layers of detectors from the collision point, as shown in Figure 3.4. These layers are the VErtex LOcator (VELO), Ring Imaging CHerenkov layer 1 (RICH1), Tracker Turicesis (TT), Tracker stations 1-3, RICH2, Electromagnetic and Hadronic CALOrimeters (CALO) and the Muon layers. Each layer is designed to measure specific characteristics of the outgoing particles which can be combined to reconstruct the full event. In between the Tracker Turicesis and the other tracker stations is a dipole magnet, bending charged particles in the y-plane.

[2]Pseudorapidity is a variable constructed using the angle θ between a particle's flight and the direction of the initial proton beam (z axis), such that $\eta = -\ln\left[\tan\left(\frac{\theta}{2}\right)\right]$. In the small mass and high speed regimes, pseudorapidity converges to rapidity. Rapidity is a preferable to θ angle as linear sums are Lorentz invariant.

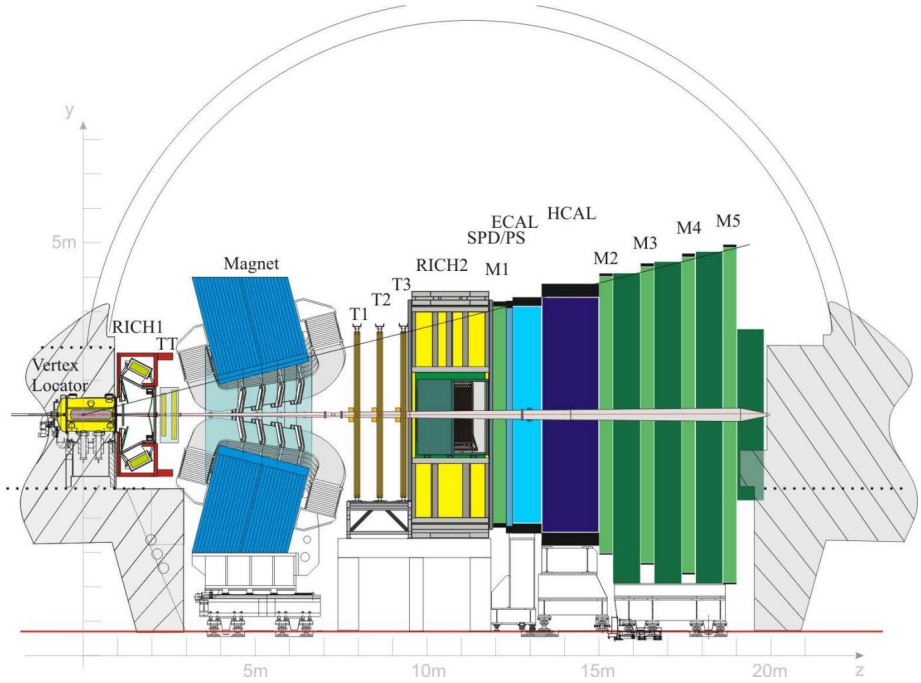

Figure 3.4: Cross section through the x-plane of the LHCb detector, with the beampipe along the z axis.

This magnet is non superconducting, offering a cheap, reliable build that is mechanically supported outside the experimental acceptance. This provides an integrated magnetic field path length, $\int \vec{B}.d\vec{l} \simeq 4.2$ Tm. Measuring the curvature of charged particles in this field, enables the experiment to quantify their charge and momentum. Two opposite polarities of the LHCb magnet are used, useful to double check the symmetry of the apparatus that is particularly important in CP phase measurements.

3.2.2 Tracking systems

Name	z position (m)	Resolution (μm)	Use in final reconstruction
VELO	-0.2 $\rightarrow$ 0.8	>4	Vertex Location and Tracking
TT	+2.33 $\rightarrow$ +2.63	$\sim$50	Triggering
IT	$\sim$7.8 $\rightarrow$ 9.4	$\sim$50	Small Angle tracking
OT	$\sim$7.8 $\rightarrow$ 9.4	$\sim$200	Higher Angle tracking

Table 3.1: Table showing the systems used in LHCb tracking.

Tracking in a particle detector refers to inferring the path of a charged particle by measuring the impact of it passing through a medium. Usually this is achieved by measuring a hit, where low energy electrons are produced by the passing particle. High rate precision tracking is predominately achieved using doped silicon semiconductors, such as in Figure 3.5. A large voltage is applied across a junction between two doped semiconductors, a charge particle passing through liberates electron−hole pairs. In the electric field, electrons drift towards the nearest cathode and can be counted as a hit.

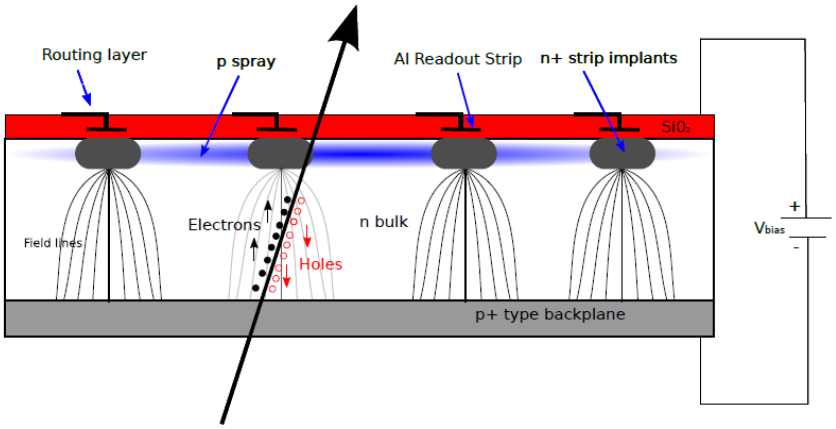

Figure 3.5: Schematic of a *n-in-n* in detector. A bulk of n-type doped semiconductor mounted on a p-type back plane with a reverse bias field. Small n-type implants at the top of the detector have higher doses than the bulk. Electron-hole pairs are formed as a charged particle passes through and drift in the applied electric field, with the former being detected at discrete aluminium readouts. Reproduced from [34].

Vertex Locator

The VELO is the component nearest to the collisions between the LHC beams. The principle goal of the VELO is to measure the primary vertex of the event. The primary vertex (PV) is the point where the interaction between two protons occurs, creating new particles. When one on these particles decays after a finite but small time, this creates a secondary vertex that can be used to reconstruct the particle. When dealing with B meson decays, it is important to be able to identify the decay length of the meson using these vertexes. To achieve high precision in the measurements, it is vital for the detector to be as close to the beam as possible. However, during the injection phase of LHC running, the beam halo expands by a factor of up to thirty. This expanded beam would irrevocably damage the detector, so the VELO instrumentation is designed in two parts which are retracted to 3 cm until stable beam conditions are met. Each of the two sides

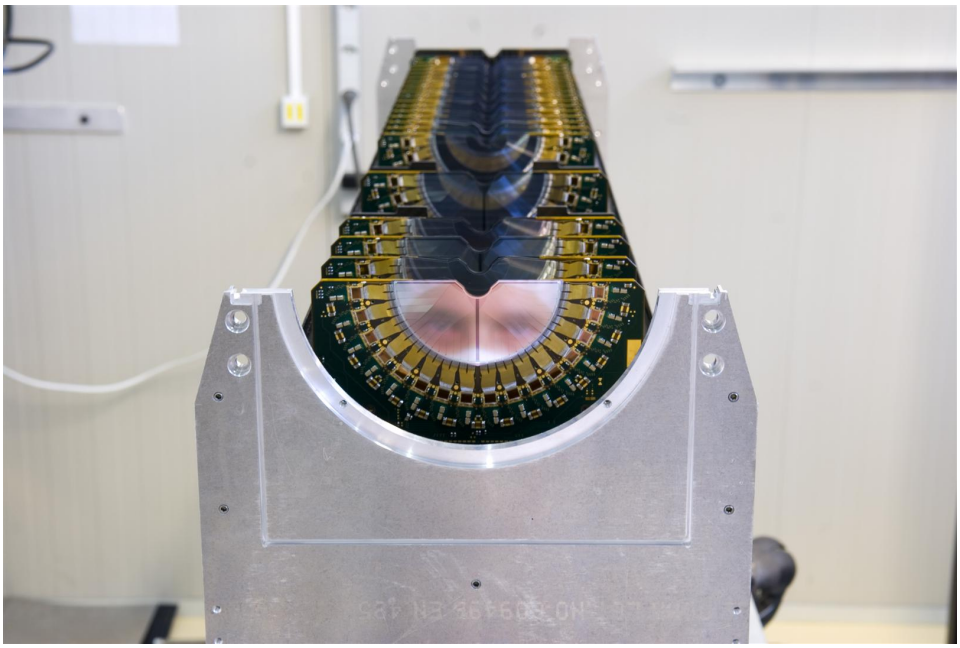

Figure 3.6: Photo of one VELO half in the assembly stage, displaying the semi-circular hole that sits 7 mm from the beamline. Another half was placed above to enclose the sensors around the beam. LHCb collaboration, CERN–EX–0610037

constitutes 21 stations over a z distance of 1m, covering an angle of 300 mrad horizontally and 250 mrad vertically. The whole apparatus operates in a vacuum, separated from the LHC vacuum by a thin aluminium foil. Each station has two silicon n+ on n sensors, containing 2048 strips of 300 μm. One sensor has semi-circular strips and another has stips radiating from the centre to measure R and ϕ respectively. This spread out geometry in the z co-ordinate, along with 4 μm point resolution enables the measurement of low angle tracks. This enables precise resolution of the Primary Vertex. In 2011 Z data[35], events with 25 tracks had an average resolution of 13 μm.

Tracker Turicesis

The TT is designed to measure all charged particle tracks before the magnet field for $|\eta| < 1.284$. In a thermally (5 °C) and electrically isolated chamber sits two tracker stations. The two stations are separated by 27 cm in the z co–ordinate. Each station has two identical layers of tracking, mounted in the (x,u),(v,x) configuration, with x representing a horizontal position and u,v representing a ± 5 ° rotation about the x axis. This low angle setup enables two adjacent layers to combine readout and provide accurate three dimensional hit placements without ambiguity. The stations are composed of

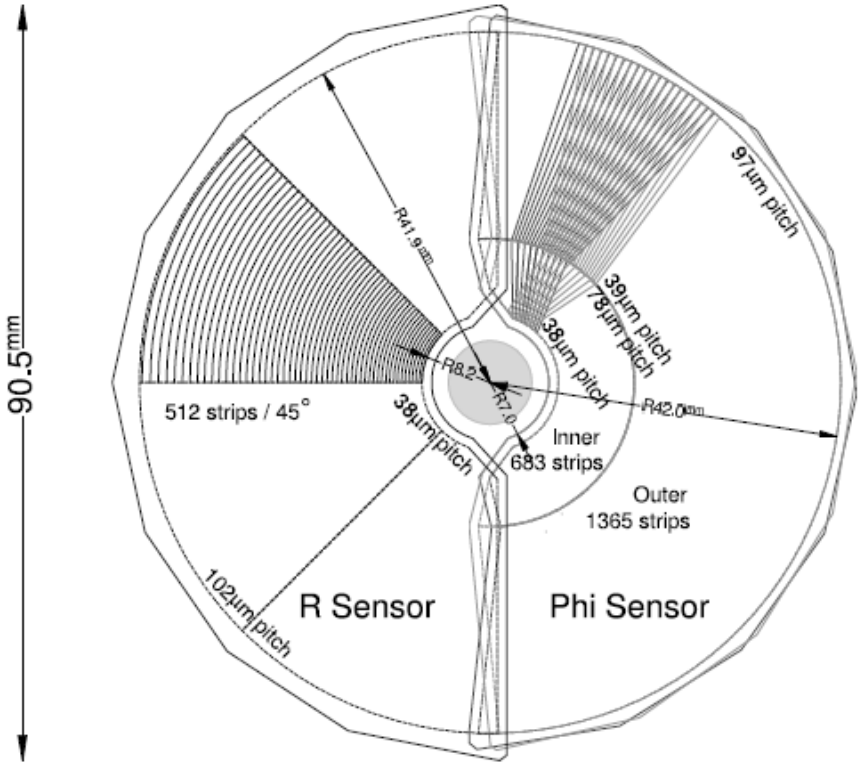

Figure 3.7: Geometries of the R and ϕ sensors of the VELO detectors, portraying the layout of a fraction silicon strips. The alternating patterns of the ϕ sensors are shown overlapped. Reproduced from [32].

9.64 cm wide by 9.49 cm long, single sided p^+ on n chips. Each chip has 512 readout strips with pitch of 183 μm. Rows of seven sensors are constructed, with $\sim$1 cm displacements in the z coordinate to negate any gaps in acceptance due to instrumentation. The first two stations have seven rows and the last two have eight, the larger target area needed for the same angular acceptance.

Inner and Outer Trackers

After the particles pass through the magnetic field they are tracked again by two systems, the silicon Inner Tracker in the high flux areas and the straw tube Outer Tracker in the larger area of low flux. Each Inner Tracker station contains 4 boxes as shown in Figure 3.8.

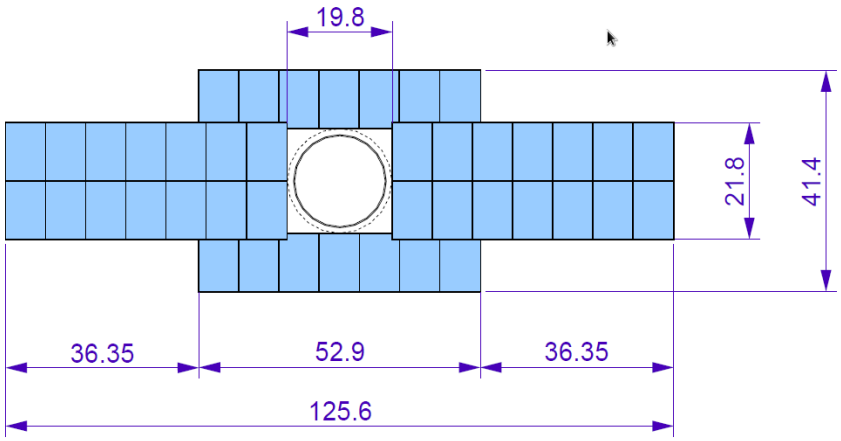

Figure 3.8: Layour of the x layout of a Inner Detector Tracker box. Dimensions in centimetres refer to the distances over which the silicon is able to track particles. Reproduced from [36].

Tracking Algorithms

Track Type	Systems used	Track Uses
Long Tracks	All	The Best Quality Tracks Available
VELO Tracks	VELO	No Momentum but has Backward Tracks
Upsteam Tracks	VELO & TT	Used with RICH1 for Low Momentum Particles
Downstream Tracks	TT & OT	Tracks Particles Outside VELO Acceptance
T Tracks	T Stations	Used with RICH2

Table 3.2: Table showing the types of tracks formed in LHCb.

Tracks are identified in the detector by combining a number of discrete hits, described by states $\bar{x}$ defined by

$$\vec{x} = \begin{pmatrix} x \\ y \\ t_x \\ t_y \\ q/p \end{pmatrix}$$

where x and y are the Cartesian co-ordinates as defined in Section 3.2.1, t_x and t_y are the gradients of the x and y planes with respect to the z axis, such that $t_x = \frac{dx}{dz}$ and $t_y = \frac{dy}{dz}$ and q/p is the charge divided by the scalar momentum. Six pattern recognition algorithms are used in the following order to reconstruct tracks from the $\bar{x}$ states:

VELO Seeding: Sequential VELO layer hits are used to create a straight line path. Surrounding layers are then searched for matching clusters. This process identifies VELO seeds with information on PVs and backwards tracks, but no momentum information. These seeds feed into the subsequent algorithms.

T Station Seeds: The T station information is used to construct additional seeds. At this point charged particles have been been bent in the y direction by the magnetic field, so seeds are recorded only in the (x, z) plane.

Forward Tracking: VELO seeds are matched to single T station hits. If a match is found, surrounding hits are clustered and a momentum calculation is possible.

Track Matching: VELO seeds unused from Forward Tracking and T Station seeds are extrapolated to the magnet region. When a match between two seeds are found, TT hits are scanned to be added to the track.

Upstream Matching: Further leftover VELO seeds are extrapolated to the match hits on the (y, z) plane of the TT. When a seed momentum matches that of three TT hits a track can be formed.

Downstream Matching: Leftover T Station Seeds are matched to TT hits in a method similar to Upstream Matching.

Output from the pattern recognition algorithms are fed into a Kalman filter to finalise trajectories. The fitter iterates over individual states and detector components to optimise the tracks while taking into account scattering and material interactions. Unlike a simple least squares fitter, the Kalman filter approach has the ability to discard problematic hits from detector noise[37].

3.2.3 The Ring Imaging Cherenkov Detectors

Extremely high momentum particles can travel faster than the local speed of light in a medium. When this occurs, the particle photons form a cone of radiation, known as Cherenkov radiation. The angle θ_c of this radiation cone can be related to the particle

velocity v by

$$\cos\theta_c = \frac{c}{\eta v_p} \tag{3.5}$$

where c is the speed of light and η is the refractive index of the medium. This velocity can be combined with a momentum value from the tracking systems of the experiment to extract the particle mass. This discriminant is particularly useful for the $B \to h^+h^-$ decays, where h are charged hadrons such as pions and kaons. However, these systems are also used to improve lepton tagging. Two detectors, RICH1 and RICH2 provide this information in LHCb. A schematic design of the two detectors is shown in Figure 3.9. Both detectors use high quality spherical mirrors to focus the conical light onto photo-detectors outside of acceptance. In RICH1, two mediums are used to induce Cherenkov radiation. An initial silicon aerogel target and gaseous C_4F_{10} in the bulk are used for low and medium momentum particles respectively. This detector is instrumented over the full LHCb range of 25–300mrad and is placed as near as possible to the collision point to reduce the amount of interaction material needed. RICH2 has a smaller 15–120 mrad acceptance and is situated after the tracking systems. RICH2 uses a mono–gaseous C_4F medium to produce light in the higher momentum range. The Cherenkov angle resolutions at 7 TeV [38] are 5.6 mrad for the aerogel medium, 1.62 mrad for C_4F_{10} and 0.68 mrad for the C_4F. Using this information, kaons in the 2-100 GeV range can be discriminated from pions with ∼95% efficiency and with misidentification fraction ∼10%.

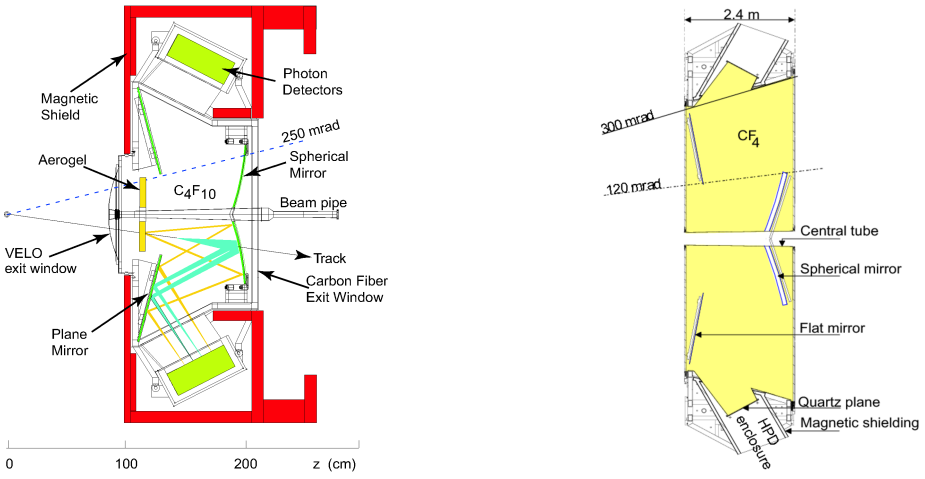

Figure 3.9: Schematics of the RICH1 (left) and RICH2 (right) detectors at LHCb, from [39].

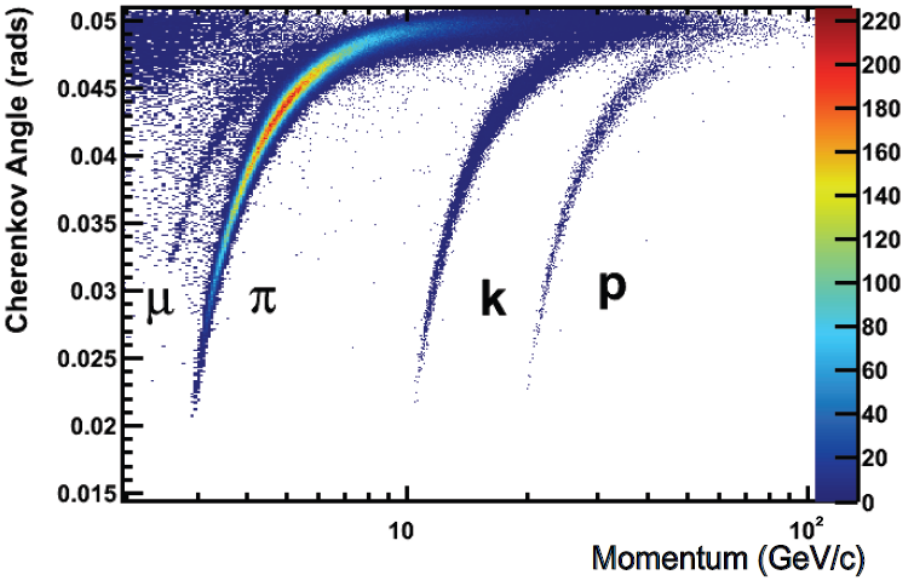

Figure 3.10: Recontructed Cherenkov angle with the C_4F_{10} material in the RICH1 detector. Curves for muons, pions, kaons and protons are labelled. Reproduced from [38].

3.2.4 Calorimeters

Calorimeters aim to record energy from showers of secondary particles arising from interactions with matter. Electromagnetic showers are due to Bremsstrahlung[3] of charged particles or pair production, characterised by the radiation length of the material X_0. Hadronic showers arise from strong interactions, and are usually more complex due to their higher multiplicity and inelastic nature. The nuclear absorption length λ_l that defines hadronic showers is typically greater than X_0, enabling the separation of the two shower types. LHCb uses sampling calorimeter designs where layers of scintillator are detection material containing wavelength shifting fibres.

The Electromagnetic CALorimeter (ECAL) contains layers of 4 mm scintillator tiles alternating with 2 mm lead layers in the Z direction, covering twenty five radiation lengths. Sixty-six rectangular modules are used containing 4.04×4.04, 6.06×6.06 and 12.12×12.12 cm square cells at central, middle and outer angles to account for decreasing occupancies. The ECAL energy resolution is found to be $\frac{8\%}{\sqrt{E}} \oplus 0.8\%$. To enable increased electron isolation, two additional components are placed before the main ECAL, the Scintillating Pad Detector (SPD) and the PRe-Shower (PRS). Separation by a 15 mm lead block, representing 2.5 X_0, enables the two components to measure

[3]When charged particles such as electrons are bent in the magnetic field, they emit photons known as Bremsstrahlung. This occurs in a material poor region so is free of interactions, so the position of these photons is easily predicted and matched.

electron tracks before and after initial material effects, enabling identification of pion background. Photons as neutral particles should not form tracks and should deposit in the ECAL via electron–positron pair production. However, tracks may exist that could feasibly be attributed to the photons ECAL clusters. A position estimator χ^2_γ is formed between ECAL deposits and any long extrapolated tracks matched. Charged particles exhibit peaks at small values of this position estimator and hence photons are identified by having a value $\chi^2_\gamma > 4$. Next an electron identification variable χ^2_e is formed using χ^2_γ and the ratio of the energy of the charged ECAL cluster to the momentum of the closest track. Furthermore to reject photon mis-identification, photons from the previous step are fitted as possible Bremsstrahlung radiation.
The Hadronic CALorimeter (HCAL) consists layers of scintillator aligned parallel to the beam axis separated by 1 cm lead absorber layers. Square cells measuring 13.13×13.13 and 26.26×26.26 cm make up 52 modules contributing to 5.6 nuclear absorption lengths of the medium. The HCAL energy resolution is found to be $\frac{6\%}{\sqrt{E}} \oplus 9\%$.

3.2.5 Muon systems and reconstruction

Typically, muons shower much less whilst passing through calorimeters than other particles. Indeed muons are the only charged particles to survive passage through large amounts of absorption material. In order to identify and measure these muons 5 extra layers of tracking, known as Muon layers, are used. The first layer M1 is situated before the calorimeters, with four more layers at the outside of the detector separated by 0.8 m blocks of iron to further weed out hadronic backgrounds. Charged muons passing through the muon systems are detected by gas detectors. Multiwire chambers are used throughout with the exception of the innermost section of the M1 layer, where a triple gas electron multiplier is used to cope with high occupancy. The first three layers have a greater spatial resolution leading to more precise momentum reconstruction. The final two layers have only half the spacial resolution, but are more effective at confirming candidates are truly muons. The final station M5, is situated at twenty nuclear absorption lengths, drastically reducing the probability of all other charged particles reaching this point. However, muons with $p_T > 5$ GeV can reach this point to be identified. The combined performance of the layers resolve muon transverse momentum to within 20% over angles of 20–206 mrad in the bending plane. Multi-Wire Proportional Chambers (MWPCs) are used in all but one of the twenty regions [68]. In the innermost region of M1 (M1R1),

triple-GEM (Gas- Electron-Multiplier) technology is used. This is because of its increased radiation hardness which allows it to cope better with the high particle flux in this region

3.2.6 Triggering Events

The LHC produces events at high rates such that it is not possible to totally record all collisions. The reduced recording rate is due to limitations of disk writing speed and total data storage capacity. The majority of collisions consist of two partons inelastically scattering; interactions unlikely to produce many secondary particles interesting for analysis. Trigger systems filter out these events and aim to record events with elastic collisions producing secondary particles. The LHCb trigger chain filters the initial 10 MHz event rate to record a final 2 KHz rate to disk. The first part of the chain is the Level–0 (L0) hardware based trigger, operating with a 4 μs window to reduce the event rate to 1 MHz. The LO trigger consists of four parts:

Pile Up: This pile–up system is in place to veto events with more than one primary interaction using VELO sensors. Two VELO R–geometry sensors are placed upstream of the VELO and perpendicular to the beam axis. Assuming the vertex originated from the beam axis it's z position can be estimated using

$$z_v = \frac{kz_a - z_b}{k-1} \tag{3.6}$$

where r_a and r_b are radial positions corresponding to z positions z_a and z_b on the A and B planes and k is the ratio $k = \frac{r_a}{r_b}$. Every peak in the z_v distribution signifies a separate interaction vertex. If more than one peak exists in an event it is veto'd.

Calo: The Calorimeters, in zones of 2 $\times$ 2 cells, are used to select the highest E_T electron, hadron, photon and neutral pion. Each of these objects is then fed into the L0 trigger decision. Firstly high E_T deposits in the Calorimeters are grouped together (with only HCAL contributing to hadron candidates). Secondly, ECAL contributions are combined with PRS/SPD to separate out electrons, photons and neutral pions. Lastly total E_T in the HCAL and SPD multiplicity are stored, so that events with large number of final particles can be rejected to save processing time.

Muon: The L0 muon trigger is formed without the use of the tracking systems to ensure hasty decisions. A straight line is made between the PV and M3 hits and extrapolated to find additional hits in M2, M4 and M5.

Decision Unit: The decision unit combines information from the L0 systems and passes events to the High Level Trigger (HLT) if one of the following candidate conditions is met: One high p_T muon, two lower p_T muons, a high E_T hadron, electron, photon or neutral pion.

The HLT trigger is a software based decision, using the lower output rate from the L0 decision unit. Two thousand nodes implement two successive C++ event filters. Firstly, HLT1 uses L0 output directly, using additional time to refine the decisions made. Muons form an exception, where a new full reconstruction is used to extrapolate and match $> 3\,\text{GeV}$ tracks to compared to the L0 decision. HLT2 takes these decisions and performs an almost complete global reconstruction. A simplified build of the Kalman filter is used due to time constraints. A list of basic particle requirements is collated from analysis group submissions within the experiment. Events passing one or more of these requirements are then written to disk.

3.2.7 Software

To facilitate analysis of recorded data, LHCb uses the Gaudi[40][41] software framework to produce the Data Summary Tables (DSTs) that can be analysed offline. The GAUSS application is used to control external Monte Carlo generators such as PYTHIA[42], to produce simulations of various known or theorised physical interactions occurring in collisions. It further uses the GEANT4[43] application to simulate the propagation of particles through the detector mass. In the case of this simulation, the Boole application uses test beam data to ape reconstruction of electric readout from these events. In data, the Brunel application reads the recorded detector data of tracks, deposits and vertices to create proto–particles, unidentified tracked objects with RICH, CALO and Muon ID information attached. These proto-particles are read in offline analysis using the DaVinci application, forming particle states from proto–particles and selecting events on analysis based criteria.

Chapter 4

Supersymmetry searches using the ATLAS detector

Before instigating the analysis on diboson production at LHCb, I worked on the ATLAS experiment. During this time, I engaged in experimental shift and service task work as well as engaging in the supersymmetry (SUSY) group on the ATLAS experiment. The following chapter will outline the ATLAS detector, the basics of SUSY theory, the phenomenology of a third generation SUSY search and the student's role in the group.

4.1 ATLAS Detector

The ATLAS detector, unlike LHCb, is a GPD capable of SM measurements as well as a large programme of new physics searches. The most obvious design difference is the almost 4π rad angular acceptance. The ATLAS detector is a 25m diameter, 44m long barrel shaped apparatus with the interaction point in the centre, as portrayed in Figure 4.1. Concentric layers of detector are placed around this interaction point, surrounding it. These detector layers are similar in function to those described for LHCb (see Section 3.2.1) and as such will be only briefly outlined below. The ATLAS inner detector consists of three layers covering $|\eta| < 2.5$, each divided into a central barrel and end caps, as portrayed in Figure 4.2. The first two layers consist of pixel and strip silicon semiconductor detectors, whereas the final layer is a straw–tube detection system, known as the Transition Radiation Tracker. This tracking system is based inside a 2T solenoid magnet to enable vertex location and track curvature measurements. These systems have maximum position resolutions of $O(10\mu\text{m})$ in $R - \phi$ and $O(100\mu\text{m})$ in z. The ATLAS

ECAL coverage of $|\eta| < 4.9$ is split again between barrel and end caps. Lead absorption plates are threaded with liquid argon detection material in three layers. These three layers enable high granularity and avoid shower leakage into the HCAL. Similarly the HCAL uses steel and scintillating tiles to detect hadronic particles, except in the end caps where liquid argon is again used. The calorimeters provide up to 9 λ (interaction lengths) of material throughout its coverage. The muon and magnet system envelopes the rest of the detector. Three superconducting toroid magnets provide an orthogonal magnet field to the muon trajectories as well as the experiment's acronym. The muon spectrometer consists of a mix of drift tubes and cathode strip chambers to momentum resolutions of 3% at 100 GeV and 10% at 1 TeV. Finally, interspersed with the muon system are fast acting plate and gap chambers to detect muons for the triggering system. The ATLAS experiment can use high multiplicity events, unlike LHCb which uses luminosity levelling. This means for each bunch collision, there are multiple events per crossing. Good vertex correction is essential for separating events in this environment, as well as data driven corrections for pile–up of events.

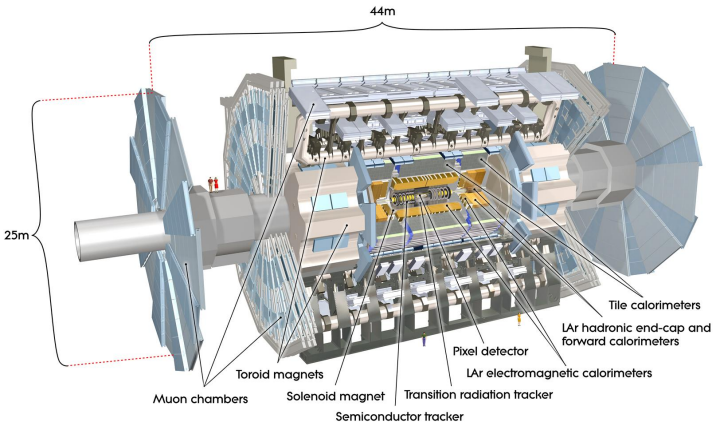

Figure 4.1: Diagram of the layout of the ATLAS detector, with cross sectional view of the centre of the detector and collision point.

4.2 Supersymmetry

Supersymmetry is a branch of 'Beyond the Standard Model' theories based on a proposed symmetry relation between fermions and bosons. In this regime every particle has a super–partner with half integer spin difference. The other quantum numbers are shared between

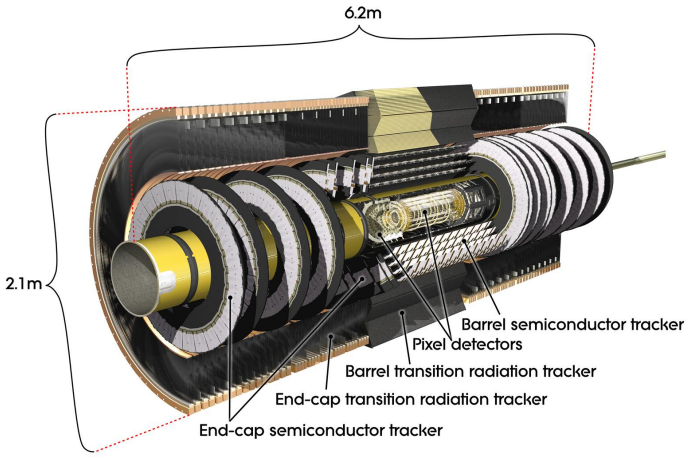

Figure 4.2: Diagram of the ATLAS inner detector layout, including the layers of semiconductor and TRT detectors in both the barrel and endcaps.

SM Particles	SUSY Partners	Name convention
g	$\tilde{g}$	Gluino
γ Z^0 h^0 H^0	$\tilde{\chi}_1^0$ $\tilde{\chi}_2^0$ $\tilde{\chi}_3^0$ $\tilde{\chi}_4^0$	Neutralinos
W^+H^+	$\tilde{\chi}_1^+$ $\tilde{\chi}_2^+$	Charginos
e μ τ ν_e ν_μ ν_τ	$\tilde{e}_R$ $\tilde{e}_L$ $\tilde{\mu}_R$ $\tilde{\mu}_L$ $\tilde{\tau}_1$ $\tilde{\tau}_2$ $\tilde{\nu}_e$ $\tilde{\nu}_\mu$ $\tilde{\nu}_\tau$	sleptons (e.g selectron)
q (with q)	$\tilde{q}_R$ $\tilde{q}_L$	squarks (e.g stop)

Table 4.1: Table of Minimal SUSY theory Particles. Here there exists not one Higgs state, but a group of light (h), and heavy (H) states. Additionally, the partners of gauge bosons can mix; the neutral states into the Neutralinos and the charged ones into Charginos. The partners of left and right handed fermions are independent bosons, so are named separately. The tau, bottom and top particles have large masses, such that the right and left handed components mix into two distinct mass eigenstates.

the particle and super–partner, at least when SUSY in unbroken. On a mechanical level one can view this as an extension of the symmetry principles used with success within the SM as seen in Section 2.2. The most basic set of SUSY models are the Minimal Super Symmetric Models (MSSM). Table 4.1 shows the SUSY particles for this model with an explanation of the mixing of states that occurs. The existence of super-partners gives rise to a solution to the hierarchy problem as mentioned in Section 2.2.5. When SUSY is introduced, the super-partner of a fermion has a Higgs loop as shown in Figure 2.6 that cancels out that of the fermion. To cancel the terms in Equation 2.11 one has

terms arising from superpartners,

$$\Delta m_H^2 = 2 * \frac{\lambda_S}{16\pi^2}\left[\Lambda_{UV}^2 - 2m_s^2 ln\left(\frac{\Lambda_{UV}}{m_s}\right) + ...\right] \tag{4.1}$$

with λ_S as the Higgs scalar coupling to a particle of mass m_s. If this scalar coupling equals the Higgs–fermion coupling λ_f then terms in the cut–off scale cancel, with a Higgs mass $O(100\,\text{GeV})$. However, for this solution to be viable, the scale of soft SUSY breaking must be not greater than 1 TeV.
In unbroken SUSY the mass of a particle and super–partner are degenerate. However, searches for degenerate mass super–partners have excluded this possibility. To build an effective model with non-degenerate mass, the theory must contain terms in its Lagrangian formation that break SUSY. However, large SUSY breaking removes preferable characteristics of the theory, such as containing dark matter candidates. Hence one induces a soft-SUSY breaking[44]. For illustrative purposes, one can discuss minimal supergravity (mSUGRA) in some detail, where the parameters define the model. These parameters are shared amongst many theories and can be used to define the signals used and the exclusion reach. The mSUGRA models are extensions of MSSM with SUSY breaking mediated by gravitational effects. In this framework at some large unification scale we have boundary conditions:

- The gauge couplings of electromagnetism, the weak and strong nuclear forces unify at a large scale, which is in agreement with the LEP results for running of couplings.
- Unification of the gaugino masses, the super-partners of SM gauge bosons, into one parameter $m_{1/2}$.
- Unification of scalar masses into one parameter m_0.
- Unification of trilinear couplings of quarks into one parameter A_0.

These last three values, along with $\tan(\beta)$ and μ form the parameters that fully describe the model. β is the ratio of the vacuum expectation values of the light and heavy Higgs fields and μ the Higgs-Higgsino mass parameter. The low number of free parameters lends this theory to specific interrogation in the experimental data.
Phenomenological constraints can be applied to the soft SUSY breaking [45], such as small mixing between sfermion families with minimal flavour violation. These are commonly known as phenomenological MSSM or pMSSM and are used to manually select models to study for particular searches. Relevant here are pMSSM with light third generation quarks. One assumes at large scales (i.e. the Planck scale) all sfermion masses are degenerate, but that at lower scales the masses diverge due to running of the masses as

the energy scale changes. The Yukawa coupling mass terms for squarks are related to their partners' mass (ie are they comparable to the Higgs vacuum expectation value), hence these terms are negligibly small for the first two families[6]. The running of these two generations of squark mass is mainly dependent on gauge interaction terms, leading to large masses. For the sbottom and stop squarks the Yukawa re-normalisation group acts to mix the left and right squark term via a standard 2×2 mixing matrix, parametrised by $\tan\beta$. Due to this mixing, the stop and sbottom quarks occur not as q_L and q_R but as two mixed states with differing masses, q_1 and q_2. If $\tan\beta > 5$, the Yukawa effects are large enough to noticeably oppose the gauge interaction effects at low scales and this leads to third generation squarks with masses lower[46] than the other families. Crucially for pMSSM models, the cross section is largely dependant on the sparticle mass hierarchy, so experimentalists can quote cross section exclusions that are somewhat model independent. This type of mass based exclusion is hence useful for a wide range of theory introspection and application, regardless of model specifics.
The gluino is a colour octet fermion so it cannot mix with other MSSM particles. Due to this absence of mixing it is usually assumed that the gluino is heavier than the other gauginos. In such mass hierarchies, decay chains will be gluinos decaying into either $\tilde{b}$ or $\tilde{t}$. Low mass squarks will have less kinematic constraints and thus yield higher cross sections, increasing the potential number of signal events for analysis.
In a general SUSY model, there exists the possibility for baryon and lepton number non-conservation. However, experiments such as proton decay searches place exclusion limits on these processes. Ideally one wishes to construct a theory consistent with these implications of the observations, but without simply imposing conservation. For example, baryon or lepton number are seen to be violated by Bell-Jackiw anomailes[47]. SUSY connects particles of integer $|I\rangle$ and half integer $|H\rangle$ spin states; $Q|I\rangle = |H\rangle$. The Lorentz group is inherently a spin group and acts separately on bosons and fermions

$$L|I\rangle = e_1|I\rangle \text{ and } \mathrm{L}|\mathrm{H}\rangle = \mathrm{e}_2|\mathrm{H}\rangle$$

with $e_1 \neq e_2$. So considering the action of both operators on an bosonic state

$$\begin{aligned} LQ|I\rangle &= L|H\rangle = e_2|H\rangle \\ QL|I\rangle &= Qe_1|I\rangle = e_1|H\rangle \\ LQ|I\rangle &\neq QL|I\rangle \end{aligned}$$

It can be seen that they do not commute. One can, however, choose a special case of U(1) continuous symmetry, denoted R-symmetry, that commutes with the Lorentz group, but whose commutator with SUSY is just Q, the SUSY operator. Considering the R operator, $R|F\rangle = q|F\rangle$ whilst substituting in the basic SUSY operator Q

$$R|B\rangle = RQ|F\rangle = ([R,Q] + QR)|F\rangle = (q+1)|B\rangle$$

one can infer that the R charge of the boson is one more than the fermion. However, having worked to achieve these requirements, a number of consequences occur that are not desirable for a physical theory given prior knowledge. To enable the see–saw mechanism, commonly used to motivate small SM neutrino mass[48], an R parity violating Lagrangian term is needed. Furthermore, there is no longer a possibility of soft SUSY breaking, which had removed undesirable baryon and lepton number violating terms.
Instead of choosing a continuous symmetry, one can choose to constrain to a discrete symmetry, ie one with a fixed value of α, the generator of the group. Specially, for R Parity one chooses $\alpha = 2\pi$, $e^{i\alpha/2} = -1$ so that Higgsinos are invariant under the R Parity transform. Furthermore, the SM particles, P, transform as $P \rightarrow -P$, such that every term in the Lagrangian has even numbers of -P terms (superpartners). One defines the R-Parity quantum number as,

$$R_p = (-1)^{(3[B-L]+2S)} \tag{4.2}$$

where B, L and S stand for baryon number, lepton number and spin respectively. This quantum number is 1 for any particle and -1 for its super-partner. So, with R-Parity conserved, at any interaction vertex the number of superpartners can only change by a even number. Hence a superparticle cannot decay into SM particles only. In the rest frame of the lightest superpartner, it has insufficient mass to decay into another superpartner. This particle is referred to as a stable Lightest Supersymmetric Particle or sLSP. In most of mSUGRA space the LSP is suggested to be the lightest neutralino, a mass eigenstate composed of a mixture of the two neutral gauginos and the two neutral Higgsinos. This is a neutral state, leading to no EM interactions in the detector and hence making it a suitable dark matter candidate.
If a stable-LSP were to be produced in proton-proton collisions in the ATLAS detector it would not interact with the detector in a meaningful way. This prohibits the direct detection of such particles by the detector systems. In a general purpose detector, with almost full hermeticity, E_{T}^{m} or related variables can be utilised. E_{T}^{m} is the total missing transverse energy in an event, found by summing all the transverse momentum vectors.

The presence of large E_{T}^{m} values could be used to identify particles that take momentum away from the event without being detected. These particles include, but are not limited to, LSPs. To use the E_{T}^{m} variable, any particle misidentification or detector deficiencies must be known well. The status of the detector from early running onwards suggest that expected MC simulations match the found E_{T}^{m} in data[49]. To adequately search for LSPs one must quantify other potential sources of E_{T}^{m} and possibly provide kinematic cuts to minimise these backgrounds. Details of the methods used within a light stop analysis are detailed in Section 4.4.

4.3 Cross Section Calculation

Using data recorded in 2011 and 2012, analyses aimed to expand into new processes, as well as new kinematic regions of already studied channels. To this end, more signal Monte-Carlo samples were needed to compare with data. When comparing expected signal to data and other MC one needs to normalise the signal MC events simulated above by the factor,

$$f = \frac{\mathcal{L} \times \sigma}{N} \tag{4.3}$$

where $\mathcal{L}$ is the data Luminosity, σ is the process cross section and N is the number of events generated in the Monte-Carlo simulation. Hence it is necessary to take a SUSY mass spectrum for each sample and calculate a cross section. Prospino[50] is a Fortran package for calculating Leading Order (LO) and Next to Leading Order (NLO) cross sections for a large number of output states. These cross sections are calculated from the partonic cross section as shown in Equation 2.15. Prospino can be set to run for various models but is mainly dependent on the mass spectrum of supersymmetric particles. When calculating the cross section, one needs to choose the factorisation/re-normalisation scale Q^2 of the theory. It is convention to choose this value as the average of the masses of the sparticles produced in the hard interaction. To account for any effect from this choice, one would wish to quantify the effects of the choice of this scale on the resulting values. To this end, one calculates the re-normalisation uncertainty. Simply, the chosen Q^2 is varied by 50% and the cross section is recalculated for these extrema. In this sense it is a pseudo-uncertainty, an estimate for the effects of this unknown quantity which is an accepted convention. The Prospino package has the ability to include these values in its output and it is important to include these values.

Additionally, one must consider the impact of the Parton Distribution Function (PDF) set one uses when calculating cross sections. Equation 2.15 shows the use of PDFs in calculating the partonic cross section. Again, two extremes are calculating by adding/subtracting the errors in individual PDF and the differences between them to the nominal value. The routine is then run for each variation to ascertain the effect of this change on the values. The author was tasked with providing the cross section values and associated errors for a number of analyses[51, 52, 53, 54, 55, 56, 57, 58, 59, 60, 61, 62]. For each mass configuration, a Les Houches Accord[63] formatted particle mass hierarchy must be fed into the prospino package. A decay process and options must be set and the cross section calculated. For each process and mass hierarchy the Fortran code must be altered, requiring a large manual effort. The author developed a framework for automating this process, reading the Les Houches Accord on the fly and altering the necessary details without manual input. In the course of this work, it was seen that the prospino package was running slowly and producing large volumes of error messages at LHC collision energies. After intensive investigation, a long–standing bug in the Prospino code was noticed, namely the variation of Q^2 scale was erroneously set to twice the suggested value. This took the scale above the 1 TeV limit of functionality. In conjunction with the authors of the package this bug was fixed and the author produced a large number of signal samples for analyses within the SUSY group.
In late 2011 the NLL–Fast routine became available for general use. NLL–Fast uses interpolation algorithms to produce cross section values. As well as incorporating Prospino results, grid files of NLO calculations and next to leading log re-summations of soft gluon emission are inputted into the interpolation grids. The routine provides a larger range of available cross section as well as greatly speeding up the calculation process. In early 2012 the ATLAS SUSY group switched to this methodology and a central file of relevant cross sections for the third generation squark searches was produced. Figure 4.3 shows these cross section values and associated errors plotted in the stop mass plane.

4.4 Search for Low Mass Stop Pair Production

A key group of ATLAS SUSY searches involve R-Parity conserving models with a LSP, where a b–quark jet is present such as that portrayed in Figure 4.4. Due to the typical mass spectra containing heavy gluinos and light third generation quarks, one expects decays chains from direct gluino and sbottom/stop pair production to dominate. These decays chains have large content of b quark jets in the detector. The b quark has a long

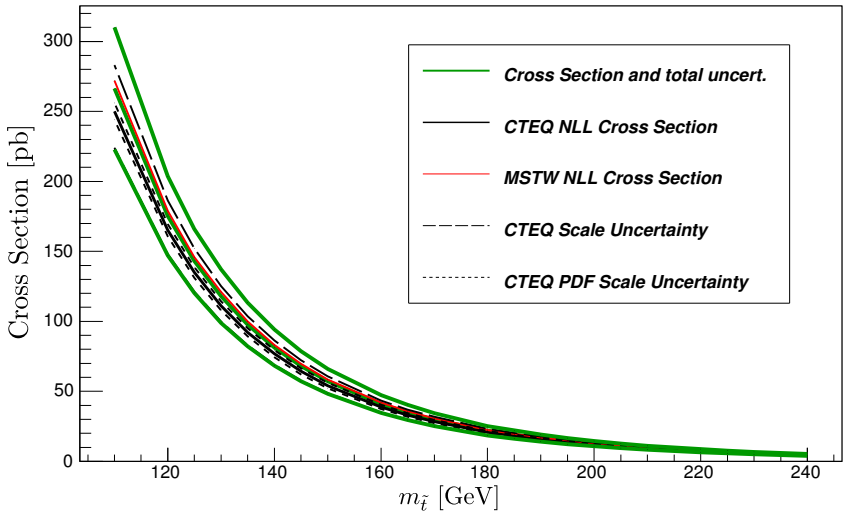

Figure 4.3: Cross sections for stop pair production calculated using the Next to Leading Log Fast (NLL–Fast) routine for this thesis. This result is an average of calculations inputting differing PDF sets, illustrated by the central black CTEQ line and the red MSTW line. The total error uncertainty, enveloped by two green lines is constituted of PDF, scale and α_s contributions. The first two of these uncertainties are plotted with dashed lines.

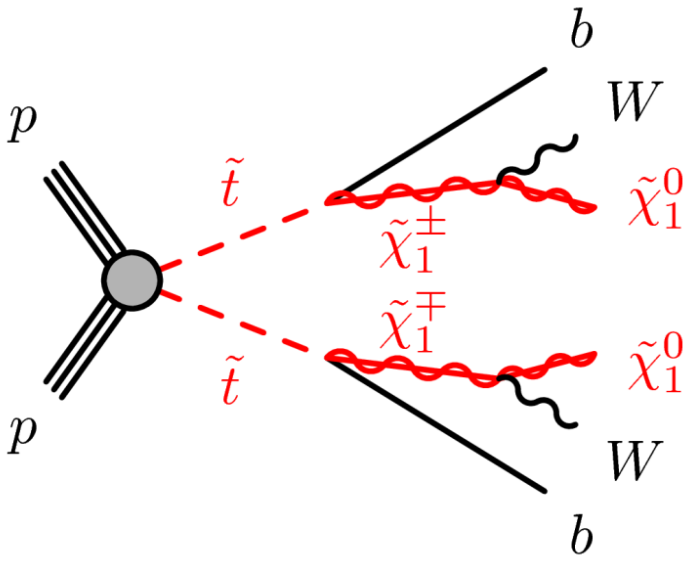

Figure 4.4: Stop pair production with 100% decay BR to b quarks and charginos. Charginos subsequently decay to neutralinos and W bosons.

lived state due to having a larger mass. Hence, the primary and secondary vertices are sufficiently displaced that with high enough detector resolution one can identify this displacement. Many background processes such as QCD, contain light flavour jets which will not pass a b jet requirement. This offers a method of signal isolation requiring lower jet or missing energy cut-offs. Specifically for this student, stop pair production where the LSP is produced via chargino decay for each stop

$$m(t) > m\left(\tilde{t}_1\right), m\left(\tilde{\chi}_1^{\pm}\right) < m(t) - m(b)$$

and

$$\tilde{t}_1 \rightarrow \tilde{\chi}_1^{\pm} b \rightarrow W^{(*)} \tilde{\chi}_1^0 b\,. \tag{4.4}$$

In this scenario the masses of the top and the lightest stop are almost degenerate. Top particles exclusively decay into a W boson and b quark, providing E_{T}^m via the neutrinos in leptonic decays. These decays behave very similarly in the detector to the stop decays containing one or two leptons (referring to only electron and muons), b and/or other jets, and large E_{T}^m from neutrinos and the neutralinos. In light of the large exclusion values of other production mechanisms, stop quarks were one of the most viable candidates for SUSY below the TeV scale. In the 2011 analysis the lowest p_T single lepton triggers that record all available events are used. Electrons with $\mathrm{p}_T > 25\,\mathrm{GeV}$ triggered with 97% efficiency and muons with $p_T > 20\,\mathrm{GeV}$ trigger with 90% & 75% efficiency for endcaps and barrel regions respectively. For the offline analysis, physics objects must meet quality and identification criteria uniform definitions across the experiment [64], called *loose*, *medium* and *tight*. Muons are required to pass the *medium* requirements, have $p_T > 10\,\mathrm{GeV}$ and $|\eta| < 2.4$, as well the isolation requirement that in a cone of $\Delta R = 0.2$ around the muon contain a p_T sum of less than 1.8 GeV. Finally, for cosmic ray rejection, muons must have a distance of closest approach or transverse impact parameter to the primary vertex of less than 1 & 0.2 mm respectively. Electrons are required to pass *tight* requirements [65] as well as $p_T > 20\,\mathrm{GeV}$ and $|\eta| < 2.47$, have the p_T sum of a $\Delta R = 0.2$ cone contain less than 10% of the electron's p_T. Jets are reconstructed using the anti-k_t algorithm [66], using a cone size of $R = 0.4$, with $\mathrm{p}_T > 20\,\mathrm{GeV}$ and $|\eta| < 4.5$. Any jet candidate within $\Delta R = 0.2$ of an electron is not stored and consequently any lepton within $\Delta R = 0.4$ of any surviving jet is also discarded.

The main discriminant used in this analysis is the mass scale subsystem variable [67]. One wishes to isolate a subsystem of particles (visible or otherwise) originating from the vertex of interest, referred to as downstream. Remaining underlying event or initial state

radiation particles are labelled upstream. Using these distinctions, a minimum of $\sqrt{s}$ can be calculated,

$$\sqrt{s}^{(\mathrm{sub})}_{\mathrm{min}}(\not{M}) = \left[\left(\sqrt{M^2_{\mathrm{sub}} + P^2_{T(\mathrm{sub})}} + \sqrt{\not{M}^2 + \not{P}^2_T}\right)^2 - \left(\overrightarrow{P}_{T(\mathrm{sub})} + \overrightarrow{\not{P}_T}\right)^2\right]^{1/2} \tag{4.5}$$

where $P_{T(\mathrm{sub})}$ and M_{sub} are the transverse momentum and invariant mass of the downstream visible particles. The invisible particles' invariant mass and transverse momentum, $\not{M}$ and $\not{P}_T$ are also used, with the latter identified as the global variable E^m_{T}. To correct for upstream particles affecting the transverse kinematic variable, the square of the vector sum of transverse momentum of upstream and downstream p_T is subtracted in the final term of Equation 4.5. This variable can be used to reconstruct $t\bar{t}$ events, where the invisible particles are neutrinos with $\not{M} = 0$. The subsystem variable for real $t\bar{t}$ events should peak around twice the top mass, as shown in Figure 4.6. Whereas stop pair events, due to the heavy neutralinos contained, show more events in the lower tail of the distribution $\sqrt{s}^{(\mathrm{sub})}_{\mathrm{min}}$. The analysis is split into two streams, 1 and 2 leptons, with tailored event selections for both. Specifically here the focus will be on the 2 lepton search. Here one expects two leptons, two neutrinos and two b–tagged jets. b jets are tagged using the JetCombNN neural network tagging algorithm[68] with weight > 1.8 cut–off. JetCombNN (also known as JetFitter) assumes b and c hadron decay vertices are in line with the b-hadron flight path. A Kalman filter can seek to find the PV from this assumption and calculate a b-hadron decay length. JetCombNN adds this information to the secondary vertex length used by other b–tagging algorithms with a neural network. In $t\bar{t}$ events it has been seen to tag 60% of b jets with a 10% rate of false positives [69]. With this in mind, events are selected with:

- Two oppositely charge leptons with one electron/muon of $\mathrm{p}_T > 20/25\,\mathrm{GeV}$
- Two jets, including one b–tagged jet
- $E^m_{\mathrm{T}} > 40\,\mathrm{GeV}$ and the invariant mass of the two leptons must fall between 30 and 81 GeV
- $\sqrt{s}^{(\mathrm{sub})}_{\mathrm{min}} < 225\,\mathrm{GeV}$ in Signal Region 1 (SR1) as shown in figure 4.5
- Or for Signal Region 2 (SR2) invariant mass of the two leptons and two jets $m_{lljj} < 140\,\mathrm{GeV}$ and $\sqrt{s}^{(\mathrm{sub})}_{\mathrm{min}} < 235\,\mathrm{GeV}$

Full sets of MC simulation are produced for each background as well as the signal grids, more information about the generators used can be found in [56]. Generator level MC is fed into the GEANT4 detector simulation[70] of the ATLAS experimental setup[71].

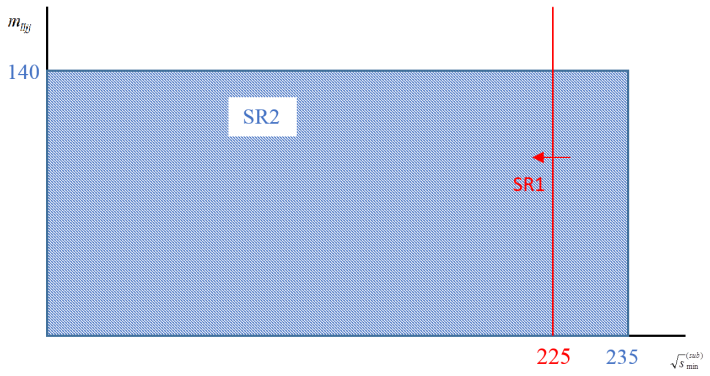

Figure 4.5: Diagram showing the two signal regions used in the analysis, portrayed on the m_{lljj} and $\sqrt{s}_{\min}^{(\mathrm{sub})}$ plane.

Stop production itself is simulated using PYTHIA6 and Herwig++[72]. These signal MC are scaled with cross section produced using NLL–Fast, see Section 4.3.
A number of potential backgrounds can be collectively labelled as fake lepton, where one or more object is incorrectly identified as a lepton. QCD events with many jets can fake both leptons, whereas W+jet events and single top events can both produce one real and one fake lepton. These backgrounds can not be effectively modelled using MC, so a data driven approach is essential. The so called Matrix Method is used in this instance. Leptons that are accepted into the final analysis all pass the *tight* requirements. By comparing the proportion of events passing *tight* and just the *loose* (less isolated) requirements, it is possible to estimate a probability of a lepton being faked. It is seen that there is negligible contribution from events with two fake leptons, but a measurable contribution from events with one fake and one real lepton. The major background in the 2 lepton channel is $t\bar{t}$ production. A control region for $t\bar{t}$ is defined by $m_{ll} > 101\,\mathrm{GeV}$ and $\sqrt{s}_{\min}^{(\mathrm{sub})} < 325\,\mathrm{GeV}$. These requirements select a $t\bar{t}$ rich sample with kinematics comparable to the signal regions. A number of fake events in the signal region can de defined as,

$$N_{SR}^{Top} = \left(\frac{N_{SR}}{N_{CR}}\right)_{MC}^{Top} [N_{CR}^{data} - N_{CR}^{non-top,MC} - N_{CR}^{fake}] \tag{4.6}$$

with a transfer factor between the control and signal regions,

$$TF_{MC}^{Top} = \left(\frac{N_{SR}}{N_{CR}}\right)_{MC}^{Top} \tag{4.7}$$

including the fake lepton background from the matrix method. Theoretical uncertainties prevalent in $t\bar{t}$ simulation are common in both regions and hence undergo cancellation,

providing more stringent estimates of the $t\bar{t}$ contribution than a purely simulation based approach. The effects of Z background are estimated by a control region with same flavour leptons, having $81\,\text{GeV} < m_{ll} < 101\,\text{GeV}$ and $\sqrt{s}_{\text{min}}^{(\text{sub})} < 225\,\text{GeV}$. In this region $t\bar{t}$ contribution is very reduced so that Z and Z+jets backgrounds can be isolated and measured. A transfer factor is calculated in a similar method to the $t\bar{t}$ estimate above. Small contributions from diboson and $t\bar{t}$ + X affect the channel are simulated using purely MC. The student was particularly involved in estimating the fake rates in the Top and Z control regions and applying this to the estimations, as seen in [73]. In using a data driven method, it is implicitly assumed that the simulation in the signal region contains non of the fake events. However, while one expects fake leptons to be badly modeled, simulations will contain some of the contribution. The student identified that the MC simulation did indeed contain these fake events (however at erroneous rates and with inaccurate kinematics). It is important that the fake events are not double counted. To prevent this the following process is followed for each lepton:

- Check if the lepton matches to a truth lepton in MC, if not label 'no match'
- If the lepton is true, check if the lepton parent was a W, Z, t or b quark
- Iterate the above step over the parents
- If no particle in the family matches W, Z, t or b, label as 'orphan'
- Label 'No Match' or 'orphan' leptons are *non–real* and others as *real*

Events are required to contain two *real* leptons. Events without two *real* leptons are removed from the MC and this modified simulation is fed into the analysis. This procedure proved very effective, retaining 98% of true *real,real* lepton events. In the W+jets MC sample, all events were removed by this procedure, such that the contribution is contained in the data driven fake Lepton numbers completely. This is a reassuring result, as (high p_T) two lepton events can only be produced from W+jets with one lepton being a misidentified jet. As shown by table 4.2, no significant excess was seen in either signal region. Using the CL_s method[74], 95% confidence levels upper limits are used to constrain MSSM models. These limits can be interpreted as upper bounds on the visible non-SM cross section $\sigma_{\text{vis}} = \sigma\epsilon\mathcal{A}$, with ϵ the sum of detector reconstruction efficiencies, $\mathcal{A}$ being the particle level acceptance and σ the production cross section for the signal. In these exclusions, the branching ratio of the stop is assumed to be 100%, with $\tilde{\chi}_1^\pm \rightarrow \tilde{\chi}_1^0 l^\pm \nu$ mimicking the SM branching ratio of 11%. Four pMSSM grids were created for exclusion. One grid in the $m_{\tilde{\chi}_1^\pm}, m_{\tilde{\chi}_1^0}$ plane with stop mass set to 180 GeV. Three grids in the $m_{\tilde{t}_1}, m_{\tilde{\chi}_1^0}$ plane, with $m_{\tilde{\chi}_1^0}$ set at 1 GeV, 180 GeV and half $m_{\tilde{\chi}_1^0}$

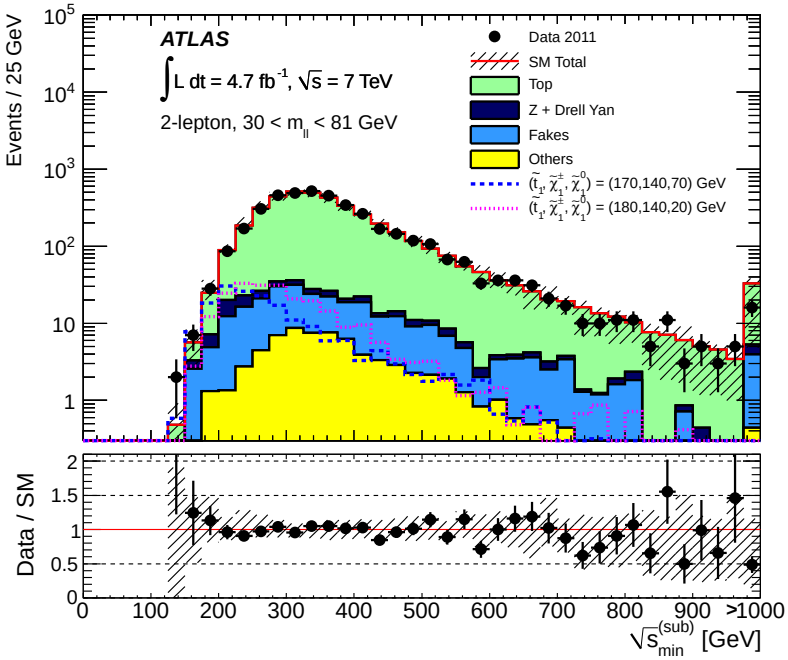

(a) $\sqrt{s}_{\text{min}}^{(\text{sub})}$ data distribution in [56] before the SR cuts, with normalised backgrounds and their total uncertainty as a hatched region. Two example signal models are superimposed on top with dashed lines.

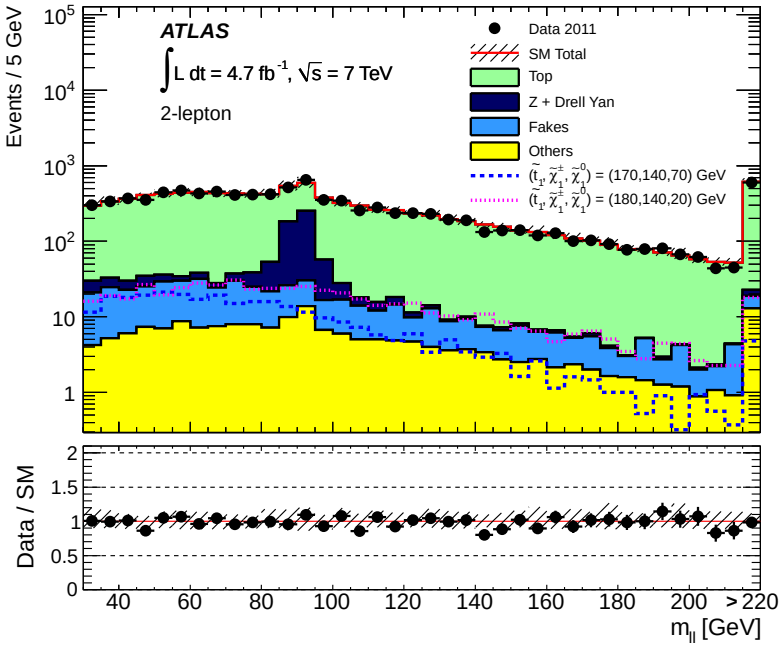

(b) Invariant mass of the two identified leptons as plotted in [56] before the SR cuts, with normalised top from the CR. The Z has not been normalised from the Z control region. The total uncertainty of background samples is shown as a hatched region. Two example signal models are superimposed on top with dashed lines.

Figure 4.6

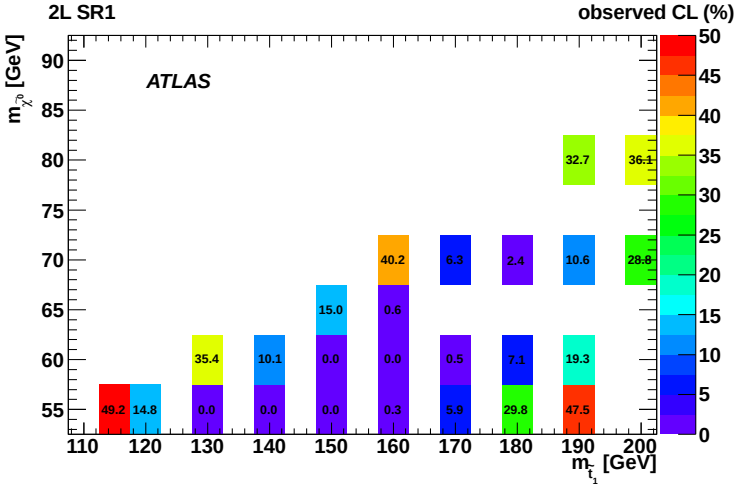

(a) Percentage Confidence Level values for SR1 in the signal scenario where the chargino has exactly twice the neutralino mass. For clarity of viewing, regions with $> 50\%$ are not drawn. This represents a visualisation of the mathematical process used to exclude regions of parameter space. The signal + background hypothesis is tested against data in each 2D bin, with a confidence value calculated. Signal regions are denoted excluded when showing a CL value of less than 5%, showing clear disagreement with a signal contribution.

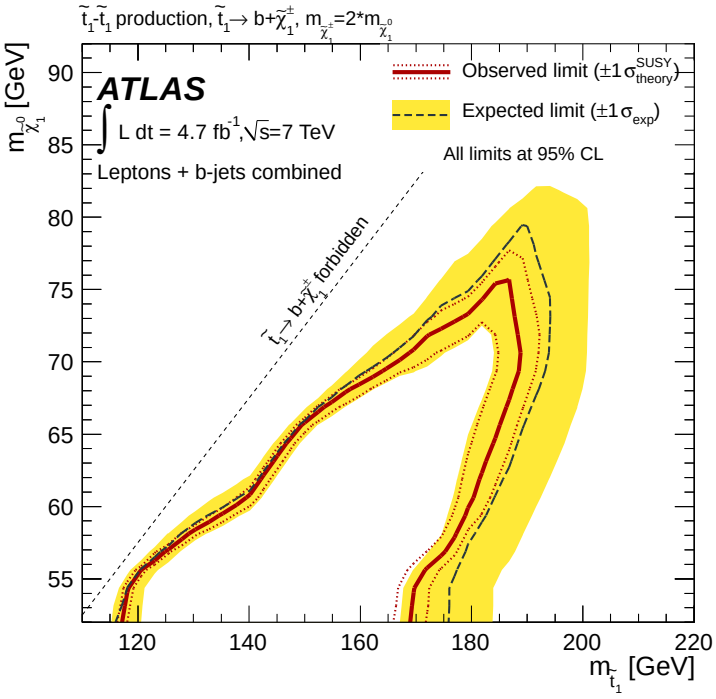

(b) Exclusion plane in the signal scenario where the chargino has exactly twice the neutralino mass. After the values in the above diagram are calculated, the limits of exclusion are plotted here. Observed limit is represented by the area contained by the solid red line and the x axis. The Expected exclusion limits follow a similar pattern in a dashed line. The yellow band represents one standard deviation from the central result.

Figure 4.7

Process	Number of SR1 Events	Number of SR2 Events
Top	$89 \pm 6 \pm 10$	$36 \pm 2 \pm 5$
Z+jets	$11 \pm 4 \pm 3$	$3 \pm 1 \pm 1$
Fake Leptons	$12 \pm 5 \pm 11$	$6 \pm 4 \pm 4$
Others	$2.7 \pm 0.9 \pm 0.7$	$0.9 \pm 0.2 \pm 0.5$
Total SM	$115 \pm 8 \pm 15$	$46 \pm 4 \pm 7$
Data	123	47

Table 4.2: Prediction for number of events in the 2011 two Lepton signal regions. Fake Leptons includes the numbers for W+jets. Numbers reproduced from ATLAS paper in Phys. Lett. B [56].

respectively. Figure 4.7 shows an example exclusion for the final grid and the respective confidence level plot. After the 7 TeV analysis was completed, work progressed onto the 8 TeV dataset, which the student was not involved with. With the results from the above analysis recorded, priorities shifted for the new analysis. The new analysis focused on using the m_{T2} stranverse mass variable to identify semi-invisible decays. With increased centre of mass energy and luminosity, further exclusion was possible as seen in [59] and work will continue into the future 13 & 14 TeV runs in 2015 onwards.

Chapter 5

Measurement of WW events using the LHCb experiment

Section 2.5 outlines the motivations and challenges of a WW diboson measurement. Diboson physics can provide stringent tests of the SM, aTGC can hint at or exclude new physics phenomena and dibosons at LHCb could be used to measure the low Björken–x PDF content of the proton. This chapter outlines the ideas, method and undertaking of such an analysis on the LHCb experiment. WW events produced in LHC collisions will produce isolated opposite sign leptons with large transverse mass. The leptons will also have a low impact parameter due to the almost instantaneous W decays. Events in the forward angular acceptance of the LHCb will have large longitudinal momentum with respect to the beam pipe. Using a selection of these kinematic variables WW signal, as visualised in Figure 5.1 can be distinguished from the background events. In the general purpose detectors there are enough statistics to study all the decay ratios, with results being in agreement with the SM and no aTGC effects have been seen[23, 24, 25]. The ZZ measurements look for two pairs of high p_T leptons, each with transverse mass around the on–shell Z mass. WZ decays are complicated by their low leptonic BR and a large background contribution from events with leptonic τ decays. WW events use E_{T}^{m} and m_T (see Section 4.2) to identify neutrino signatures.
In the jet rich environments of ATLAS and CMS, large numbers of jets can be reconstructed as fake leptons. This can be a consequence of not detecting all the particles in the jet, lapses in reconstuction algorithm or having a jet dominated by a high p_T leption. These GPD measurements require strict jet vetoes, using the ΔR cone variable around physics objects. Cross sections in these analyses are presented in a fiducial region, as well as total cross section. Presenting a cross section in a stated p_T, angular or other

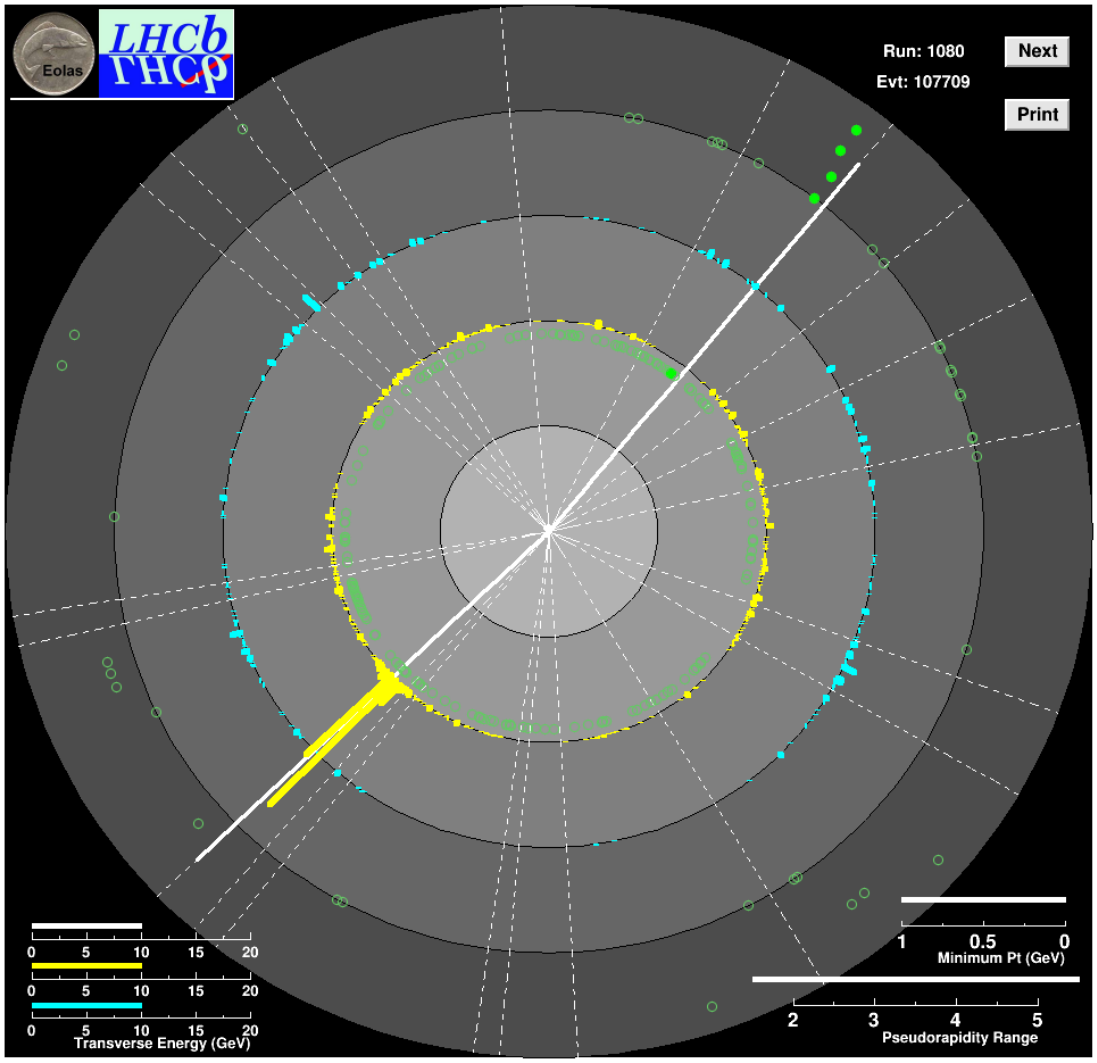

Figure 5.1: A WW simulated event display using the Eolas viewer. The centre of the display represents the LHCb collision point, with radial distance the z co–ordinate system. Each radial disk represents a detector component, with a representation of the basic reconstructed output. White dotted lines represent tracks, with solid white lines representing high p_T tracks. The ECAL (HCAL) deposits are represented in the third (fourth) layer with yellow(blue) bars, related to the amount of energy deposited. Finally hits in the muon layers are portrayed with green circles which are solidly filled if matching a track in reconstruction.

kinematic region has many advantages. The process of expanding an effective cross section measured in a small kinematic region to the full hadronic level cross section can introduce a large theoretical uncertainty. Instead, quoting partonic level uncertainties allows for the ease of tailoring theoretical prediction from various models/PDFs. The fiducial cross section is defined as,

$$\sigma_{fiducial} = \frac{N_{obs} - N_{bkg}}{C \int \mathcal{L} dt} \tag{5.1}$$

where N_{obs} & N_{bkg} refer to the observed number of events and the predicted number of background events, $\int \mathcal{L} dt$ is the integrated data luminosity and the acceptance factor C is defined as,

$$C = \frac{N_{Reco}}{N_{fid}} = \sum^{i} \epsilon_i \tag{5.2}$$

with N_{Reco} being the number of MC events passing full detector reconstruction and N_{fid} the number of MC truth events passing the fiducial requirements at generator level. The acceptance factor can also be calculated as a sum of efficiencies of reconstruction, ϵ_i. In cases where backgrounds are subtracted in the analysis, the cross section is modified,

$$\sigma_{fiducial} = \frac{N_{obs} - N_{bkg}}{C \int \mathcal{L} dt} \left(1 - \frac{N_{sb}^{MC}}{N_{sig}^{MC}}\right) \tag{5.3}$$

with N_{sb}^{MC} being the number of subtracted background MC events and N_{sig}^{MC} being the number signal MC events. This is used when a data driven estimate for a background is calculated (as opposed to pure simulation). These fiducial cross sections also benefit from cancellations in the same theoretical uncertainties in the acceptance factors and ratio of signal and background events.
In LHCb the angular acceptance of the diboson events is much lower than in a general purpose detector, so extrapolation of fiducial cross section to the total value can lead to a large uncertainty.

5.1 Background Processes

A number of background processes can produce the baseline signature of a muon and electron in the forward region. These include processes that are direct backgrounds,

Decay Mode	Total Cross Section (NLO)	# Events per fb^{-1} data
WW	57.3	53.4
WZ	4.48	22.9
ZZ	7.92	2.57

Table 5.1: Table of cross sections and number of events passing into the LHCb for diboson states. The leptons produced in the events must fall into the $2 < \eta < 4.5$ angular region and have a transverse momentum, $\text{p}_T > 15\,\text{GeV}$.

producing a muon and electron in the main leading order process. These backgrounds are reduced by using events requirements tailored to kinematic differences with the signal. Other background are not direct but can fake the signal pair of leptons. The production and characteristics of the MC that was simulated to study the backgrounds are described below.

5.1.1 Signal and Background Simulation

The contributions of these processes must be simulated in order to be accounted for in the final comparison with data. Initial events are simulated using PYTHIA8 and this is fed into the GAUSS framework. The cross section used for each process is recorded as well as the ratio of events initially produced and those recorded at the end of the process, allowing for events not surviving angular or basic kinematic requirements. These events are further fed into the LHCb detector simulation with recorded running conditions from the 2012 data taking. The following backgrounds have been produced centrally by the LHCb experiment for multiple analysis, with two exceptions. Diboson and $t\bar{t}$ samples, requiring two $\text{p}_T > 15\,\text{GeV}$ leptons are produced specifically for this analysis, using the same conditions as the central simulations. Effective NLO cross sections for these samples are produced using the POWHEG-BOX generator tool[75, 76, 77]. Two hundred and fifty thousand events of each diboson process are created, alongside two hundred thousand events of $t\bar{t}$. A simple python script is used to apply the PYTHIA/GAUSS generator level event requirements applied in the full simulation. These requirements are an opposite sign pair of generator level W bosons, decaying to electrons or muons, each with $\text{p}_T > 15\,\text{GeV}$ and $\theta < 400\,\text{mrad}$. A ratio A, of the number of surviving events to the number of events originally produced is calculated. The effective cross section of the

sample can then be calculated

$$\sigma_{\text{eff}} = A\sigma_{\text{tot}}BR, \tag{5.4}$$

where σ_{tot} is the total cross section for the process and BR is the branching ratio of the process to the leptonic state created.

PDF Uncertainty

The uncertainty introduced from the choice and variation in PDF set is needed for an appropriate use of simulation. Three PDF sets are used; MSTW[78], CT10[79] and NNPDF[80]. The first PDF set fixes a central value for $\alpha_s(m_Z)$ whereas the other two sets use the best value from their PDF fits. Two uncertainties are calculated for the PDF contribution. Firstly, the statistical errors on the simulated effective cross section are combined to form a MC sampling statistical uncertainty. Secondly, the difference between the highest and lowest individual values and the mean, in addition to the uncertainty on the individual PDF sets, are taken as the PDF uncertainty. Finally the uncertainty on the theoretical cross section used for normalisation must also be considered. The fiducial cross section of the signal MC is then given as

$$\sigma_{\text{fid}}(\sqrt{s} = 8\,\text{TeV}) = 53.4^{2.0}_{1.5}(\text{theo.}) \pm 0.2(\text{stat.})^{+3.0}_{-2.7}(\text{PDF.})\ \text{pb} \tag{5.5}$$

PDF Set	Events surviving %	# Events per fb^{-1} data
CT10	3.90	50.7
CT10nlo	3.98	51.8
MSTW2008lo68cl	4.20	54.7
NNPDF	4.23	56.4

Table 5.2: Table showing POWHEG output for WW simulation. For each PDF set, 250000 events were produced. Column two shows the ratio of events surviving generator p_T, acceptance and lepton cuts that are also applied to the full MC simulation. The final column represents an effective luminosity for the WW MC decaying to any combination of μ or e, calculated using Equation 5.4.

PDF Set	Events surviving %	# Events per fb^{-1} data
CT10	0.690	83.3
CT10nlo	0.650	78.7
MSTW2008lo68cl	0.696	83.8
MSTWQ2008lo68cl-nf3	0.666	80.8

Table 5.3: Table showing POWHEG output for $t\bar{t}$ simulation. For each PDF set, 250000 events were produced. Column two shows the ratio of events surviving generator p_T, acceptance and lepton cuts that are also applied to the full MC simulation. The final column represents an effective luminosity for the $t\bar{t}$ MC decaying to any combination of μ or e, calculated using Equation 5.4.

5.1.2 Top Pair Production Background

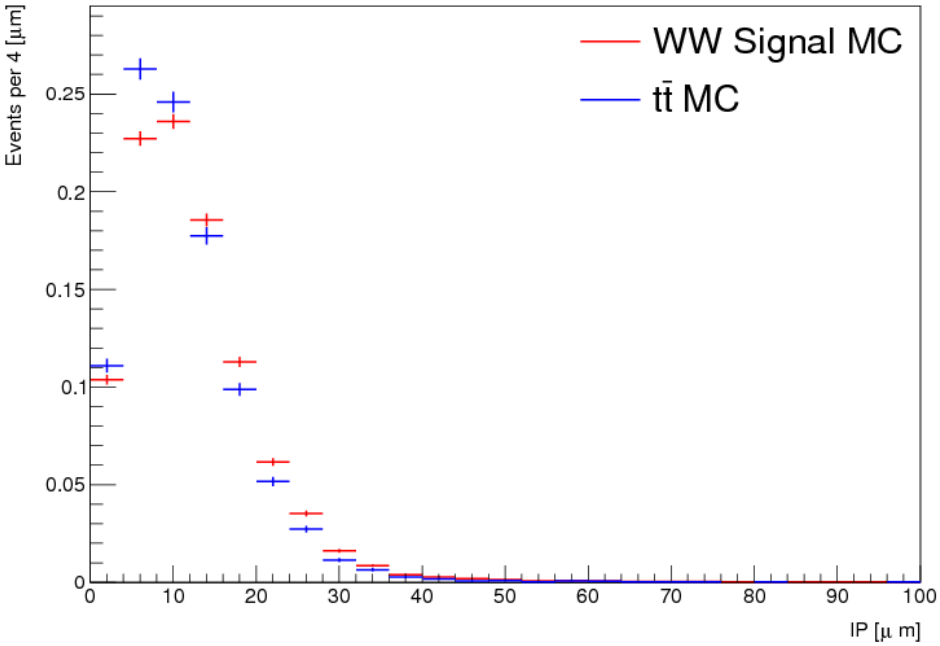

Figure 5.2: The shapes of Impact Parameter (as defined in 5.2.4) in electrons in the WW and $t\bar{t}$ simulation.

A top and anti-top quark pair can be produced through gluon and quark pair production. Production in the forward region is rare, as shown by table 5.3, but is still 50% larger than the WW rate. Top quarks decay almost exclusively to a Wb pair, with lifetimes of $O(10^{-24})s$. The width of the top means that the particle decays before hadronisation into quark–antiquark pairs can begin. The $t\bar{t}$ events produce isolated leptons from the same origin point. Hence, the electron–muon pairs formed having remarkably similar kinematic distributions to WW signal. The two step decay, provides

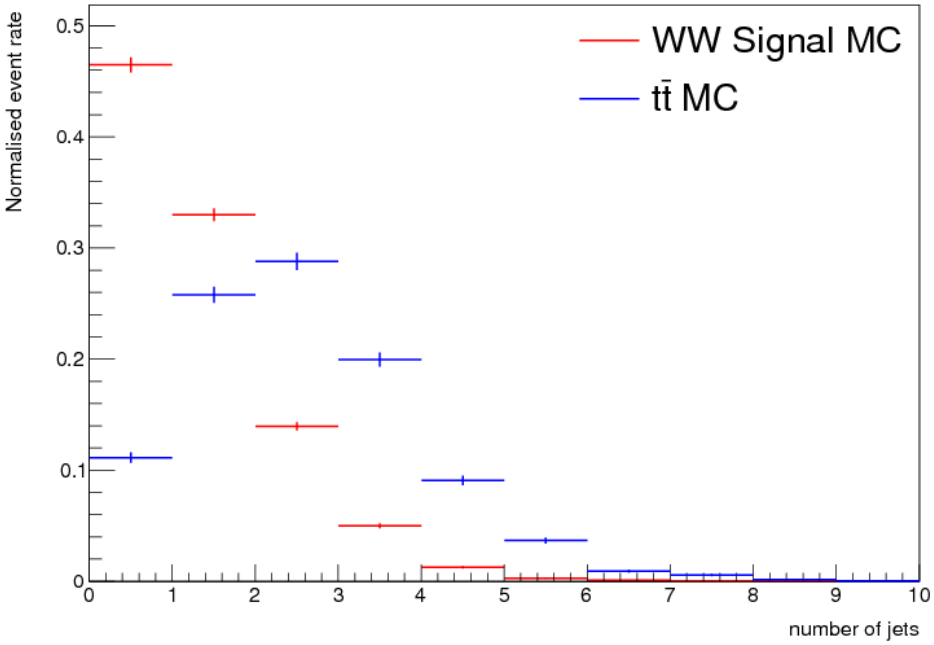

Figure 5.3: The number of jets in WW and $t\bar{t}$ simulations after the lepton quality invariant mass requirements. It can be clearly seen that the contribution from $t\bar{t}$ background can be considerably reduced by imposing a jet veto.

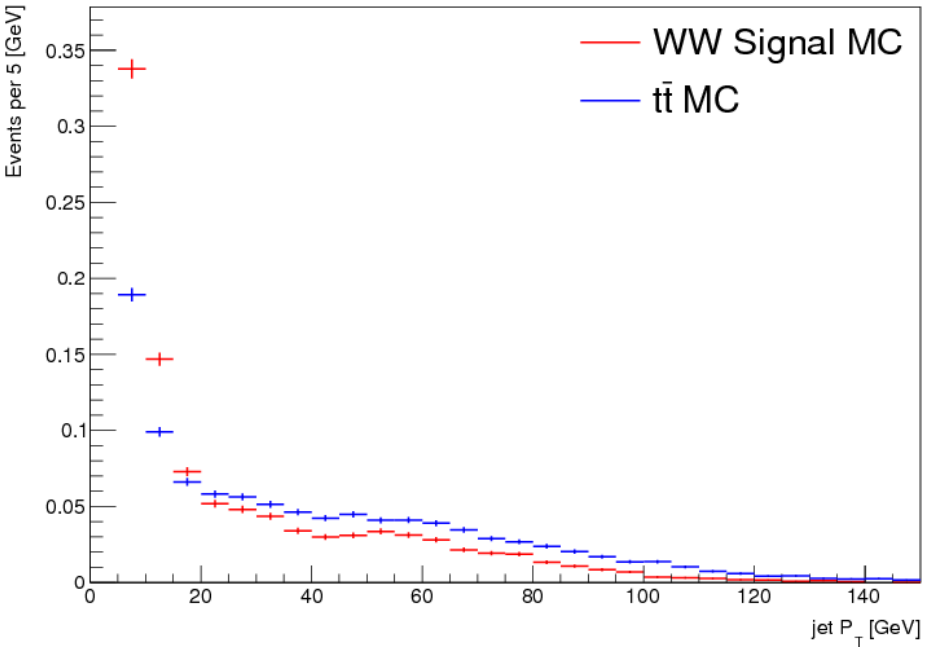

Figure 5.4: The p_T spectrum of jets in WW and $t\bar{t}$ simulations, with the latter having a larger tail in high p_T values.

an increase in separation between the two leptons, as seen in Figure 5.2, but the effect is too small to separate from signal. Since WW events do not produce a high p_T quark, a

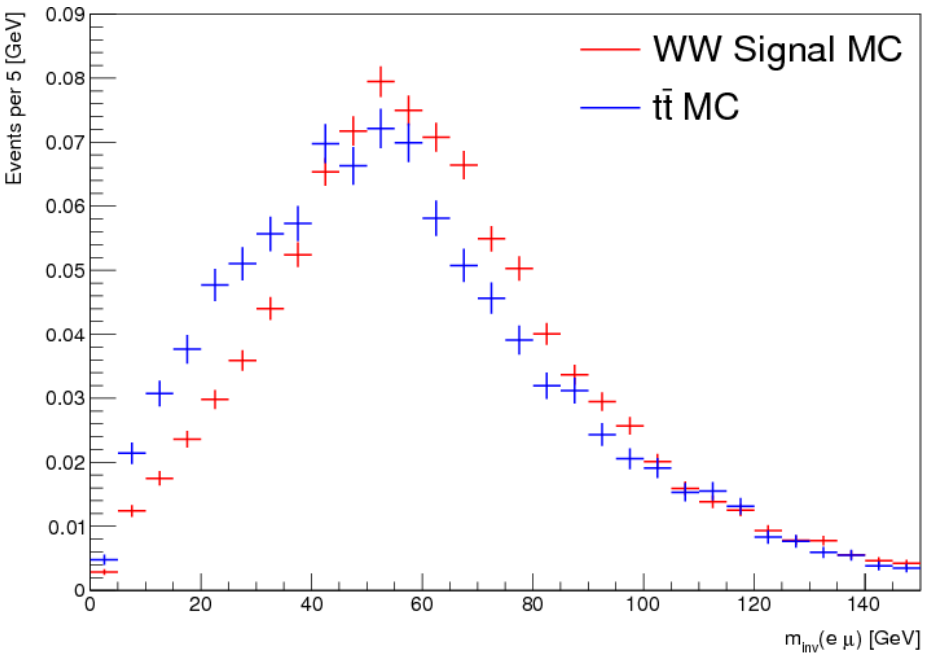

Figure 5.5: The normalised distribution of the invariant mass of the electron and muon in WW and $t\bar{t}$ simulation.

jet veto is an effective discriminant. Events where the quarks exist outside the acceptance or are not reconstructed can remain as background. Figure 5.3 shows $t\bar{t}$ events with higher jet multiplicities and fewer low p_T jets than in signal. It is clear here that a jet veto is a strong discriminant for the $t\bar{t}$ background that is otherwise very similar. Nearly ninety percent of $t\bar{t}$ events are removed, compared to roughly half the signal events. After the electron and muon quality refinements and invariant mass selection, 2.8 $t\bar{t}$ events are expected. A further 95% of events are removed with the zero jet requirement and the final selection leads to an expectation of less than a twentieth of an event.

5.1.3 Z Decaying to Taus Background

Z events in LHC collisions are common and will decay into a pair of tau leptons at a rate of 3%. τ leptons are unstable (due to their heavy mass) and decay to a variety of leptonic or hadronic modes. The dominant leptonic modes are $\tau \rightarrow \mu\bar{\nu}\nu$ and $\tau \rightarrow e\bar{\nu}\nu$. The branching ratio of a Z decaying into an electron and muon via two τ leptons is just over 4%. Z events produce isolated leptons and large values of transverse mass. Two neutrinos are produced in each leptonic tau decay, carrying invisible momentum. This results in softer leptons as shown in Figure 5.7, leading to 36% of muons and 67% of electrons failing baseline LHCb leptons p_T requirements. The τ decay also has a

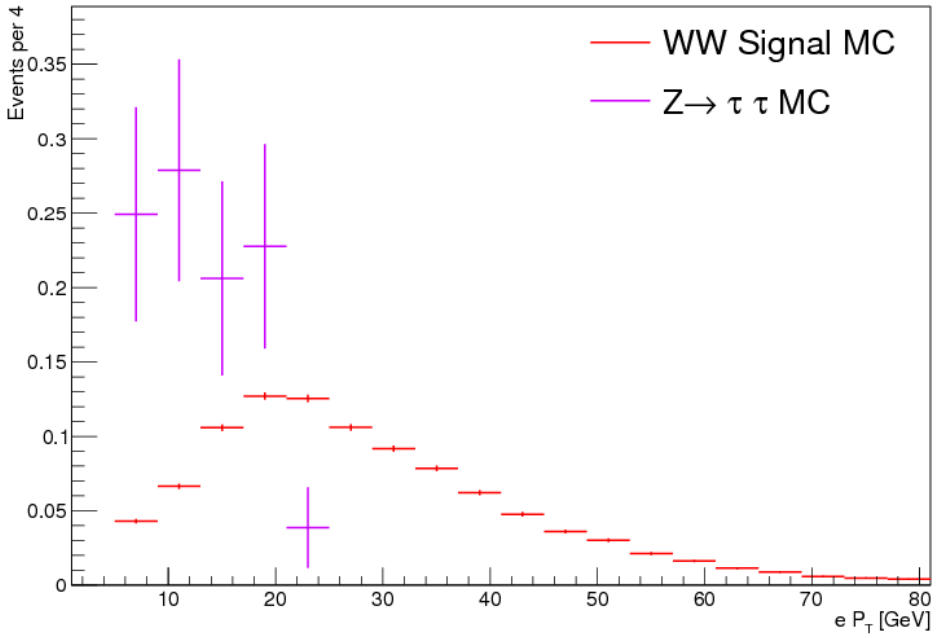

Figure 5.6: The shape of the electron p_T distributions in WW and $Z \to \tau\tau$ simulation. Due to the decay of τ containing invisible neutrinos, it has a high proportion of electrons with low p_T, that can be used to reduce this background.

visible lifetime, with decay lengths $O(1\text{cm})$. This visible lifetime can result in attributing different primary vertices for each lepton, where the stripping (see Section 5.2.3) requires the two leptons to share a primary vertex. Hence, many of these events failing to pass the stripping requirements for a lepton candidate pair and are not stored. The non–zero τ decay length also provides a larger impact parameter (see Section 5.2.4) with respect to the primary vertex than in other Z events, as seen in Figure 5.8. This also manifests with higher value of the impact parameter distance of closest approach (see Section 5.3.3). Figure 5.9 shows that requiring a low value of this variable can reduce the contribution of $Z \to \tau\tau$ to zero in the signal region. Roughly four million events are simulated in the LHCb acceptance, however events mimicking the initial stripping requirements on leptons contribute a very small proportion of events. The statistical uncertainty on this background is therfore high, as can be seen in the aforementioned figures. However due to small $Z \to \tau\tau$ rates, this does not contribute greatly to the overall uncertainty.

5.1.4 Indirect Two Lepton Backgrounds

A number of backgrounds do not contain both an electron and muon in the main leading order process, but full events can be reconstructed with both. This is compromised of

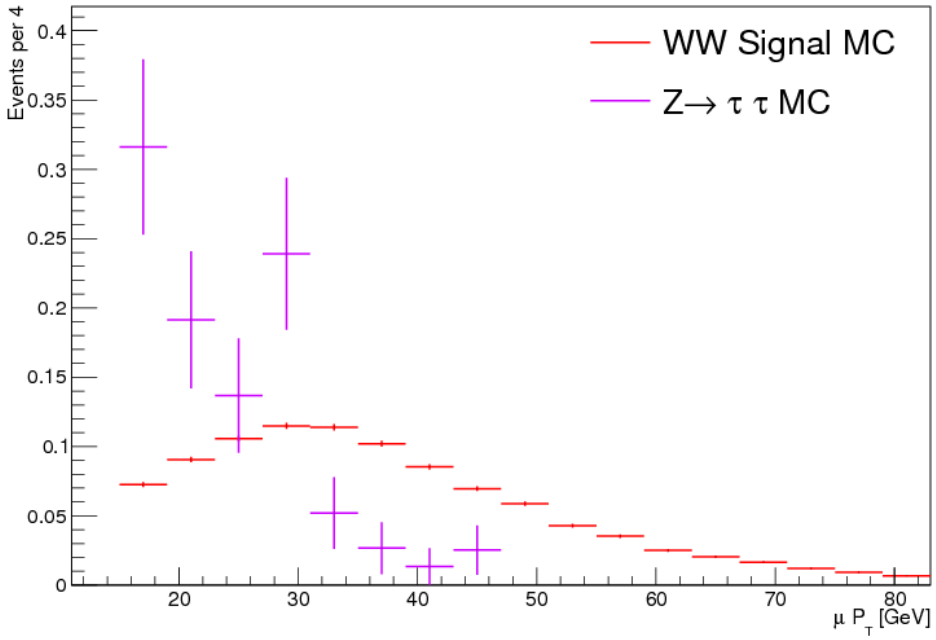

Figure 5.7: The shape of the muon p_T distribution in WW and $Z \to \tau\tau$ simulation. Due to the decay of τ containing invisible neutrinos, it has a high proportion of muons with low p_T, that can be used to reduce this background.

other physics objects faking leptons (usually electrons). The main backgrounds of this type are single top production and single W & Z production with an associated jet. Single top production contains one heavy b quark jet, which is often vetoed in the event and seldomly fakes an isolated electron. One would naively expect the second fake lepton to be less isolated and/or have a large impact parameter, allowing for removal of this background with lepton quality cuts. For this simple approach, one relies on having well simulated jets in the forward region. However, as seen in the LHCb $t\bar{t}$ analysis [81] there are deficiencies in the simulation of forward jets. Reconstruction of MC simulating $Z \to \mu^+\mu^-$ and $W \to \mu + \nu_\mu$ events that must contain a jet, suggest a fake event rate greater than the combined data rate after stripping requirements. Figure 5.11 shows broad agreement[1] in the muon p_T, but this is not the case in electrons shown in Figure 5.10. These electrons inside jets are not truly isolated, other particles created in the hadronisation will be present in the reconstructed jet cone as described in Section 5.3.2. The summation of these particles' energy in the cone should prompt reconstruction of a jet. However, if these particles are not modelled with satisfactory detail in MC, no such jet will be identified. This will lead to a greater rate of fake electrons in MC than in the

[1]Difference in shape can be attributed to the comparison between leptons from W decays to those of W and Z decays radiating a jet.

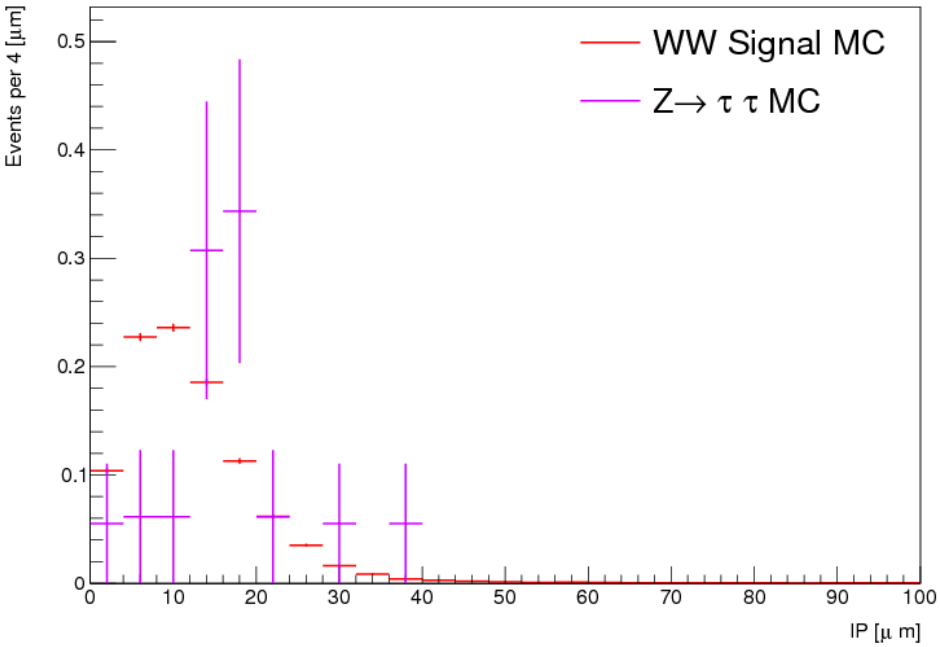

Figure 5.8: The shape of the electron impact parameter (see Section 5.2.4) distribution in WW and $Z \rightarrow \tau\tau$ simulation. Electrons that are the product of τ decay will not be centred on the event primary vertex.

data.

In GPD diboson searches the rate of jets faking leptons is estimated using a fully data driven approach, similar to the method detailed for the SUSY search in Section 4.4. The matrix method is used to define four regions of data. Firstly, an analysis cut is inverted to form a control region. Secondly, for both of these regions the lepton isolation requirements are loosened to form two more regions. A transfer rate between the two inverted regions is calculated and applied into the signal region from the loose signal region. However, due to the low event statistics in the signal channel this is not possible[2]. Instead a semi-data driven approach in a higher rate channel is useful. The relative rate of jets faking electrons can be isolated by selecting muon pairs in Data and $Z \rightarrow \mu^+\mu^-$ MC[3]. After selecting dimuon events with high p_T muons within 30 GeV of the Z mass, electrons in the event are also stored. The rate of events containing electrons passing the

[2]Five million $Z \rightarrow \mu^+\mu^-$ +jets made are simulated in the LHCb acceptance, with roughly seven thousand unscaled events surviving stripping and only 32 after final selection.

[3]This is inclusive MC where there is no requirement for a jet. The MC scaled in the final analysis is requires a jet in the partonic production stage. The inclusive MC is used in order to avoid any potential bias.

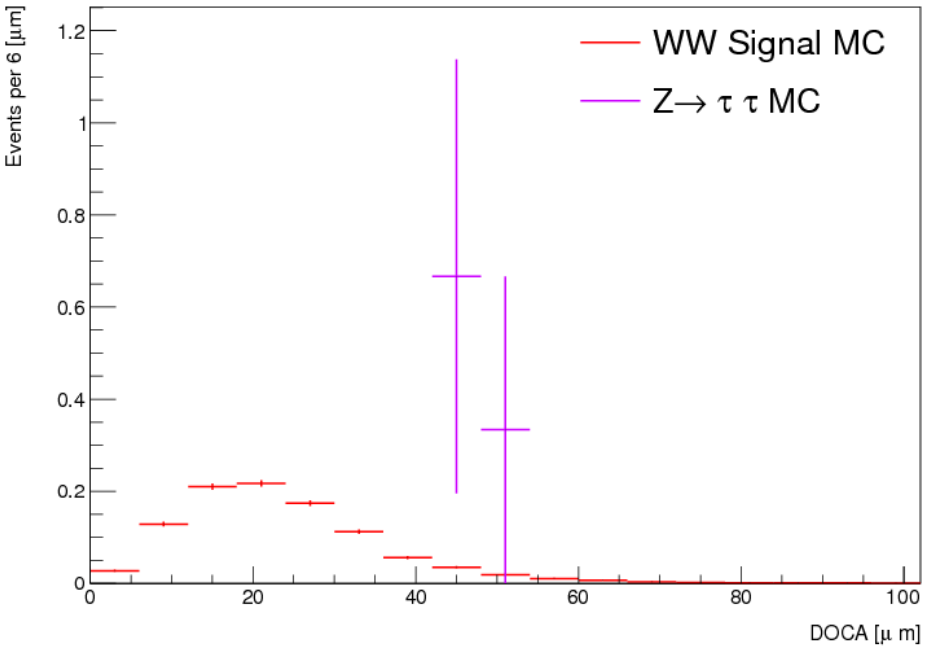

Figure 5.9: The shape of the distance of closest approach for the muon and electron in WW and $\tau\tau$ simulation. The initial vertex in the latter produces two τ leptons that travel O(cm) before decay into lighter leptons. Hence, the decay products originate from physically separate vertices, resulting in higher values of this variable.

standard quality requirements is measured to form the ratio,

$$\frac{(N_{\mu\mu}/NN_{\mu\mu+e})_{\mathrm{MC}}}{(N_{\mu\mu}/NN_{\mu\mu+e})_{\mathrm{DATA}}} = 0.18 \tag{5.6}$$

denoting the differing rate of fake electrons in MC and data. Z events are produced at high rates, with a pure clean sample. One only expects electrons from radiated jets in the events, hence it provides an effective correction factor, utilising high statistical rates. This result shows that the forward jets are indeed poorly modelled in the forward region. As described in Section 3.2, the LHCb detector was primarily designed for the identification of composite hadrons such as B mesons and/or isolated leptons. Identification of high momentum electrons can be complicated by punch through, where electron energy deposits are not confined to the EM calorimeter. The simulated W and Z MC samples requiring final state radiation jets are therefore modified by the above ratio to account for these issues.

Figure 5.12 shows a large tail in the electron IP. These two characteristics are used in selecting good quality electrons as described in Section 5.2.4, aiding in vetoing fake backgrounds. There are additional jets in 86% of events, such that a jet veto can further alleviate these events. The discriminating variables listed in Section 5.3 reduce the

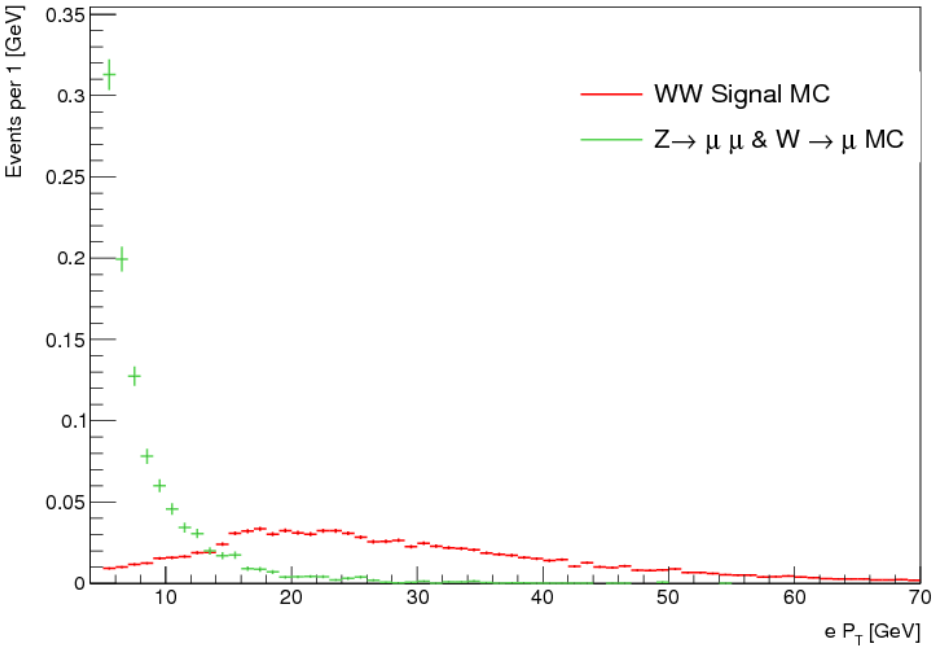

Figure 5.10: The shape of the electron p_T distributions in WW and single electroweak boson simulations. The single boson events do not contain a leading order electron, but an electron can be reconstructed from a ISR jet. These electrons are typically of low p_T.

estimated contribution of $Z \to \mu^+\mu^-$+jets and $W \to \mu$+jets to 0.41 and 0.2 respectively. $W \to e$ and $Z \to e^+e^-$ backgrounds contributions are estimated to be zero. These events are very rare, even with the high Z production rates. Consequently the unscaled number of MC events in the signal region is low, with a high statistical uncertainty on these estimates.

5.1.5 Unsimulated QCD and electroweak backgrounds

Some backgrounds are not readily simulated using a MC approach, such as QCD background. QCD events would typically have non–isolated leptons. These processes will produce leptons equally in both same and opposite sign lepton configurations. It is therefore possible to estimate the volume of these backgrounds by inverting the charge requirement of the candidate selection and processing the full dataset. Nearly two hundred events pass the stripping same sign lepton candidate pair selection. However, none of these same sign events contain any jet content and hence no events pass the full selection. The contribution of QCD events in the signal region is therefore also estimated to be zero.

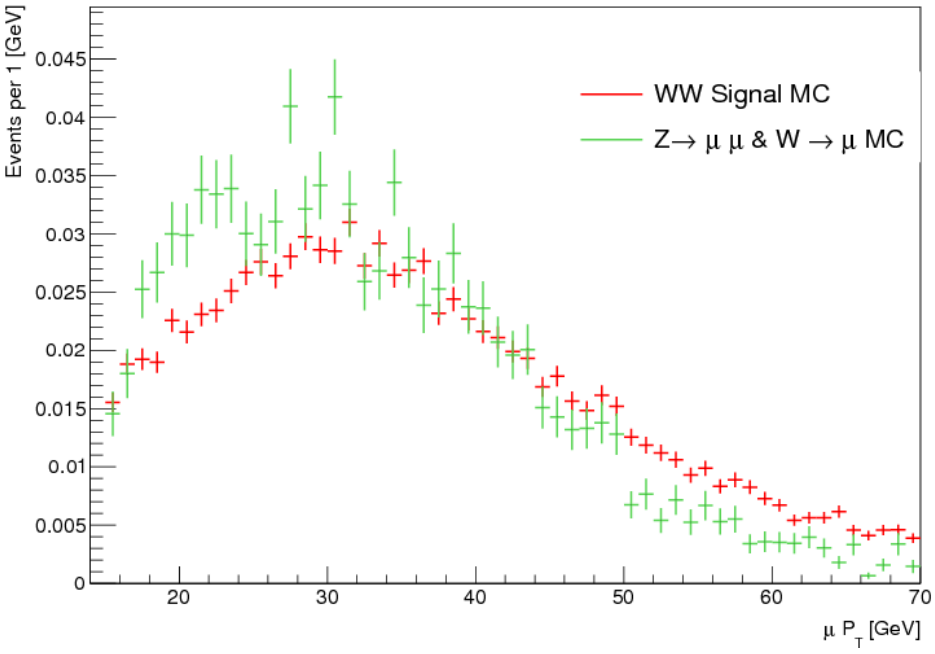

Figure 5.11: The shape of the muon p_T distributions in WW and single electroweak boson simulations. Both samples produce leading order muons decaying from an electroweak boson.

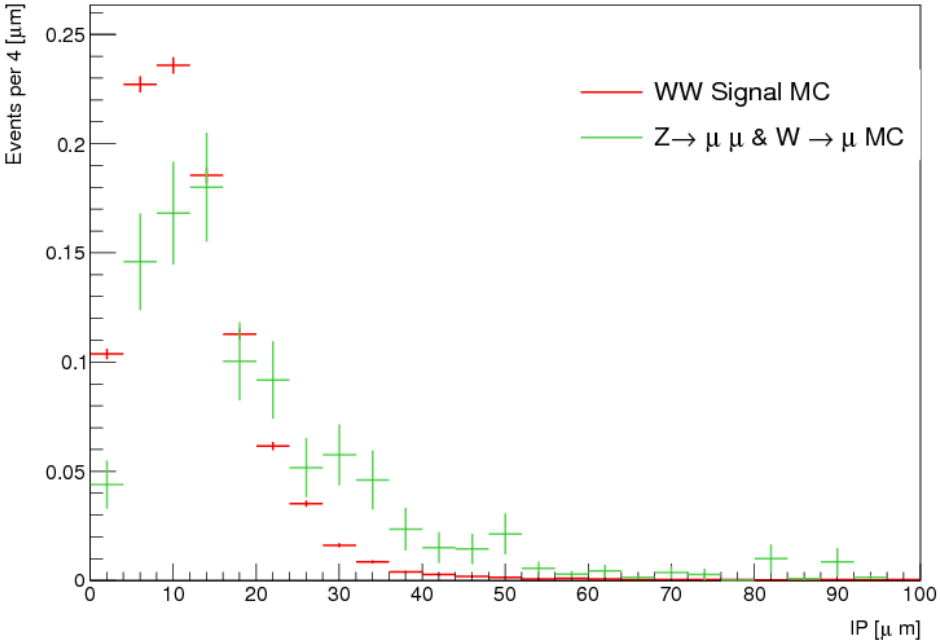

Figure 5.12: The shape of the electron impact parameter (see Section 5.2.4) distribution in WW and single electroweak boson simulations.

5.1.6 Higgs

Higgs bosons produced in the proton–proton collisions can decay into pairs of electroweak bosons. The Higgs is preferentially produced with large transverse momentum and as such the angular acceptance of these events in LHCb is very low. In addition to this, the Higgs cross section at 8 TeV is only 22.1 pb[82]. These two factors contribute to less than 0.15 events expected in the acceptance in the 2012 run. Taking into account reconstruction efficiency in the analysis selection this background can be treated as negligible.

5.2 Event Pre–selection

5.2.1 Trigger

As described in Section 3.2.6, undesired events are filtered from data (and MC) using the LHCb trigger system. In this analysis, the muon in the event is the object triggered on. Specifically the L0MuonDecision, Hlt1SingleHighPTMuon and Hlt2SingleHighPTMuon trigger are used. This trigger configuration requires a $p_T > 15\,\text{GeV}$ muon with < 600 SPD hits. The efficiency of the trigger selection is estimated with the tag and probe method, utilised in numerous LHCb analyses with muons[83, 84]. This method utilises the ability of the experiment to measure $Z \to \mu\mu$ decays to high precision. Data is processed to perform the basic identification of oppositely charged muons pairs, within a Z window. This window is defined here as the invariant mass of the two muons falling within 30 GeV of the Z mass. Two basic muons are selected with basic quality cuts[4]. One muon which passes the trigger selection with $p_T > 20\,\text{GeV}$, *ProbNNmu*> 0.68 and passes the ISMUON requirements. *ProbNNmu* is a neural network output for muon identification and the ISMUON flag is passed if the reconstructed muon track is close enough to hits in all the M1–M5 stations. The second muon is then known as a probe, a high p_T muon that the experiment should ideally trigger on. The rate at which these probe muons trigger can be identified as the muon identification efficiency. The systematic uncertainty on this efficiency can be calculated by comparing the efficiency in both $Z \to \mu\mu$ and signal MC. The efficiencies are shown in Figure 5.13, resulting in an efficiency, $\epsilon_{\text{trig}} = 0.765 \pm 0.023$. Similarly to the trigger efficiency, one must estimate

[4]Namely the same muon requirements in the main analysis, track χ^2, σ_P/p and angular acceptance. Additionally a small isolation requirement is put in place, $|\Delta\phi| > 0.1$.

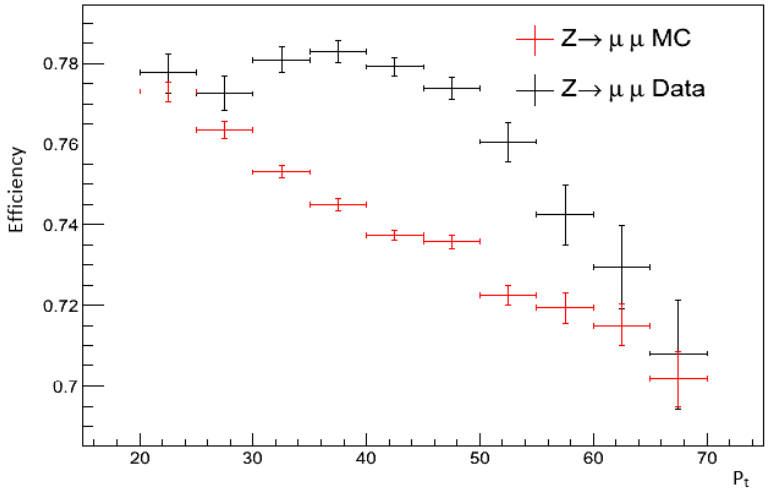

Figure 5.13: Efficiency of a probe muon activating the single muon trigger in $Z \to \mu\mu$ selected data and simulation. For events within 30 GeV of the Z invariant mass, a tag muon is selected that passes the muon trigger. The efficiency is then calculated from the proportion of events where the probe muon also passes the trigger. These secondary muons in Z events contain characteristics that should pass the trigger, so form a good test of the trigger performance. It can be seen that the MC overestimated trigger efficiency, partly due to lower muon chamber resolution and optimaisation of the detector to events with low energy muons, such as $B_S \to \mu^+\mu^-$ events.

the effect of the SPD cut ($N_{SPD} < 600$) in the W triggers. The dimuon trigger instead requires $N_{SPD} < 900$ and so the SPD cut can again can be measured using tag and probe. In this case, full dimuon trigger is placed on both muons with the tighter SPD requirement differentiating the tag and probe muons. The resulting efficiency is, $\epsilon_{\text{SPD}} = 0.828 \pm 0.025$.

5.2.2 Basic Physics Object Definitions

Tracks for particle identification are required to be in the range of $2 < |\eta| < 4.5$. Futhermore, the fit of the hits to the track must have a χ^2 probability of > 0.001. Muons are selected using the LHCb *tight* definition with the additional requirement ECAL detector deposits $E < 10\,\text{GeV}$. This extra requirement aides in purifying the muon sample against mis–identified electrons. Electrons are identified using the same procedure as the $Z \to e^+e^-$ analysis[85]. These requirements focus on the energy deposits of electron candidates in the calorimeters components. The electron candidate should, by design, have a significant fraction of energy deposited in the electromagnetic calorimeter $E_{\text{ECAL}}/P > 0.1$. Conversely, as a lepton, deposits in the hadronic calorimeter should be a

low fraction $E_{\mathrm{HCAL}}/P < 0.5$. The electron should also trigger the PRS, $E_{\mathrm{PRS}} > 0.05\,\mathrm{GeV}$. Finally, to remove overlap with muon candidates, electrons are rejected if they also pass muon *loose* requirements as defined in [86].

5.2.3 Stripping Requirements

In order to reduce the number of events stored to disk, the initial reconstruction of data and MC events are stripped in order to discard uninteresting events. In this analysis, events are required to have a basic opposite sign muon electron pair to pass the stripping selection. Each lepton must be reconstructed as a basic particle, with at least one unique track and (for electrons) p_T 15 GeV. Each pair must originate from the same primary vertex and have a positive invariant mass. Once these criteria have been passed other particles such as jets in the events are stored. For MC, the truth information is also stored at this stage.

5.2.4 Track and Lepton Quality requirements

To select isolated leptons a few quality cuts are placed upon them. The muons and electrons are required to have a p_T of 20 or 15 GeV, respectively. Furthermore, the reconstructed lepton must have a $\chi^2 > 0.001$ value. This requires the fit between lepton track and recorded hits to be of a high quality. For electrons additional requirements are used. The fractional error on the electron quality must be less than 10%, $\sigma(p)/p < 0.1$. One wishes to ensure a lepton is isolated from other physics objects. In a cone of $\Delta R = 0.5$ around the electron, the energy of all the charged particles must be less than 2 GeV. A requirement on the impact parameter of electrons is also used, as described in the next section. These additional requirements are not placed upon the muons in the selection, due to more accurate reconstruction of muons in the initial LHCb reconstruction. As described in Section 5.1.4, a major background for events with a correlated pair of muons and electrons are events where jets fake leptons. Specifically, these jets fake electrons at higher rates than muons, so electron quality requirements are an effective discriminant. However, muon quality requirements do not improve signal significance. Due to the low event statistics in the signal and $\epsilon_{\mu iso} < 1$, the loss of signal events motivates this analysis choice.

Impact Parameter

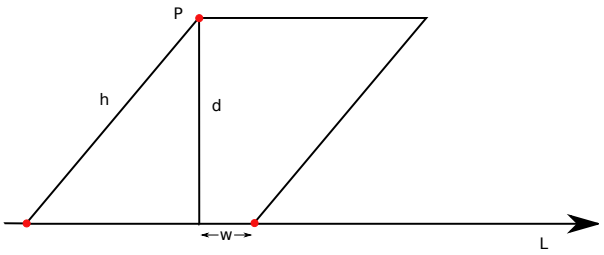

Figure 5.14: The dimensions used in calculating the impact parameter (d) in Equation 5.7, between a line representing the particle track and a point (P) representing the primary vertex.

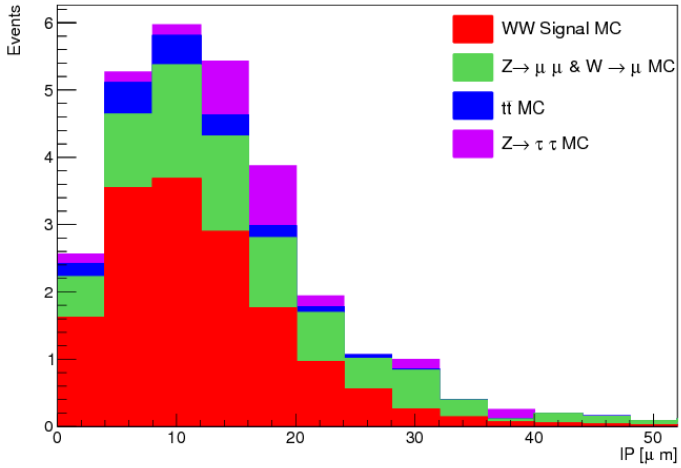

Figure 5.15: IP of electrons in signal and background MC after event pre–selection. The requirement of IP$< 40\,\mu$m removes a large number of single boson states.

Initially produced particles with short lifetimes will decay close to the initial production vertex. W bosons are particles with a short decay distance. The Impact Parameter (IP) is calculated by estimating the closest point of approach of the particle track to the initial collision vertex[5]. To calculate the IP, one forms a parallelogram from the track path and the point of primary vertex. One can calculate the area of the parallelogram using the

[5]To remove bias from this procedure, the primary vertex is refitted without the input of tracks from the particle in question.

height or the impact parameter itself and use the comparison,

$$\begin{aligned} |\overrightarrow{h} \times \overrightarrow{w}| &= A \\ \overrightarrow{d}.\overrightarrow{W} &= A \\ \text{hence d} = \frac{|\overrightarrow{h} \times \overrightarrow{w}|}{|\overrightarrow{w}|}&. \end{aligned} \tag{5.7}$$

Particles such as the W with short decay lengths can be isolated from long decaying particles by their low IP. For this analysis, one requires electrons to have $IP < 40\,\mu$m.

5.2.5 Lepton selection efficiency

The efficiency of selecting leptons is quoted for the collections of requirements upon each lepton. Similar to the calculation of trigger efficiency in Section 5.2.1, the primary method used is the so called tag and probe. $Z \rightarrow l^+l^-$ data and MC are compared for each selection as detailed below, with the resulting figures quoted in Table 5.4. The muon p_T spectrum is modelled comparing $Z \rightarrow \mu^+\mu^-$ MC and selected data in Figure 5.16, showing good agreement. No correction factor for the p_T is applied and no implication on the efficiency of analysis muon p_T cut is seen. The track reconstruction efficiency ($\epsilon_{\mathrm{Track}}$) can be estimated from tag and probe [87], as shown in [88]. The probe muons track are reconstructed TT only tracks, using information from the muon chamber and TT only. Full muon tracks are reconstructed using the VELO and the other tracker components. The rate at which TT tracks match full reconstruction tracks is therefore measured. This is then compared to the same rate in signal MC, with the difference forming the uncertainty on the measurement. The muon ID efficiency (ϵ_{ID}) is again calculated using tag and probe method. Both tag and probe muons are required to be in acceptance, have good quality tracks and have $\mathrm{p}_T > 20\,\mathrm{GeV}$. Tag particles additionally pass the trigger requirements and pass the $isMuon$ requirements.

Electron reconstruction and resolution is poorer than for muons in LHCb, due to bremsstrahlung and detector effects such as ECAL punch through. Efficiencies for electron reconstruction are calculated in the same manner as for muons, but additional nuances have to be considered. This has been evaluated in the $Z \rightarrow e^+e^-$ analysis at $\sqrt{s} = 7\,\mathrm{TeV}$ [85] and is the soon to be published $\sqrt{s} = 8\,\mathrm{TeV}$ analysis [89]. The track reconstruction efficiency ($\epsilon_{\mathrm{Track}}$) represents the likelihood an electron within the η and p_T acceptance has a long track reconstructed. Electrons with insufficient tracking hits will

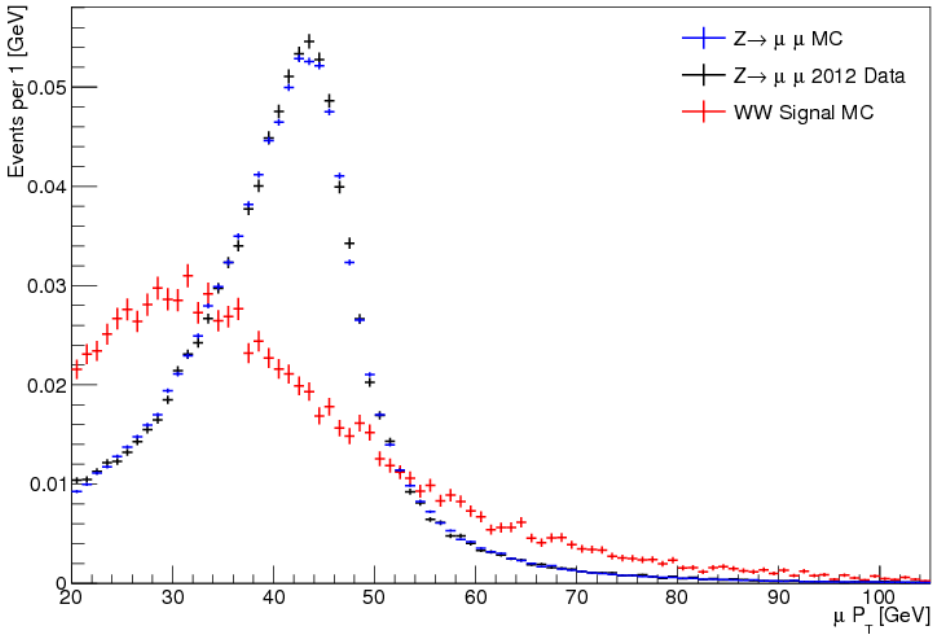

Figure 5.16: Agreement of muon p_T spectrum in $Z \to \mu\mu$ MC and data, with the signal WW signal overlaid.

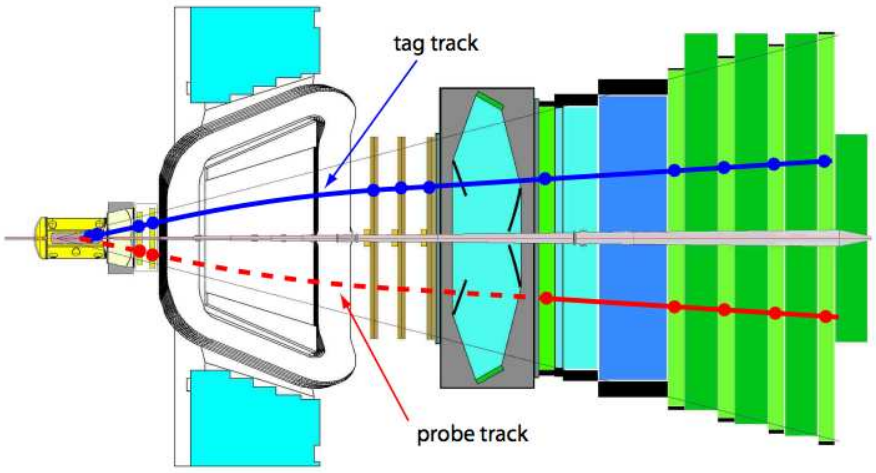

Figure 5.17: Reproduced [87] diagram showing the information used to reconstruct full muon tracks used for tagging and so called TT tracks using the TT and muon chambers for probe muons.

be reconstructed as photons due to energy deposits in the ECAL. In order to estimate this effect, tag and probe methods are applied to $Z \to e^+e^-$ MC and data events in the Z mass window. In order to increase tag lepton purity, tag events are selected with tighter calorimeter requirements; $E_{\mathrm{ECAL}}/P > 0.2$ and $E_{\mathrm{HCAL}}/P < 0.01$. Probe electrons and photons are selected with $E_T^{\mathrm{ECAL}} > 10\,\mathrm{GeV}$ and $\Delta\phi > 0.75\pi$ were ϕ is the angle

Requirement	Efficiency %	Uncertainty %
ϵ_{Trig}	76.5	3.0
ϵ_{SPD}	84.2	2.7
ϵ_{Track}	95.4	0.2

Table 5.4: Percentage efficiencies in the selection of muons in this analysis and the uncertainty on each value, using results from [88].

between tag and probe. The probe is designated an electron if it has a track and a photon otherwise. However, the $e+\gamma$ channel in data will have contributions from non–Z processes. A template fit is therefore applied, with the erroneous background's template modelled by inverting isolation cone requirements.
The electron kinematic efficiency (ϵ_{Kin}) is related to the correct reconstruction of electron p_T. Bremsstrahlung from the electron affects the rate of electrons passing the p_T requirements. The p_T spectrum in Z data is scaled by a factor α that provides a best fit with MC. This factor is consistent, within errors, with unity in all bins barring the extremum of y_Z. The Particle IDentification (PID) efficiency is a measure of electrons falling outside acceptance, failing calorimeter requirements and other PID criteria. Again the tag and probe method is applied to Z MC and data and then compared, similar to the muon calculation above.
$Z \rightarrow \mu\mu$ MC and data is used to evaluate the systematic uncertainty on IP by the

Requirement	Efficiency %	Uncertainty %
ϵ_{Track}	95.5	0.5
ϵ_{Kin}	71.2	0.4
ϵ_{PID}	91.5	4.0

Table 5.5: Percentage efficiencies in the selection of electrons and the uncertainty on each value, as per the LHCb $Z \rightarrow e^+e^-$ analysis [89].

difference in the selection efficiency. Good agreement is found as shown in Figure 5.18.

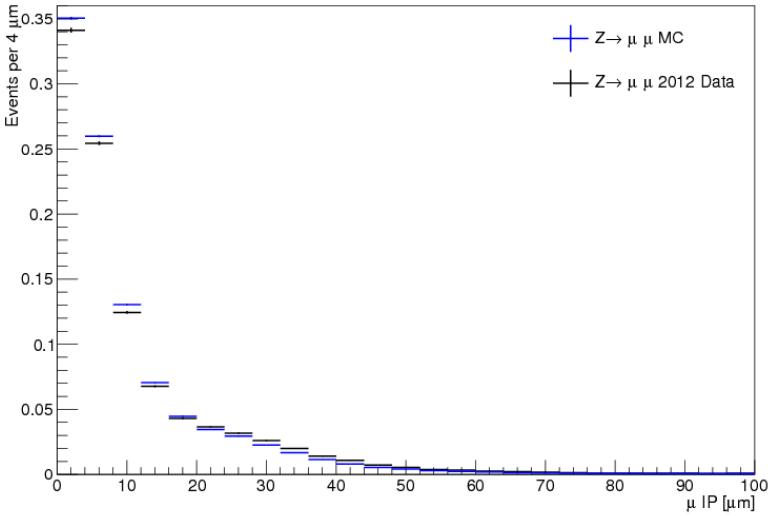

Figure 5.18: Muon IP in $Z \rightarrow \mu\mu$ simulation and data used for estimation of selection systematics.

5.3 Discriminating Variables

To isolate the signal events from backgrounds passing the basic trigger and stripping selection, one places requirements on events that are preferentially met by the signal. These variables and the requirements placed upon them are detailed below.

5.3.1 Invariant Mass

The initial particle in a two body decay can be characterised by the invariant mass. Invariant mass is a Lorentz invariant quantity identifying the mass of the initial particle in the rest frame. It can be calculated from the four–vectors of the two final state bodies,

$$m_{inv} = \sqrt{(E_1 + E_2)^2 - (P_{1,x} + P_{2,x})^2 - (P_{1,y} + P_{2,y})^2 - (P_{1,z} + P_{2,z})^2} \qquad (5.8)$$

and is particularly useful for identifying Z decays in a window around the known Z mass. Decays with invisible particles, such as $Z \rightarrow \tau\tau$ have smeared invariant mass distributions. In this analysis the requirement $m_{e\mu}$ >45 GeV is placed. It can also be seen that the fake jet backgrounds contain small values of invariant mass, particularly in the $Z \rightarrow \mu^-\mu^+$+jets channel as the mass of one of the muons (and some of the jet) is missing. The efficiency of this selection is expected to be high, as leptons with reconstructed kinematics lower than their true values are expected to be lost in the individual lepton

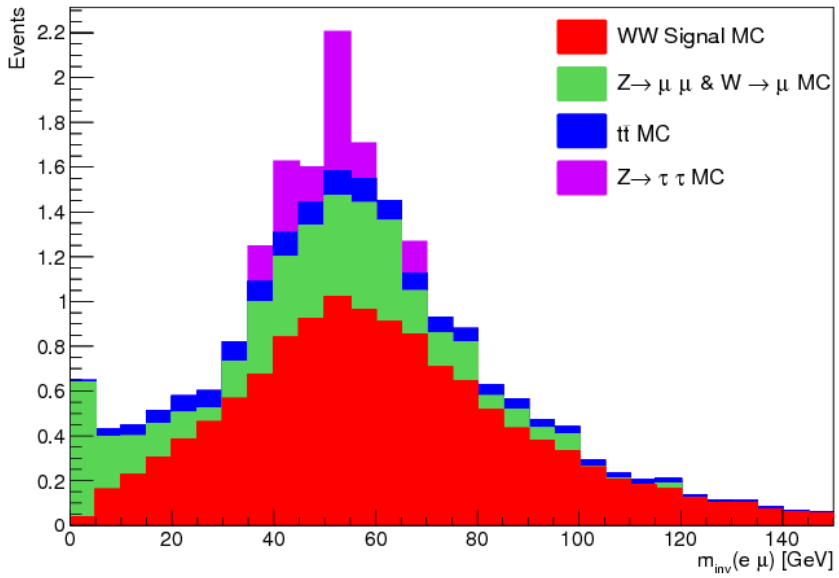

Figure 5.19: Invariant mass of the electron and muon in signal and background MC, after event pre–selection and electron IP requirements. The selection of events with $m_{e\mu} > 45\,\text{GeV}$ serves to preferentially remove single electroweak boson events.

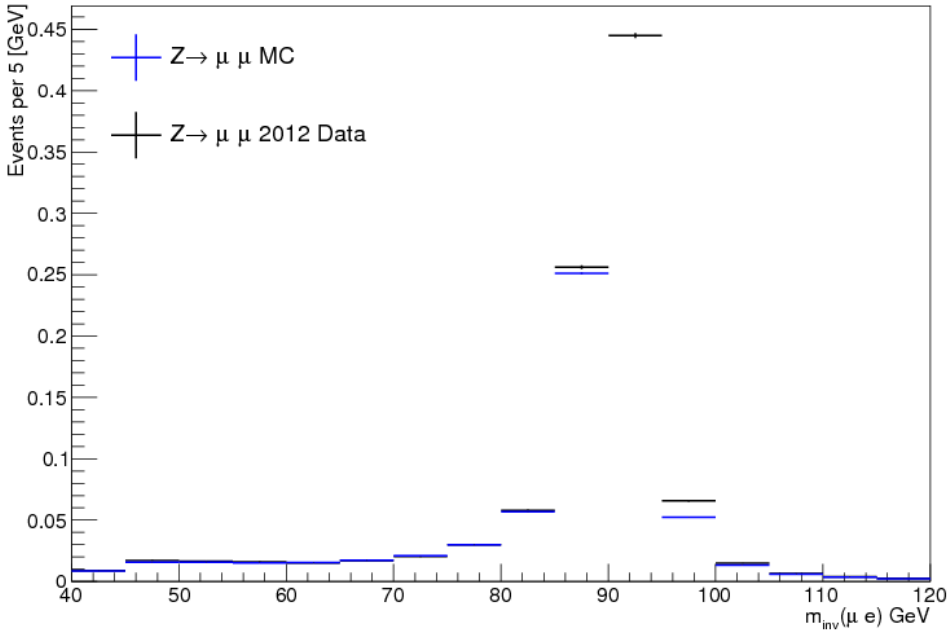

Figure 5.20: Invariant mass of muons in selected $Z \to \mu\mu$ simulation and data used for estimation of selection systematics.

p_T selections. Indeed Figure 5.20 shows good agreement in data and MC, resulting in an invariant mass selection efficiency of 99.0 ± 0.2 %.

5.3.2 Jet Veto

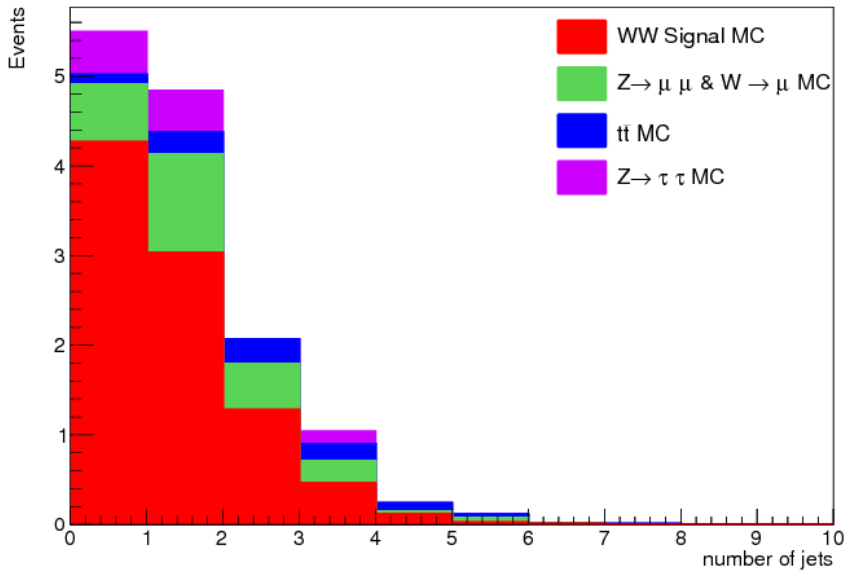

Figure 5.21: The multiplicity of jets in the signal and background MC, after event pre–selection and invariant mass requirements. The WW signal is seen to have low multiplicity, as contrasted with the fake jets background and $t\bar{t}$.

At leading order, one expects no jets in the WW signal. Initial and final state radiation can produce partons that will subsequently hadronise, although one would expect these jets to have low p_T. Jets in the LHCb experiment are fed, using the reconstructed object tracks, into the FASTJET variation of the anti–k_t algorithm[66]. The $R = \sqrt{\Delta\phi^2 + \Delta\eta^2}$ cone size used is 0.5 with a minimum p_T of 5 GeV. Each jet (and at least two of it's daughters) are furthermore required to share the primary vertex as the muon–electron candidate pair. The jet must contain a charge particle with p_T > 1.8 GeV, but no charged particle may constitute more than 75% of the total jet p_T. These definitions are used to reject events with jet candidates with $p_T > 5$ GeV. Figure 5.21 shows the jet multiplicity in various MC samples. The jet veto can be seen to drastically reduce fake jets backgrounds as well as $t\bar{t}$ events as per Section 5.1.2, whilst losing just over half of the signal events as shown in Figure 5.21. This cut increases signal purity from 0.326 to 0.612. The efficiency of a jet veto will be necessarily high, as it is rare for events with no true hadronic content to trigger jet reconstruction. However when true jets are present, the events can pass the jet veto, referred to here as fake jetless events. Jet reconstruction efficiency has been seen to be as low as 75% at around p_T =10 GeV, rising to 96% for higher p_T [90][91]. Fake jetless events are much more

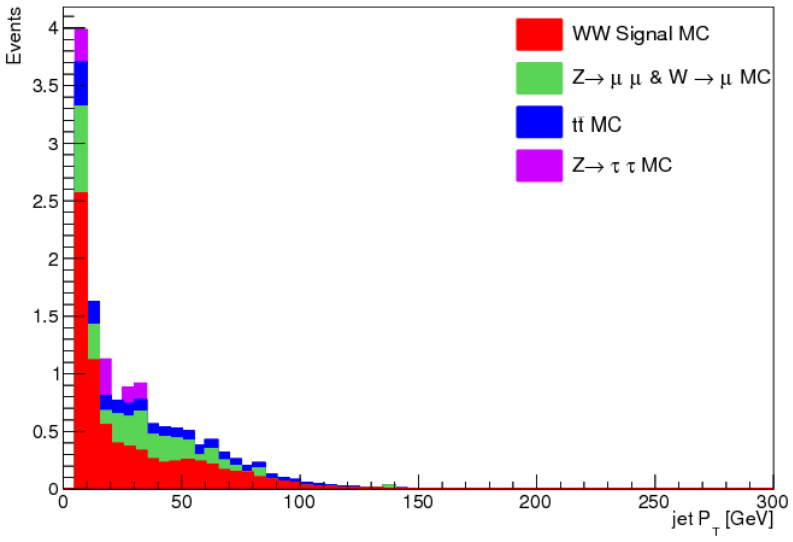

Figure 5.22: The p_T spectrum of jets in the signal and background MC, after event pre–selection and invariant mass requirements. WW events have large proportions of low p_T jets, specifically relative to the $t\bar{t}$ process.

likely at low values of p_T. Additionally a true jet containing a heavy quark such as a b has more mass to hadronise, causing more showering and lowering fake rates. Processes producing quarks in the LO process, such as $t\bar{t}$, result in high p_T or high mass jets, which are unlikely to fake jetless events. Processes that have only ISR/FSR jets however, have a greater proportion of low p_T and low mass jets. The p_T spectrum in Figure 5.21 shows WW as one such process. A systematic uncertainty on the jet veto is applied to allow for fake jetless events. An average jet reconstruction efficiency is calculated for WW truth jets, applying the efficiency according to the jet p_T. The rate of failed reconstruction is around 14% and this is applied once to the proportion of WW truth events with 1 jet, twice to events with 2 jets and so forth. The systematic error can then be estimated as 4.2%.

5.3.3 Distance of Closest Approach

For two particles decaying from the same original object, extrapolating tracks backwards should result in near overlap. The IP Distance of Closest Approach (DOCA) variable is

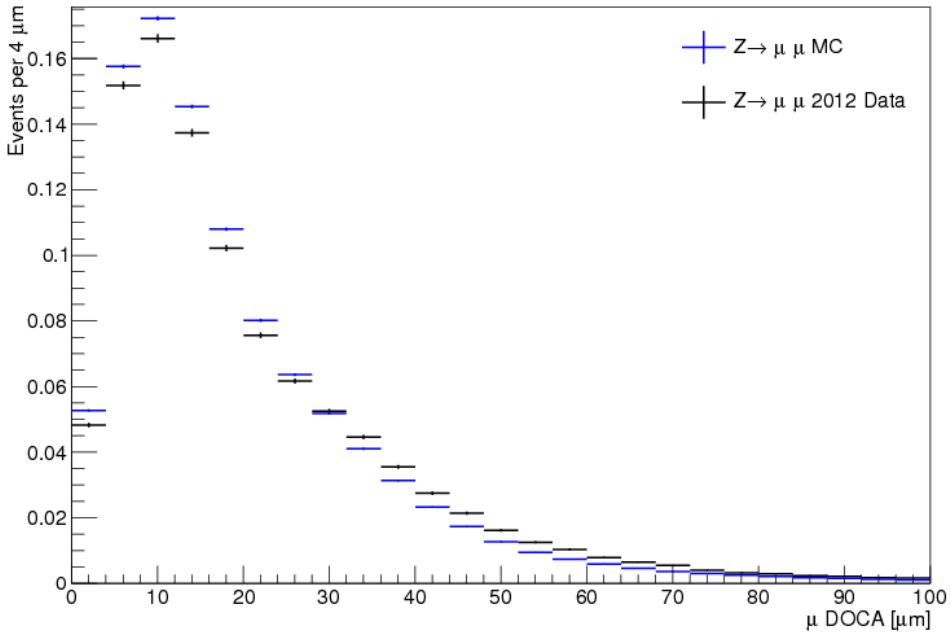

Figure 5.23: The distance of closest approach of the two muons in Z decay for both MC and data, used to calculate the systematic uncertainty.

a measure of this overlap for two leptons and is formed from I_1 and I_2, the IP of the leading leptons such that

$$DOCA = I_1^2 + I_2^2 - 2I_1 I_2 \cos(\Delta\phi) \tag{5.9}$$

where $\Delta\phi$ is the angle between the leptons. For decays with one visible step such as WW, the DOCA should be small as the two particles do indeed originate from the same decaying particle. Multi–step decays will have the two leptons pointing back to their parent particles, at two distinct points, resulting in a marginally larger DOCA. Due to the high precision of the VELO tracker in LHCb, it is possible to measure the differences in this variable, as shown in Figure 5.24, providing a final strong discriminant. The efficiency of the selection is again calculated by applying the tag and probe method in Z MC and data, as shown in Figure 5.23.

5.3.4 Final Selection

The resulting final selection results in 4 data events with an expectation of 3.90 events in simulation, of which 3.20 are attributed to signal. Despite the low statistics available in the dataset, it is possible to select a pure sample of diboson signal.

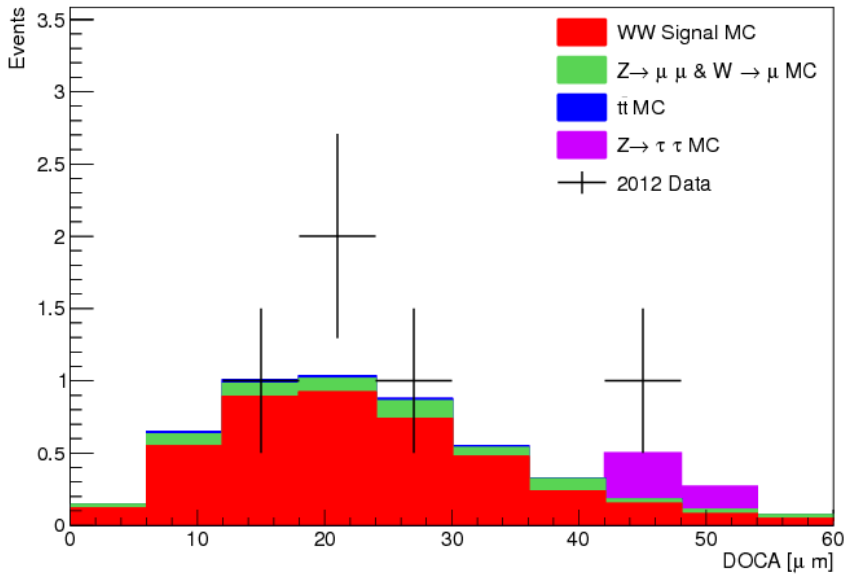

Figure 5.24: The distance of closest approach of the electron to the muon for MC and data, after event pre–selection, invariant mass requirements and jet veto requirments. The requirement $< 40\,\mu$m is the last selection in the analysis.

Requirement	Efficiency %	Uncertainty %
Impact Parameter $< 20\,\mu$m	96.3	0.7
Invariant Mass $> 45\,$GeV	99.9	0.2
DOCA $< 20\,\mu$m	95.4	0.2

Table 5.6: Percentage efficiencies of the discriminating variable selections of electrons. The jet veto is not included here; rather than an efficiency a systematic uncertainty is applied as per Section 5.3.2.

Contribution Source	% Contribution
Jet Veto Systematic	4.2
Acceptance Uncertainty	0.1
PDF Simulation Systematic	$^{5.6}_{5.0}$
Luminosity Uncertainty	1.22

Table 5.7: Global Uncertainties not arising from selection efficiencies.

Cut Selection	# Signal MC	# Background MC
Stripping candidates	30.8	931
Muon passes trigger	21.3	590
Muon $p_T > 20\,\text{GeV}$	19.3	520
Electron $p_T > 15\,\text{GeV}$	15.6	41.4
Electron IP $< 40\ \mu$m	15.4	37.9
Electron cone $< 2\,\text{GeV}$ (see 5.2.4)	12.8	16.8
$m_{e\mu} > 45\,\text{GeV}$	9.18	7.22
Jet Veto	4.26	1.43
DOCA $< 30\,\mu$m	3.20	0.70

Table 5.8: Table of the selection requirements used and their effect on signal and the sum of background MC.

5.4 Luminosity and Acceptance Uncertainty

The instantaneous luminosity of the data sample is a key variable in any LHCb analysis. This quantity is measured using two direct methods, allowing for cross checks and a reduced uncertainty [92]. Firstly the well established Van der Meer scanning method [93] is used. One LHC beam is moved in the transverse plane in order to scan the profile of the other. The rate of interactions is measured for each displacement value as the scan is performed, forming a beam profile. Secondly, the beam gas imaging method is used [94]. As the beam interacts with residual gas in the LHCb pipe, tracks are deposited onto the VELO and vertices formed. A transverse beam profile can be formed in a non–disruptive way, allowing for luminosity measurements during physics running. These two measurements use Equation 3.4 to calculate the luminosity and the associated error. For the electroweak group stripping line in 2012 data, the integrated luminosity is 1.99 fb^{-1} with a 1.22% uncertainty. Furthermore, for the delivered luminosity, one must calculate the uncertainty on acceptance, i.e the fraction of event outside acceptance leaking inside and being reconstructed. With no jets in signal events, it can be seen from MC truth it is very rare for leptons to leak into acceptance.

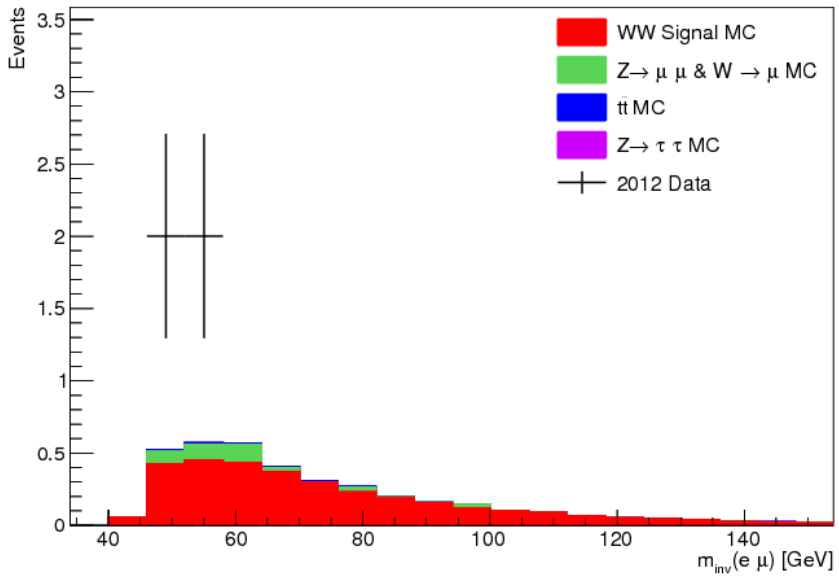

Figure 5.25: The final data events after all selections binned by the invariant mass of the two reconstructed leptons. This includes the full 2012 LHCb dataset , with integrated luminosity of 1.99 ± 0.02 fb^{-1}. The contributions from the remaining MC samples as described in Section 5.1 are overlaid.

5.5 Results

After the full selections are performed, the background processes have been greatly reduced. Four candidate data events survive the full selection, one such event is visualised in Figure 5.27. Agreement is shown between the number of simulated and data events is shown in Figures 5.25 and 5.26. Equation 5.1 can used to calculate a value of the fiducial cross section,

$$\sigma_{fid} = \frac{4.00 - 0.76}{0.34 * 1.99}\text{fb} \tag{5.10}$$

and consequently accounting for the systematic and statistical uncertainties in tables 5.4, 5.5, 5.6 and 5.7 respectively; a value of

$$\sigma_{fid}(\sqrt{s} = 8\,\text{TeV}) = 4.7 \pm 1.5(\text{stat.}) \pm 0.5(\text{syst.}) \pm 0.1(\text{lumi.})\,\text{fb} \tag{5.11}$$

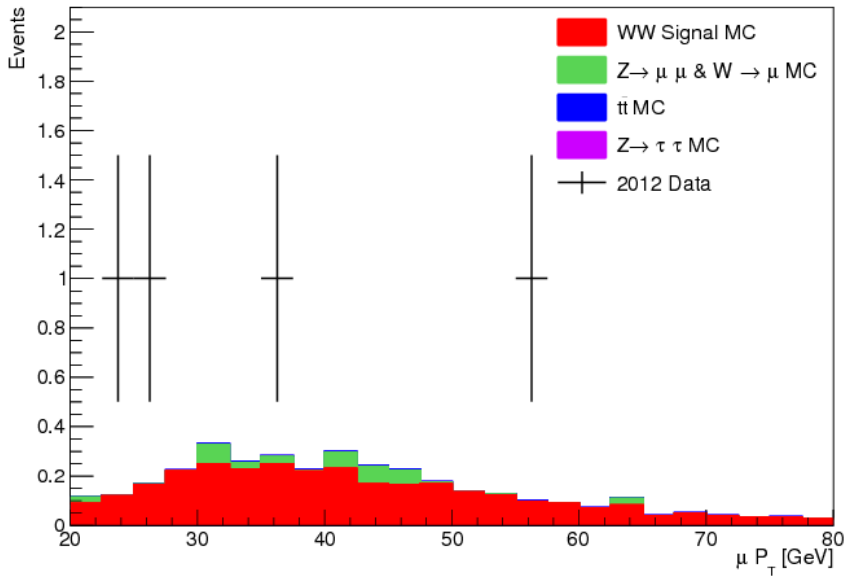

Figure 5.26: The final data events after all selections binned by the muon p_T. This includes the full 2012 LHCb dataset , with integrated luminosity of 1.99 ± 0.02 fb^{-1}. The contributions from the remaining MC samples as described in Section 5.1 are overlaid.

is calculated. This can be compared to the theoretical prediction calculated from the WW simulation

$$\sigma_{theo}(\sqrt{s} = 8\,\text{TeV}) = 4.6 \pm 0.1(\text{stat.}) \pm 0.3(\text{syst.})^{0.3}_{0.2}(\text{PDF.})\,\text{fb} \tag{5.12}$$

which shows agreement within the uncertainties calculated. Somewhat unsurprisingly, the main sources of uncertainty in this measurement are statistically driven. The low number of data events in the signal region contributes to a large statistical error on the measurement. The main background contribution is indirect two lepton backgrounds from single W or Z events. As discussed in Section 5.1.4, the fraction of single boson events entering the signal region is very low, causing small MC statistics for these samples. This results in a 23% statistical uncertainty on the indirect background estimate. In contrast, the large acceptance and reconstruction efficiency of WW MC produces a small statistical uncertainty on the estimated number of signal events. The largest systematic uncertainty comes from the choice of PDF set used and the uncertainty in measured input values. This is to be expected, as the low x parton values in the WW process are not well known, as discussed in Section 2.5. Indeed the aim future measurements, could be to measure this PDF contribution. Comparing these measurements to the 2012

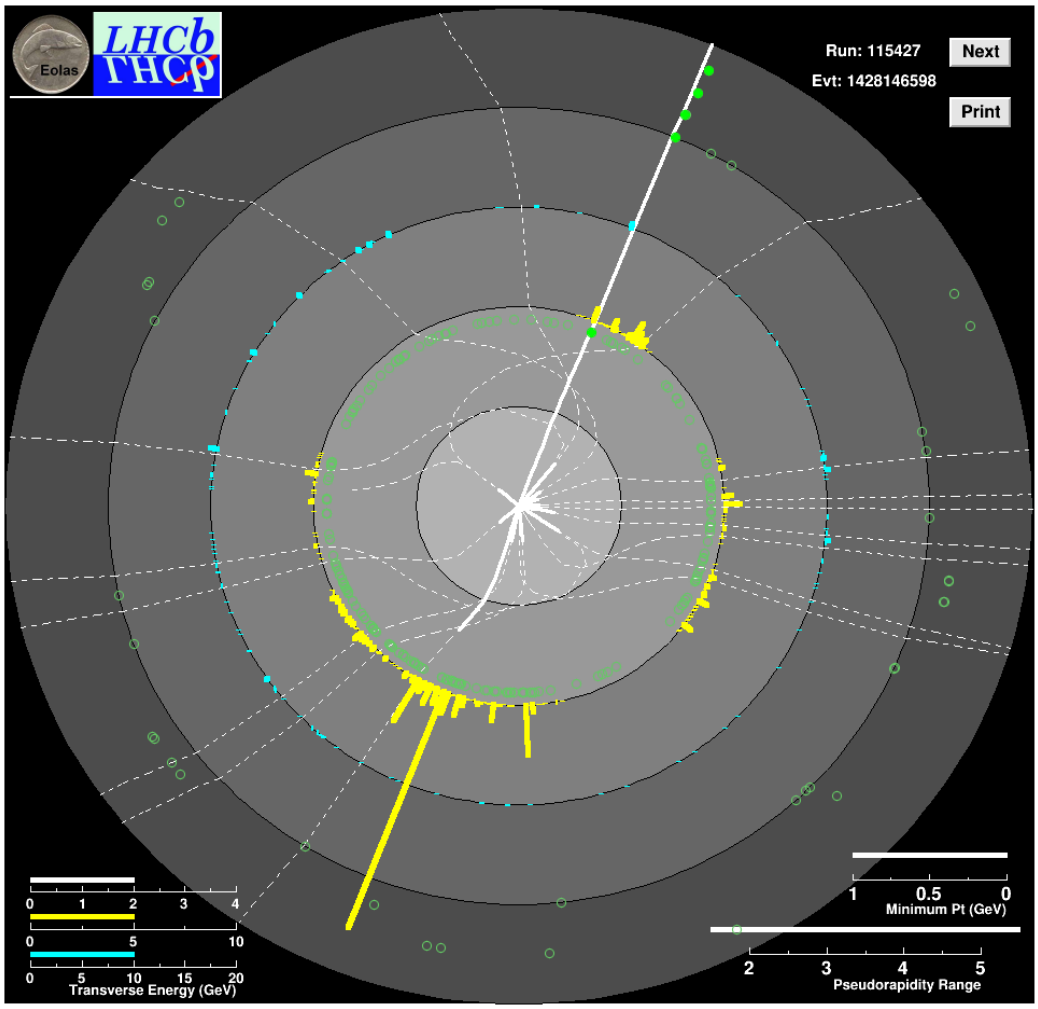

Figure 5.27: A candidate data event reconstruction visualised using Eolas. The centre of the display represents the LHCb collision point, with radial distance the z co–ordinate system. Each radial disk represents a detector component, with a representation of the basic reconstructed output. White dotted lines represent tracks, with solid white lines representing high p_T tracks. The ECAL (HCAL) deposits are represented in the third (fourth) layer with yellow(blue) bars, related to the amount of energy deposited. Finally hits in the muon layers are portrayed with green circles which are solidly filled if matching a track in reconstruction.

ATLAS measurement for $WW \to e\mu$ corresponding to 20.3 fb^{-1},

$$\sigma_{fid}(\sqrt{s} = 8\,\text{TeV ATLAS[95]}) = 377.7 \pm^{6.9}_{6.5}\,(\text{stat.})^{25.1}_{22.2}(\text{syst.})^{11.4}_{10.7}(\text{lumi.})\,\text{fb}$$

one can compare the analysis strengths and weaknesses. In the ATLAS analysis, high quality electrons and muons are selected with large E_{T}^{m}, a jet veto and a requirement on the angle between leptons and E_{T}^{m}. Pairing a higher recorded integrated luminosity with

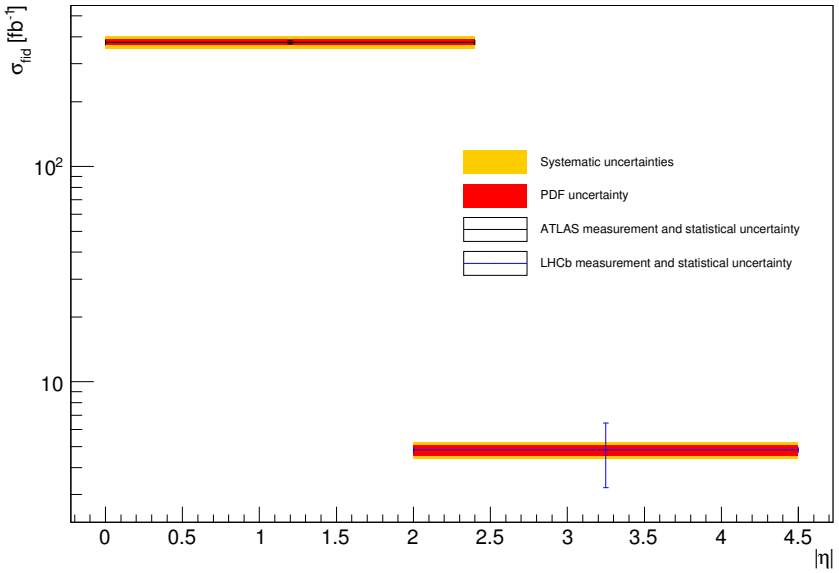

Figure 5.28: *WW* fiducial cross section measurement in this thesis compared to the ATLAS measurement, plotted as a function of the absolute value of pseudorapidity $|\eta|$. The differences in scale of statistical uncertainties on the two measurements can clearly be seen. Regions with large values of negative η only accessible by the LHCb measurement probe unique PDF space, as shown by Figure 2.7.

greater angular acceptance results in a much larger number of data events (5067) in the ATLAS analysis, and consequently lower statistical uncertainty as shown by Figure 5.28. Futhermore, it is possible to estimate W/Z fake events using fully data driven methods, using the matrix method described in Section 4.4. Due to low event statistics, this is not currently possible with the LHCb 2012 dataset. Despite these limitations, fractional systematic uncertainties are within 10% agreement in both analysis.

The RooStats package [96] is used to analyse the agreement of the observed data with both a signal plus background and a background only hypothesis. For both hypothesis, toy experiment simulations are created in a method similar to [97]. For each individual toy experiment a likelihood value is calculated. For the former, the number of expected events is modelled using a Poisson distribution, with the variance equal to the sum of signal and background events. The number of background events is treated as a nuisance parameter by modelling its fluctuations with a Gaussian distribution, with standard deviation equal to the uncertainty in background, to produce a likelihood,

$$L = \text{Poisson}(\text{n}|\text{s}+\text{b})\text{Gaussian}(\text{b}, \sigma_\text{b}) \tag{5.13}$$

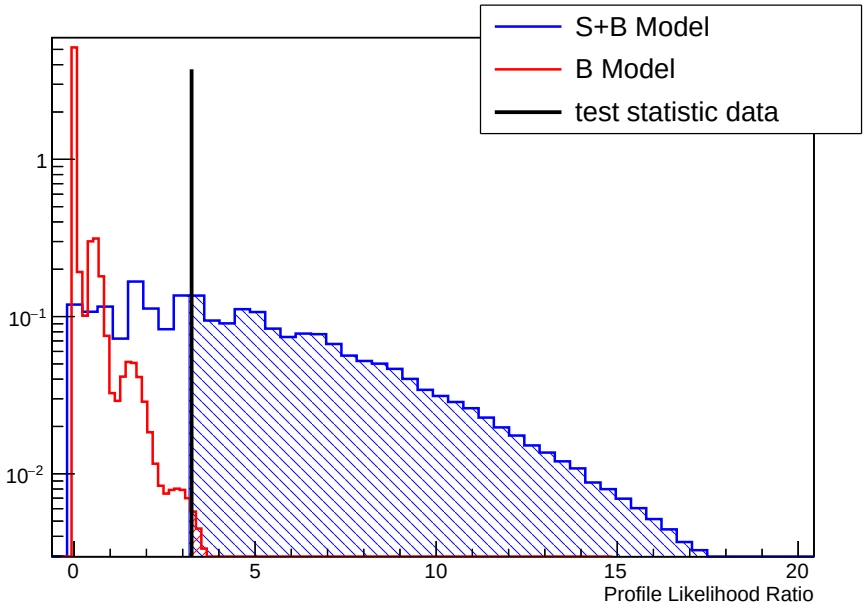

Figure 5.29: Toy experiment profile likelihood ratio plot produced for the background only and signal plus background hypothesis.

and similarly for the latter without any signal contribution. A ratio is formed with the observed data (n_{obs}), by dividing each likelihood by $L(n|\hat{s}, b)$, where $\hat{s} = n_{obs} - b$. For the background only model, 10 million toy experiments are created and a further 1 million toy experiments are created for the signal plus background. Figure 5.29 shows the distributions of the profile likelihood ratios for both hypothesis. The background only model has a p–value of $(4.3 \pm 0.3) * 10^{-3}$, suggesting a low probability of the null hypothesis fitting the observed number of data events. A signal significance is calculated from the fraction of toy experiments for the signal hypothesis that are bounded by the test statistic[6]. The significance of the signal can the be calculated as 2.6σ. The potential for improving the measurement in future LHCb runs is discussed in the next chapter.

[6]The test statistic is calculated using the likelihood value $L(n_{obs}|s, b)$.

Chapter 6

Future potential of diboson searches

Following from the analysis performed in the last chapter, this chapter aims to ascertain the potential of diboson searches in the future running of the LHCb experiment. Pertinent to this are the future run plans for LHCb and the scheduled upgrades, briefly outlined below.

6.1 Run Two

At the time of writing, the LHC apparatus has been in Long Shutdown One (LS1) since early 2013. This planned shutdown was to enable the upgrade of the superconducting dipoles, in order to increase the magnetic field strength and in turn the energy of the beam. Once these upgrades are finished in Spring 2015, the LHC will begin running again, initially at $\sqrt{s} = 13\,\text{TeV}$. Contingent on machine operation and testing, the machine may be increased to running at $\sqrt{s} = 14\,\text{TeV}$ with use of LS2. Running until 2018, it will be possible to collect 5 fb^{-1} of LHCb data.

6.2 The LHCb Upgrade

After run two, Long Shutdown Two (LS3) will begin in 2018. The machine will be upgraded into the High Luminosity LHC (HL–LHC), with instantaneous luminosity of $O(\mathcal{L} = 10^{33}\,\text{cm}^{-2}\text{s}^{-1})$[99]. Upon resumption of beam in 2023, it will be possible to collect up to 50 fb^{-1} of LHCb data. In this regime event rates will increase greatly. For example bunch crossing at LHCb will increase from 2.3 to 4 [100], increasing the occupancy in

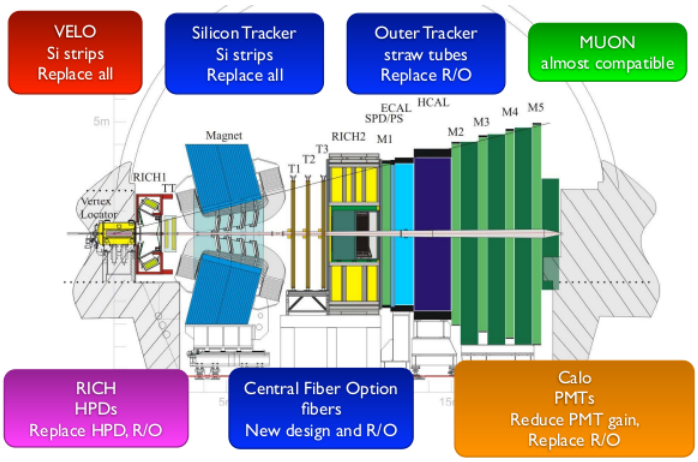

Figure 6.1: Upgrade Schematic[98].

the detector in addition to greatly increasing radiation damage rates. In order to sustain precision physics in this environment, an upgrade of the detector is necessary. Most of this upgrade currently planned to take place in LS2, although work will continue into LS3. One of the main upgrades will be in the trigger system. Currently the L0 stage have a 1 MHz rate, which is a bottleneck for the other trigger systems. In the HL–LHC, this will be plainly insufficient. The upgrade will include a new 40 MHz L0 trigger to ease this burden[100]. Even with this infrastructure, there will be a necessity to increase the p_T thresholds for some trigger lines. In the diboson analysis above a $p_T > 15\,\text{GeV}$ line is used, a higher p_T threshold than many other lines. If this were to prove problematic, dilepton triggers could be implemented at the low p_T limits. Given the leptons are decaying from high mass bosons, a $p_T = 15 - 20\,\text{GeV}$ threshold is not a significant issue. In the upgrade the outer tracker, calorimetry and muon systems can be used in a similar way to the current setup, with some replacement of components due to radiation damage and improved readout electronics. The VELO and inner tracker semiconducting sensors will need to be completely replaced to proof against radiation damage. In the RICH detector, the aerogel medium will need to be replaced. More detail of these changes can be found in the respective technical design reports [101, 102, 103, 104]. The detector is expected to maintain the current high standards of object reconstruction despite the challenges.

Process	13 TeV Cross Section [pb]	No. of events in run two
WW	112.6	772.3
ZZ	15.99	72.40
Process	14 TeV Cross Section [pb]	No. of events in HL–LHC
WW	124.3	8758
ZZ	17.72	1043

Table 6.1: Tables of NLO Cross Section values for future LHC $\sqrt{s}$ values. Also shown are estimates of the number of events in the acceptance during run two and HL–LHC, calculated using POWHEG–BOX.

6.3 Production Rates at 13 and 14 TeV

The increase of LHC $\sqrt{s}$ is beneficial to diboson searches as the cross section for the processes increase, as shown in table 6.1. $t\bar{t}$ cross sections rise quickly in the future

LHC runs, with NLO values[105] of 806.1 pb at 13 TeV and 953.6 pb at 14 TeV. This will result in roughly five hundred events per fb^{-1} of data in the LHCb leptonic acceptance. Assuming the same reconstruction efficiency as the WW analysis above, predicts an event every four fb^{-1}. This is still a manageable ratio compared to the signal event rates (see below). Furthermore, targeted $t\bar{t}$ analysis have begun at LHCb, facilitatating a new btagger [81]. Indeed due to similar event topologies (barring jets), in future these two analyses could be performed side by side. In the analysis performed, it is seen that MC for single EW bosons overestimates the rates of jets faking electrons. A semi data driven approach is used to measure this overestimation and scale the MC appropriately. In a future analysis, with larger numbers of candidate events it would be beneficial for a larger study on jets and electrons to be performed. New simulations could be written and iteratively tuned using the direct data driven methods. This work would be beneficial to other analysis such as $Z \to ee$ and $t\bar{t}$ measurements and to the ongoing work on jet methodology and b tagging within the experiment.

6.4 Estimate of analysis potential

Using the WW analysis performed above, one can estimate the expected number of reconstructed events in each run. Assuming the same efficiency of reconstructing WW pairs, one expects over two hundred and fifty (three thousand) reconstructed events

in run two (HL–LHC). With a much higher number of expected events, it should be possible to reduce the n_{obs} contribution to the statistical uncertainty from 25% of n_{obs} to around 6.1(1.8)%. With study of the single boson faking electrons as suggested above, it will be possible to additionally reduce the statistical uncertainty on the measurement significantly. The measurement can hence become competitive with the other LHC experiments.

The ZZ channel has potential due to the unique final state signature produced. Four high p_T leptons in the forward region are not at all common. One of the main real backgrounds for ZZ searches here is $H \to ZZ$, although it has a low cross section. Higgs events largely favours transverse production leading to a small acceptance in LHCb, leading to just over a single event predicted with acceptance in run two. Furthermore, at leading order there are no invisible particles in this decay. Otherwise one expects fake backgrounds arising from jets faking leptons. For a single Z event, two jets must fake leptons, which is a very rare process indeed. WZ production only requires one fake to count as background, however it has a comparably low cross section, like the signal. Obviously this is also a diboson sample, so could be counted as a secondary signal in the four lepton channel. ZZ events can be selected by selecting four isolated leptons, with two opposite sign pairs having invariant mass within the Z window. This further selects a high purity sample. As stated table 5.1, ZZ production rates are too low for an analysis in 2012 data. However, table 6.1 shows the higher event rates in future running of the LHCb experiment. Here, one can use the event selection efficiency from the previous LHCb Z analyses and internal notes [85, 88, 89] to estimate search potential. In future experiment running, one would not expect the detector performance to lower these measured values, indeed with improved components it may possibly increase. $Z \to \mu\mu$ produces clean events, often used for calibration, with selection efficiency of $73.7 \pm 0.2\%$. $ZZ \to ee$ events are less well measured due to the LHCb experiments' poor electron momentum resolution, with selection efficiency of $31.9 \pm 0.6\%$. In run two ZZ selection with these efficiencies one would expect to reconstruct around twenty events and in HL–LHC almost two hundred events. With such a clean signal, this diboson measurement could yield precise results [1] in this interesting physics sector. With a precise measurement such as this limited by systematic not statistical uncertainty, the possibility arises of probing the PDF uncertainty based on the input PDF [22]. Figure 6.2 shows the reach of LHC collisions based on the x and Q^2 scale, with the rapidity overlaid. It is clear from the diboson energy scales and LHCb rapidity reach, this is a promising possibility.

[1] This is especially true in the four muons decay channel. High p_T muons are very well measured in LHCb, although this would cut the number of events by a factor of four.

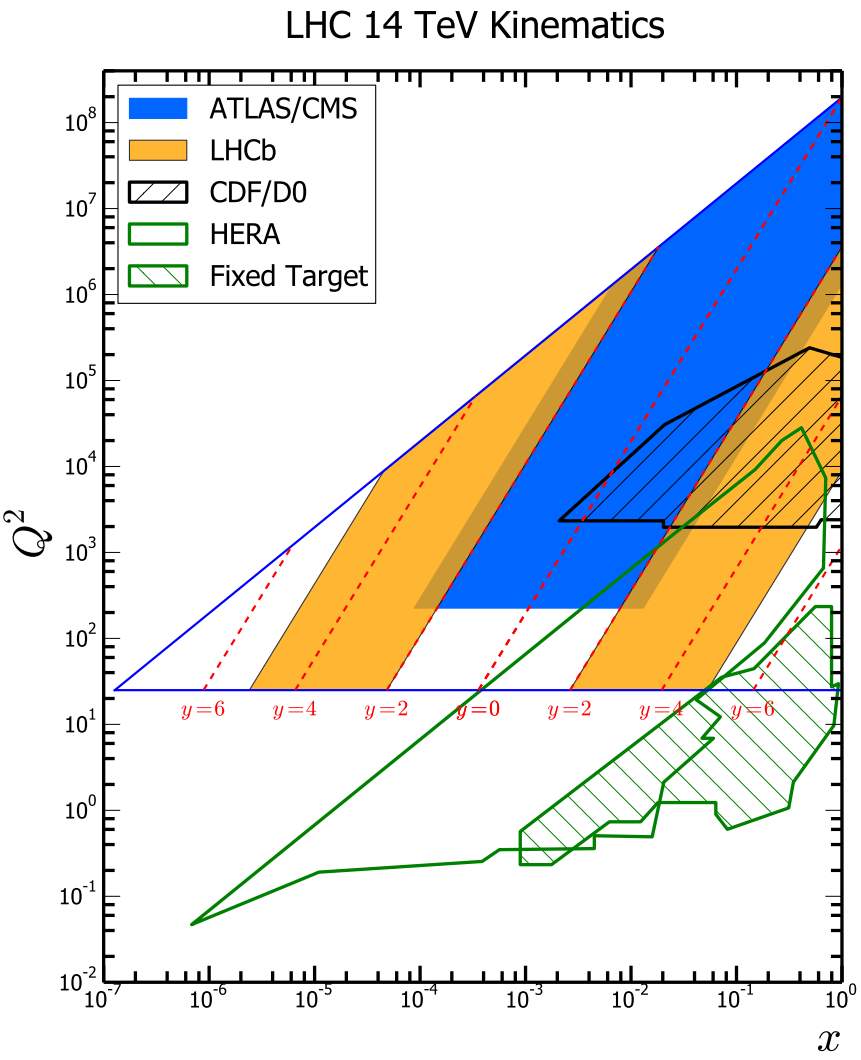

Figure 6.2: Plot showing the accessible region in the x–Q^2 PDF range for LHCb and other experiments at 14 TeV. The low x region is uniquely accessible in LHCb. With increased event statistics, measurements of high Q^2 WW and ZZ processes can be used to input into PDF fits. Adapted from [22] by J. Anderson.

Chapter 7

Conclusion

The initial run of the LHC apparatus ended in early 2013, with a number of notable successes, most famously the observation of a particle consistent with a Higgs Boson. However, there are remaining a number of significant unanswered questions in the field of particle physics that the LHC can continue to address. In the early part of studying for this thesis, (chapter 4) one such question was the focus, supersymmetry searches on the ATLAS experiment. Supersymmetry is an extended, unproven model aimed at addressing the dark matter problem and the hierarchy problem. A search for the production of pairs of stop, the supersymmetric partners of top quarks was undertook. The specific scenario tackled were stop masses almost degenerate with the top mass. In this model, it is shown that it is very difficult to dissociate signal events from top pair production, although a composite variable $\sqrt{s}_{\text{min}}^{(\text{sub})}$ based on the mass comparison of visible to invisible final state particles achieves some success. Particular effort in this analysis was focused on estimating the amount of background events where jets fake leptons. A data driven matrix method approach was used to estimate the event rate of this background in an efficient way. The results of this analysis were not to find any new physics, but to improve the exclusion limits for stop production with such masses.

The LHCb experiment was designed as a precision forward arm spectrometer, with the aim of probing CP violating effects in the b physics sector. It has and will continue to succeed in this role, however it is also possible to use the attributes of the experiment for a wide range of physics. Probing the electroweak sector with the LHCb experiment is also possible due to the high precision, vertexing, tracking and lepton identification. These analyses are particular useful in probing parton distribution functions given the experiment's unique reach in regions of low Björken–x variable.

This thesis presents a technique for the measurement of a pair of WW bosons at the LHCb detector. Each W decays leptonically, but the channel with $W \rightarrow e + \nu_e$ and

$W \to \mu + \nu_\mu$ is chosen. This channel has a clean signal, but does not have large direct single boson backgrounds as the dimuon or dielectron channels do. Events are selected using the LHCb single muon trigger, with a electron–muon pair in the LHCb acceptance and with $p_T > 15(20)\,\text{GeV}$ and invariant mass $> 45\,\text{GeV}$. Electrons are further refined by requiring isolation and small separation from the event primary vertex. To reject $t\bar{t}$, QCD and other EW events, events with jet content are vetoed. Finally the distance of closest approach between the two leptons is required to be less than 40 μm.
These requirements are very effective at reducing backgrounds with the same final state leptons, with the main background coming from single electroweak bosons with emitted jets faking an electron. This phenomena is poorly modelled in MC and a correction factor is applied from comparisons of $Z \to \mu\mu$ in data and MC. The first cross section measurement in the forward region is found to be

$$\sigma_{fid}(\sqrt{s} = 8\,\text{TeV}) = 4.7 \pm 1.5(\text{stat.}) \pm 0.5(\text{syst.}) \pm 0.1(\text{lumi.})\,\text{fb} \tag{7.1}$$

in agreement with the theoretical prediction and with a signal significance of 2.6σ. This analysis is limited by the volume of recorded data and the lack of simulation data for the electroweak backgrounds. The analysis is successful in proving diboson searches are possible at LHCb. In the future LHCb runs, greater volumes of recorded data and increasing signal cross sections would result in fifty times as many reconstructed events in the detector. At this stage, there is great possibility for a competitive measurement of WW at LHCb. Increased luminosity will also allow background events faking leptons to be estimated using a fully data driven method, further reducing a large statistical uncertainty. With increased precision these measurements will begin to probe the region of low Björken–x variable, with implications for the global fits of parton distribution functions. It may also be advantageous to parallelise any $t\bar{t}$ and WW analyses that differ only by replacing the jet veto with a b jet requirement.
In addition to the WW channel, it will become possible to facilitate the ZZ channels hitherto inaccessible due to low event rates. This channel produced four isolated high p_T leptons, that few background processes at LHCb are able to mimic. With reasonably low number of observed events, a very pure signal sample can be measured. This work ties in closely with the LHCb analyses measuring single electroweak boson production. Using those results it is seen that the four muon channel will be particularly productive. The analysis presented in this thesis provides a motivation and proof of concept for further LHCb diboson measurements in the next data run.

References

[1] A. Einstein, Annalen der Physik **18**, 639 (1905).

[2] Particle Data Group, J. Beringer *et al.*, Phys.Rev. **D86**, 010001 (2012).

[3] E. Noether, Nachr. d. Knig. Gesellsch. d. Wiss. zu Gttingen, Math-phys. **235**, 257 (1918).

[4] J. Price and J. Vossebeld, *Search for a Higgs boson in the $H \to ZZ$ and $ZH \to ll + invisible$ channels with the ATLAS detector*, PhD thesis, Liverpool, University of Liverpool, 2013, Presented 29 Jun 2013.

[5] Gfitter Group, M. Baak *et al.*, Eur.Phys.J. **C74**, 3046 (2014), 1407.3792.

[6] S. P. Martin, Adv.Ser.Direct.High Energy Phys. **21**, 1 (2010), hep-ph/9709356.

[7] LHCb collaboration, R. Aaij *et al.*, Phys.Rev.Lett. **111**, 101805 (2013), 1307.5024.

[8] C. Beskidt *et al.*, Phys.Lett. **B705**, 493 (2011), 1109.6775.

[9] L. Canetti, M. Drewes, and M. Shaposhnikov, New J.Phys. **14**, 095012 (2012), 1204.4186.

[10] B. Cleveland *et al.*, Astrophys.J. **496**, 505 (1998).

[11] A. Bellerive, Int.J.Mod.Phys. **A19**, 1167 (2004), hep-ex/0312045.

[12] Z. Maki, M. Nakagawa, and S. Sakata, Prog.Theor.Phys. **28**, 870 (1962).

[13] ALEPH Collaboration, D. Decamp *et al.*, Phys.Lett. **B231**, 519 (1989).

[14] G. Altarelli and G. Parisi, Nucl.Phys. **B126**, 298 (1977).

[15] V. Gribov and L. Lipatov, Sov.J.Nucl.Phys. **15**, 438 (1972).

[16] Y. L. Dokshitzer, Sov.Phys.JETP **46**, 641 (1977).

[17] CMS Collaboration, S. Chatrchyan *et al.*, JHEP **1401**, 096 (2014), 1312.1129.

[18] CMS Collaboration, S. Chatrchyan *et al.*, Phys.Rev. **D89**, 092007 (2014), 1312.5353.

[19] ATLAS Collaboration, G. Aad *et al.*, Phys.Lett. **B726**, 88 (2013), 1307.1427.

[20] ATLAS Collaboration, G. Aad *et al.*, CERN-PH-EP-2014-170 (2014), 1408.5191.

[21] H1 and ZEUS Collaboration, F. Aaron *et al.*, JHEP **1001**, 109 (2010), 0911.0884.

[22] R. Thorne, A. Martin, W. Stirling, and G. Watt, Parton Distributions and QCD at LHCb, in *International Workshop on Deep Inelastic Scattering (DIS2008)*, p. 30, 2008, 0808.1847.

[23] CMS Collaboration, S. Chatrchyan *et al.*, Phys.Lett. **B721**, 190 (2013), 1301.4698.

[24] CMS Collaboration, V. Khachatryan *et al.*, CERN-PH-EP-2014-080 (2014), 1406.0113.

[25] ATLAS Collaboration, G. Aad *et al.*, Phys.Rev. **D87**, 112001 (2013), 1210.2979.

[26] O. S. Brning *et al.*, *LHC Design Report* (CERN, Geneva, 2004).

[27] K. Wille, *The Physics of Particle Accelerators* (Oxford University Press, 2000).

[28] CERN - Science Grand Format, 2013, Website at `http://bigscience.web.cern.ch/bigscience/en/lhc/lhc2.html`.

[29] The ATLAS Collaboration, JINST **3**, S08003 (2008).

[30] The CMS Collaboration, JINST **3**, S08004 (2008).

[31] The ALICE Collaboration, JINST **3**, S08002 (2008).

[32] The LHCb Collaboration, JINST **3**, S08005 (2008).

[33] D. Fournier, EPJ Web Conf. **28**, 01003 (2012), 1201.4681.

[34] S. Farry, *A measurement of Z production using tau final states with the LHCb detector*, PhD thesis, U. Coll., Dublin, 2012, Presented 12 Nov 2012.

[35] P. Rodriguez Perez, JINST **7**, C12008 (2012), 1209.4845.

[36] LHCb Collaboration, CERN Report No. CERN-LHCC-2002-029, 2002 (unpublished).

[37] R. Fruhwirth, Nucl.Instrum.Meth. **A262**, 444 (1987).

[38] LHCb Collaboration, M. Adinolfi *et al.*, Eur.Phys.J. **C73**, 2431 (2013), 1211.6759.

[39] LHCb Collaboration, *LHCb RICH: Technical Design Report* (CERN, Geneva).

[40] G. Corti *et al.*, IEEE Trans.Nucl.Sci. **53**, 1323 (2006).

[41] G. Barrand *et al.*, GAUDI - The software architecture and framework for building LHCb data processing applications, in *International Conference on Computing in High-Energy Physics and Nuclear Physics (CHEP 2000)*.

[42] T. Sjostrand, S. Mrenna, and P. Z. Skands, Comput.Phys.Commun. **178**, 852 (2008), 0710.3820.

[43] GEANT4, S. Agostinelli *et al.*, Nucl.Instrum.Meth. **A506**, 250 (2003).

[44] J. Hisano, K. Kawagoe, R. Kitano, and M. M. Nojiri, Phys.Rev. **D66**, 115004 (2002), hep-ph/0204078.

[45] J. R. Ellis, K. A. Olive, Y. Santoso, and V. C. Spanos, Phys.Lett. **B573**, 162 (2003), hep-ph/0305212.

[46] I. Aitchison, **SLAC-R-865** (2007).

[47] G. 't Hooft, Phys.Rev.Lett. **37**, 8 (1976).

[48] M. Gonzalez-Garcia, AIP Conf.Proc. **917**, 3 (2007).

[49] ATLAS Collaboration, D. Orestano, PoS **CHARGED**, 002 (2010).

[50] W. Beenakker, R. Hopker, and M. Spira, (1996), hep-ph/9611232.

[51] ATLAS Collaboration, G. Aad *et al.*, JHEP **1411**, 118 (2014), 1407.0583.

[52] ATLAS Collaboration, G. Aad *et al.*, Eur.Phys.J. **C72**, 2174 (2012), 1207.4686.

[53] ATLAS Collaboration, G. Aad *et al.*, Phys.Rev.Lett. **109**, 211802 (2012), 1208.1447.

[54] ATLAS Collaboration, G. Aad *et al.*, Phys.Rev.Lett. **109**, 211803 (2012), 1208.2590.

[55] ATLAS Collaboration, G. Aad *et al.*, Eur.Phys.J. **C72**, 2237 (2012), 1208.4305.

[56] ATLAS Collaboration, G. Aad *et al.*, Phys.Lett. **B720**, 13 (2013), 1209.2102.

[57] ATLAS Collaboration, G. Aad *et al.*, JHEP **1211**, 094 (2012), 1209.4186.

[58] ATLAS Collaboration, G. Aad *et al.*, JHEP **1310**, 189 (2013), 1308.2631.

[59] ATLAS Collaboration, G. Aad *et al.*, JHEP **1406**, 124 (2014), 1403.4853.

[60] ATLAS Collaboration, G. Aad *et al.*, Eur.Phys.J. **C74**, 2883 (2014), 1403.5222.

[61] ATLAS Collaboration, G. Aad *et al.*, JHEP **1409**, 015 (2014), 1406.1122.

[62] ATLAS Collaboration, G. Aad *et al.*, Phys.Rev. **D90**, 052008 (2014), 1407.0608.

[63] E. Boos *et al.*, (2001), hep-ph/0109068.

[64] ATLAS Collaboration, G. Aad *et al.*, Report No. ATLAS-CONF-2011-063, ATLAS-COM-CONF-2011-068, 2011 (unpublished).

[65] ATLAS Collaboration, G. Aad *et al.*, Eur.Phys.J. **C72**, 1909 (2012), 1110.3174.

[66] M. Cacciari, G. P. Salam, and G. Soyez, JHEP **0804**, 063 (2008), 0802.1189.

[67] P. Konar, K. Kong, K. T. Matchev, and M. Park, JHEP **1106**, 041 (2011), 1006.0653.

[68] ATLAS Collaboration, CERN Report No. ATLAS-CONF-2011-102, 2011 (unpublished).

[69] ATLAS Collaboration, G. Aad *et al.*, Report No. ATLAS-CONF-2011-102, ATLAS-COM-CONF-2011-110, 2011 (unpublished).

[70] GEANT4, S. Agostinelli *et al.*, Nucl.Instrum.Meth. **A506**, 250 (2003).

[71] ATLAS Collaboration, G. Aad *et al.*, Eur.Phys.J. **C70**, 823 (2010), 1005.4568.

[72] M. Bahr *et al.*, Eur.Phys.J. **C58**, 639 (2008), 0803.0883.

[73] ATLAS Collaboration, Report No. ATLAS-COM-PHYS-2012-092, 2012 (unpublished).

[74] A. L. Read, Journal of Physics G: Nuclear and Particle Physics **28**, 2693 (2002).

[75] S. Frixione, P. Nason, and G. Ridolfi, JHEP **0709**, 126 (2007), 0707.3088.

[76] T. Melia, P. Nason, R. Rontsch, and G. Zanderighi, JHEP **1111**, 078 (2011), 1107.5051.

[77] P. Nason and G. Zanderighi, Eur.Phys.J. **C74**, 2702 (2014), 1311.1365.

[78] A. Martin, W. Stirling, R. Thorne, and G. Watt, Eur.Phys.J. **C63**, 189 (2009), 0901.0002.

[79] J. Gao *et al.*, Phys.Rev. **D89**, 033009 (2014), 1302.6246.

[80] A. Martin, W. Stirling, R. Thorne, and G. Watt, Eur.Phys.J. **C70**, 51 (2010), 1007.2624.

[81] H. Brown, T. Bowcock, and D. Hutchcroft, *Monitoring Radiation Damage in the Vertex Locator and Top Pair Production in LHCb*, PhD thesis, Liverpool U., 2013, Presented 07 Nov 2013.

[82] Particle Data Group, K. Olive *et al.*, Chin.Phys. **C38**, 090001 (2014).

[83] LHCb Collaboration, R. Aaij *et al.*, JHEP **1206**, 058 (2012), 1204.1620.

[84] LHCb Collaboration, R. Aaij *et al.*, JHEP **1212**, 125 (2012), 1210.2645.

[85] LHCb Collaboration, R. Aaij *et al.*, JHEP **1302**, 106 (2013), 1212.4620.

[86] LHCb Collaboration, G. Lanfranchi *et al.*, Report No. LHCb-PUB-2009-013, CERN-LHCb-PUB-2009-013, 2009 (unpublished).

[87] M. De Cian, CERN Report No. LHCb-INT-2010-058. CERN-LHCb-INT-2010-058, 2010 (unpublished).

[88] S. Farry and N. Chiapolini, CERN Report No. LHCb-INT-2014-030. CERN-LHCb-INT-2014-030, 2014 (unpublished).

[89] LHCb Collaboration, D. Ward, Report No. LHCb-ANA-2014-086 ; CERN-LHCb-ANA-2014-086, 2014 (unpublished).

[90] LHCb collaboration, R. Aaij *et al.*, JHEP **1401**, 033 (2014), 1310.8197.

[91] W. Barter and D. Ward, *Z boson and associated jet production at the LHCb experiment*, PhD thesis, Cambridge U. (main), 2014, Presented 27 May 2014.

[92] LHCb Collaboration, R. Aaij *et al.*, JINST **7**, P01010 (2012), 1110.2866.

[93] S. van der Meer, CERN Report No. CERN-ISR-PO-68-31. ISR-PO-68-31, 1968 (unpublished).

[94] M. Ferro-Luzzi, Nucl.Instrum.Meth. **A553**, 388 (2005).

[95] ATLAS Collaboration, CERN Report No. ATLAS-CONF-2014-033, 2014 (unpublished).

[96] L. Moneta *et al.*, PoS **ACAT2010**, 057 (2010), 1009.1003.

[97] P. K. Sinervo, Report No. CDF-PUB-STATISTICS-PUBLIC-6031, 2002 (unpublished), hep-ex/0208005.

[98] T. Gershon, Flavour physics in the LHC era, in *SUSSP69*, 2013, 1306.4588.

[99] LHCb Collaboration, CERN Report No. CERN-LHCC-2011-001. LHCC-I-018, 2011 (unpublished).

[100] M.-H. Schune, (2013), 1301.4811.

[101] LHCb Collaboration, CERN Report No. CERN-LHCC-2014-016. LHCB-TDR-016, 2014 (unpublished).

[102] LHCb Collaboration, CERN Report No. CERN-LHCC-2014-001. LHCB-TDR-015, 2014 (unpublished).

[103] LHCb Collaboration, CERN Report No. CERN-LHCC-2013-022. LHCB-TDR-014, 2013 (unpublished).

[104] LHCb Collaboration, CERN Report No. CERN-LHCC-2013-021. LHCB-TDR-013, 2013 (unpublished).

[105] M. Czakon, P. Fiedler, and A. Mitov, Phys.Rev.Lett. **110**, 252004 (2013), 1303.6254.